cy. 1

ORNL-4324
UC-25 – Metals, Ceramics, and Materials

COATED-PARTICLE FUELS

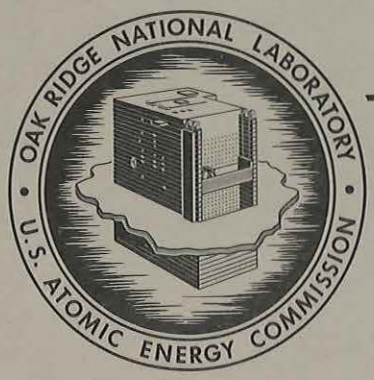

OAK RIDGE NATIONAL LABORATORY
operated by
UNION CARBIDE CORPORATION
for the
U.S. ATOMIC ENERGY COMMISSION

ORNL-4324

Contract No. W-7405-eng-26

COATED-PARTICLE FUELS

T. G. Godfrey J. L. Scott
R. L. Beatty J. H. Coobs

Metals and Ceramics Division

J. W. Prados

Consultant from the University of Tennessee

L. G. Overholser

Reactor Chemistry Division

and

L. M. Ferris

Chemical Technology Division

Prepared as a chapter for the third edition
of the Reactor Handbook

NOVEMBER 1968

OAK RIDGE NATIONAL LABORATORY
Oak Ridge, Tennessee
operated by
UNION CARBIDE CORPORATION
for the
U.S. ATOMIC ENERGY COMMISSION

ORNL-4324

Contract No. W-7405-eng-26

COATED-PARTICLE FUELS

T. G. Godfrey J. L. Scott
R. L. Beatty J. H. Coobs

Metals and Ceramics Division

J. W. Prados

Consultant from the University of Tennessee

L. G. Overholser

Reactor Chemistry Division

and

L. M. Ferris

Chemical Technology Division

Prepared as a chapter for the third edition
of the Reactor Handbook

NOVEMBER 1968

OAK RIDGE NATIONAL LABORATORY
Oak Ridge, Tennessee
operated by
UNION CARBIDE CORPORATION
for the
U.S. ATOMIC ENERGY COMMISSION

PREFACE

This report was prepared as a chapter for the third edition of the Reactor Handbook to be published under the auspices of the U.S. Atomic Energy Commission. This chapter surveys the information on fabrication, characterization, performance, and reprocessing of coated-particle fuels. Emphasis is placed on pyrolytic-carbon-coated oxides and carbides since the bulk of the development work has been on these types of particles.

CHAPTER 8 COATED-PARTICLE FUELS

Contents

PART B. FUEL MATERIALS

CHAPTER 8 COATED-PARTICLE FUELS

8-1 INTRODUCTION

The term coated-particle fuels denotes 100- to 500-μ-diam microspheres of plutonium, uranium, or thorium oxide or dicarbide coated with pyrolytic carbon, silicon carbide, Al_2O_3, BeO, or combinations of these materials. These fuels find application in high-temperature helium or CO_2-cooled reactors moderated with BeO or graphite. The primary purposes of the coatings are to prevent undesirable reactions during fabrication and in service and to contain fission products during irradiation, although in those reactors with purged elements, such as the Peach Bottom Reactor, the latter function is not required. The advantages of coated-particle fuels arise from their high service temperatures and their lack of constituents with high neutron absorption cross sections. A major disadvantage is the relatively high fabrication cost. But this cost is offset by the high thermal efficiency, high burnup, long life, and neutron economy associated with thorium utilization, so that overall fuel cycle costs may be lower than those of competing reactor systems.[1]

There is another type of coated-particle fuel which has been omitted from this definition since it is discussed in detail in Chapter 9. Fuel microspheres frequently are given metallic coatings before being fabricated into plate-type, dispersion fuel elements. The metallic coatings prevent fuel matrix reactions for incompatible systems or promote ideal dispersions.

Depending on the particular reactor system design, the coating on fuel particles functionally may serve any of several purposes.[2] These might include the following:

1. highly localized containment of fuel,
2. highly localized containment of fission product,
3. greater latitute in providing barriers for improved compatibility with coolant atmospheres or materials of construction,
4. simplification of fuel-handling procedures by the elimination of oxidation, hydrolysis, or fuel dusting,
5. protection of matrix materials from fission-recoil damage, and
6. improved distribution of fuel by the spacing provided by the coating.

The most important single function of the coating is to serve as a miniature pressure vessel to contain fission-product gases and thereby prevent excessive swelling of the fuel. Stresses in coatings arise from several effects, which must be considered in design:[3]

1. fission-gas pressure buildup inside the coating,
2. swelling of the fuel particle due to the accumulation of fission products,
3. dimensional changes in the coating due to fast neutrons, and
4. damage to the inner layers of the coating by fission recoils.

Stress relief may occur as a result of creep.[4] Spherical geometry appears best for the brittle ceramic coatings.

Coated-particle fuels evolved rather naturally from earlier forms of all-ceramic fuel elements. The first step in the evolution of such elements was the impregnation of graphite rods with uranyl nitrate followed by baking to convert the fuel to UO_2. Irradiation tests on the

impregnated elements showed that they rapidly released fission products which would severely contaminate the primary-coolant piping. The next evolutionary step was to coat impregnated graphite bodies with an impervious layer of pyrolytic carbon or siliconized silicon carbide. These coatings worked well for brief periods, but eventually shrinkage stresses induced by irradiation resulted in failure of the coating. Once the coating cracked, the release rates of fission products were equivalent to the rates for uncoated bodies. Even a small pinhole had a catastrophic effect.

The next step was to coat individual fuel particles. It was reasoned that failures of a few coatings would not be catastrophic, because each coating contained only a small fraction of the fuel. The first successful demonstration of this principle involved Al_2O_3-coated UO_2 particles fabricated and tested by workers at Battelle Memorial Institute during development of fuel for the Sanderson and Porter Pebble Bed Reactor.[5] In a purge capsule irradiation test, they obtained noble-gas release-rate-to-birth-rate (R/B) ratios shown in Fig. 8.1. From initial values of 2×10^{-7}, the R/B's rose as burnup proceeded and individual coatings failed. Although final R/B's were higher than desired for the application, the low initial values and the low rate of increase of release with burnup pointed clearly to the promise of the approach. Post-irradiation examination of the BMI capsule showed that most of the coatings which failed were near the surface of the fuel element. These failures, initially attributed to low matrix restraint near the element surface, were finally shown to be the result of irradiation damage to Al_2O_3 at temperatures below 1000°C.

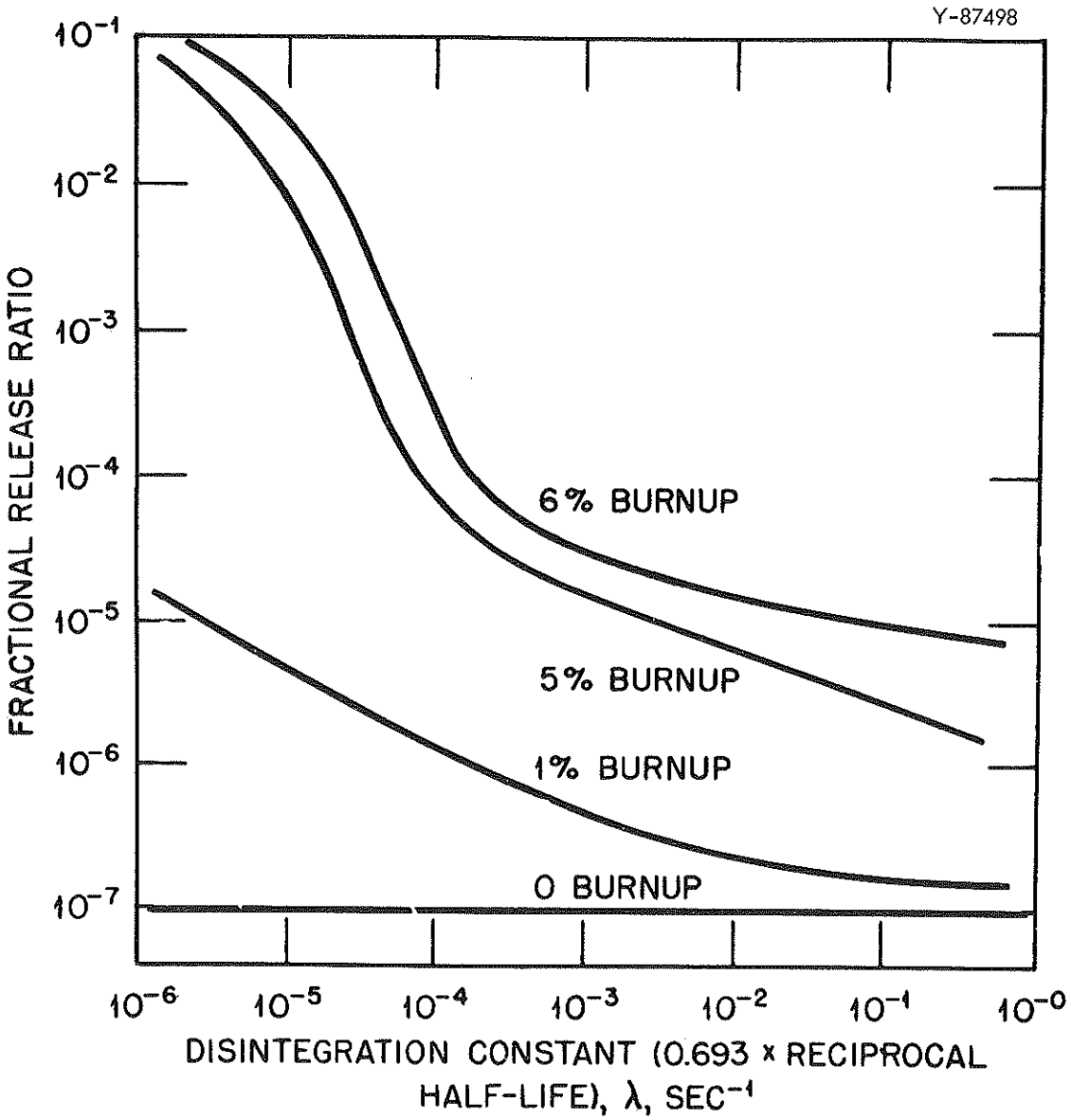

Fig. 8.1. In-pile fission-product-release behavior of alumina-coated uranium dioxide particle during Sanderson and Porter experiment. Reprinted from reference 5.

Attention turned quickly to pyrolytic-carbon-coated UC_2 particles. Carbon had the advantage of complete compatibility with both fuel and graphite up to at least 1600°C. In addition, coating fabrication by the pyrolytic decomposition of hydrocarbons was found to be a relatively easy process. Pyrolytic-carbon-coated UC_2 or $(Th,U)C_2$ particles were selected as fuel for the OECD Dragon Reactor, the German Pebble-Bed (AVR) Reactor, the U.S. experimental UHTREX and Peach Bottom reactors, all graphite-moderated and helium-cooled. Pyrolytic-carbon-coated fuel particles are now also being considered for use within a SiC matrix for advanced CO_2-cooled AGR's.

Recently, pyrolytic-carbon-coated UO_2 and $(Th,U)O_2$ particles have been shown to be attractive. Initially, it was thought that these materials would be incompatible above about 1200°C, but excellent compatibility was found up to at least 2000°C, even after extended irradiation. The basic compatibility is attributed to the retention of CO by the pyrolytic-carbon coating. Once the equilibrium CO partial pressure is reached, no further reaction occurs. Both coated oxides and carbides are being considered for use in the Fort St. Vrain Reactor being developed by Gulf General Atomic for the Public Service Company of Colorado.

A problem which has arisen with pyrolytic-carbon-coated fuels is the migration of solid fission products through the coating. Noble gases are very effectively retained by an intact coating, but certain solid fission products, such as barium and strontium, migrate through the coating at high temperatures and escape from the fuel elements. Silicon carbide effectively bars solid fission-product migration, and its use as a barrier or sealer layer in conjunction with the pyrolytic carbon is

receiving increased attention. This type of coating was used in the first and second charges of the Dragon Reactor.

Concurrent with the development of pyrolytic-carbon-coated fuels was the development of BeO-coated UO_2 for use in a BeO matrix. In spite of its toxicity and high cost, BeO is attractive because it acts as a neutron generator due to the (n,2n) reaction which occurs. Emphasis has waned in this direction because of low-temperature irradiation damage to BeO that causes grain-boundary separation and eventual pulverization. There is still interest in using beryllium with graphite-matrix fuels in HTGR's, for this appears to be the only way to make an HTGR breed. Work on BeO-coated fuels has been abandoned.

8-2 FABRICATION

A complete description of coated-particle-fuels fabrication must include fuel-kernel preparation, coating application, and fuel element fabrication. The variety of processes for each of these steps will be discussed in this section.

8-2.1 Fuel Kernels

A wide variety of fuel kernels has been produced to meet the needs of various reactors. These include the compounds UO_2, UC_2, UC, PuO_2, ThO_2, and ThC_2 and mixed compositions such as $(Th,U)O_2$, $(Th,U)C_2$, and $(U,Pu)O_2$. For some applications, diluents such as excess carbon or ZrC may also be included to reduce the rate of volumetric heat generation or the fission density. Each compound or mixture of compounds has its peculiarities and requires a different processing technique. For example, whereas carbides must be handled in an inert atmosphere during processing,

many oxide compositions can be handled in air. With pure UO_2, care must be taken to prevent conversion to U_3O_8. For each composition, one usually uses unique conditions of temperature and cycle duration for sintering or melting.

For a given composition there are a number of important parameters to control during kernel fabrication: impurity levels, density, particle size range, spheroidicity, and abrasion resistance. Impurities may capture neutrons or affect the properties of the kernel. Either a high or low density may be desired, but in either case careful control is necessary for a consistent fuel loading. Some designers prefer a low-density microsphere because void volume for fuel swelling is provided within the fuel itself. Others prefer a high-density kernel and a porous inner coating. A narrow range of particle sizes within a given batch of particles is preferred to produce a uniform loading of fuel within an element. At the same time, the rate of rejection goes up as the particle size range is reduced. Thus, one must balance one factor against the other. Good spheroidicity is preferred for consistent coated-particle performance and can be achieved readily by most processes. Good abrasion resistance reduces the contamination picked up by the coating during the coating operation.

The types of processes which have been used to meet these criteria for various kernel compositions include (1) powder rolling and sintering, (2) particle melting, and (3) sol-gel.

Some processes involve a combination of these techniques. These processes and their advantages and disadvantages will now be considered.

Powder Rolling and Sintering

The powder rolling and sintering process has been used extensively for microsphere production.[6-11] Finely divided carbide, oxide, or metal powders with or without suitable binders, such as camphor, kerosene, or aluminum stearate are used as starting materials. For some types of feed, an inert atmosphere is required to prevent oxidation. If the feed contains more than one constituent, the materials are coprecipitated or are thoroughly blended, generally by ball milling.

The blended mass is then divided into uniform particles of the proper size by cold pressing the blend and forcing the compact through a sieve, by extruding spaghetti and chopping it, or by continuously adding fine powder to seed spheres on a gyrating table. Particles produced by either of the first two processes are then formed into spheroids by a rotating drum or planetary wheel. With the third process, the feeding of powder is discontinued when the proper size spheres are obtained. At this point, particles which are too large or small may be removed by sieving and recycled with additional feed.

A flowsheet for UO_2 particle preparation by prepressing, granulation, and sieving is shown in Fig. 8.2. The UO_2 powder is cold pressed at 15,000 psi and forced through a 30 mesh screen. These granules are re-pressed to a specified density (which determines the final sintered density) and regranulated. Sieved fractions of the proper size range are then made spherical and sintered. Rejects and fines are recycled. The ease of recycle is one of the attractive features of the powder process. Since the final density depends on many variables, particularly the characteristics of the starting powders, it is necessary to develop fabrication details experimentally for each type of powder being used as feed.

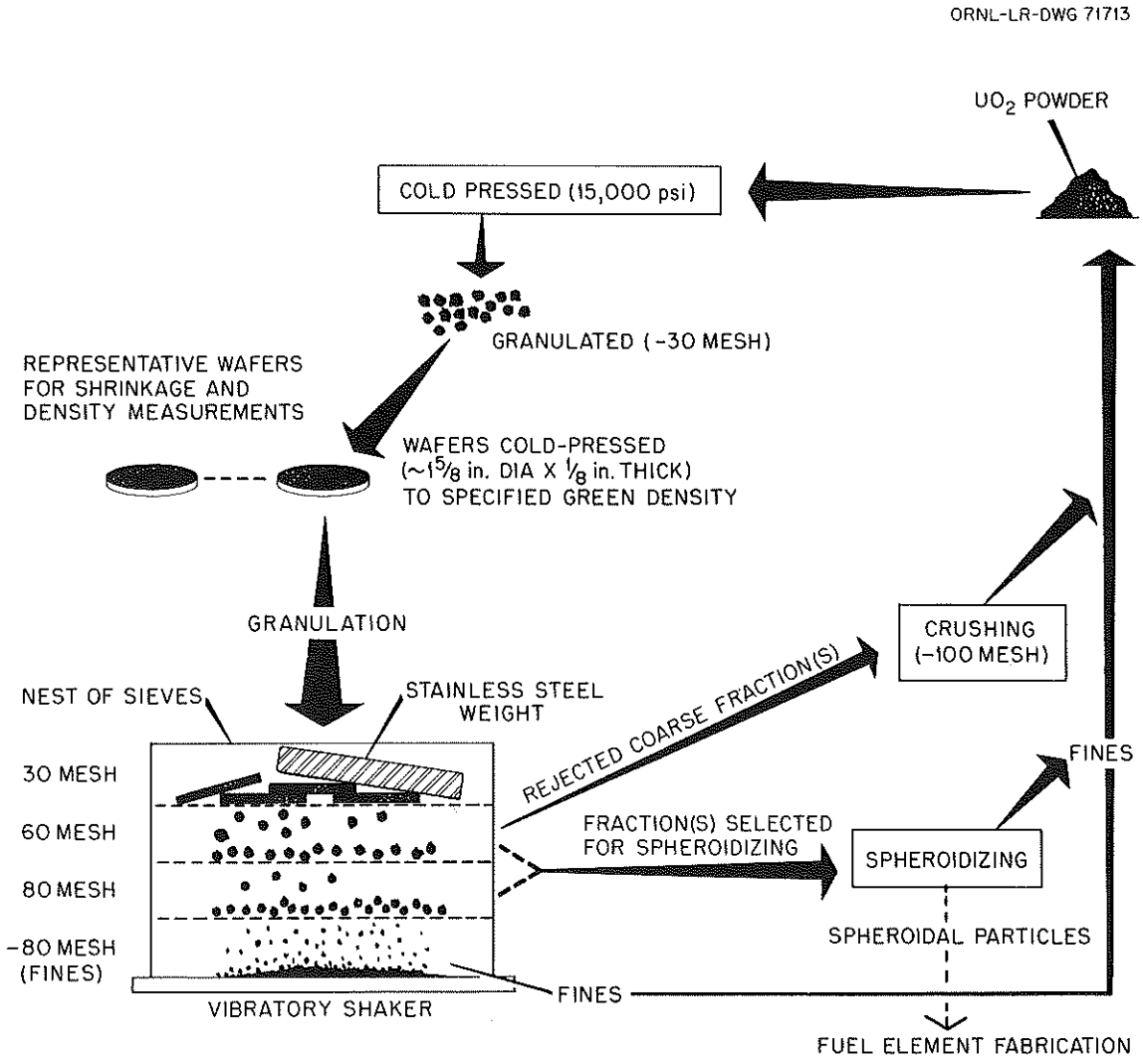

Fig. 8.2. Flowsheet for preparation of fuel particles. Submitted by Oak Ridge National Laboratory, July 1968.

Once spherical particles of the proper size have been obtained, they must be sintered. The sintering atmosphere and temperature cycle must be controlled carefully during this step. Sintering is usually done in vacuum, since this expedites the removal of volatiles at the beginning of the cycle and of gaseous reaction products at higher temperatures. A controlled heating rate is mandatory, for too rapid evolution of volatiles ruptures the sphere. Typical feed materials and reaction sintering conditions are given in Table 8.1. Spherical UO_2 particles after sintering in hydrogen at 1950°C are shown in Fig. 8.3. These are typical of products obtained by powder techniques.

The final steps after sintering are tumbling to separate particles and sieving to separate out doublets and fines. The kernels are then ready for coating.

Advantages of the powder rolling and sintering process are ease of scaleup for production, low cost, ability to produce almost any desired density, and ability to produce a wide variety of compositions, many of which could not be obtained by melting. Larger particle sizes, up to 2000 μ, can be achieved by this process rather than by alternatives.

Particle Melting

Particle melting has been used widely to produce fully dense spheroids of UC_2, ThC_2, and mixed carbides.[12–17] Melting is also possible for oxide particles, but is less attractive because of the higher melting points of UO_2 and ThO_2 compared to those of UC_2 and ThC_2 and because of the higher volatility of the oxides. Sol-gel techniques to be discussed later have supplanted melting processes for oxides.

Table 8.1. Typical Reaction Sintering Conditions for Fuel Microspheres

Feed	Product	Reaction		Sintering	
		Temperature (°C)	Atmosphere	Temperature (°C)	Atmosphere
U(metal)+C	UC, UC_2	900	Vacuum	1800	Vacuum
UC+ZrC	(Zr,U)C	2000	Vacuum	2000	Vacuum
UO_2+C	UC, UC_2	1600	Vacuum	1800	Vacuum
ThO_2+C	ThC, ThC_2	1950	Vacuum	2000	Vacuum
UO_2	UO_2			1750	Hydrogen
ThO_2	ThO_2			1750	Air
ThO_2+UO_2	$(Th,U)O_2$	1750	Hydrogen	1750	Hydrogen
PuO_2	PuO_2			1400	Air

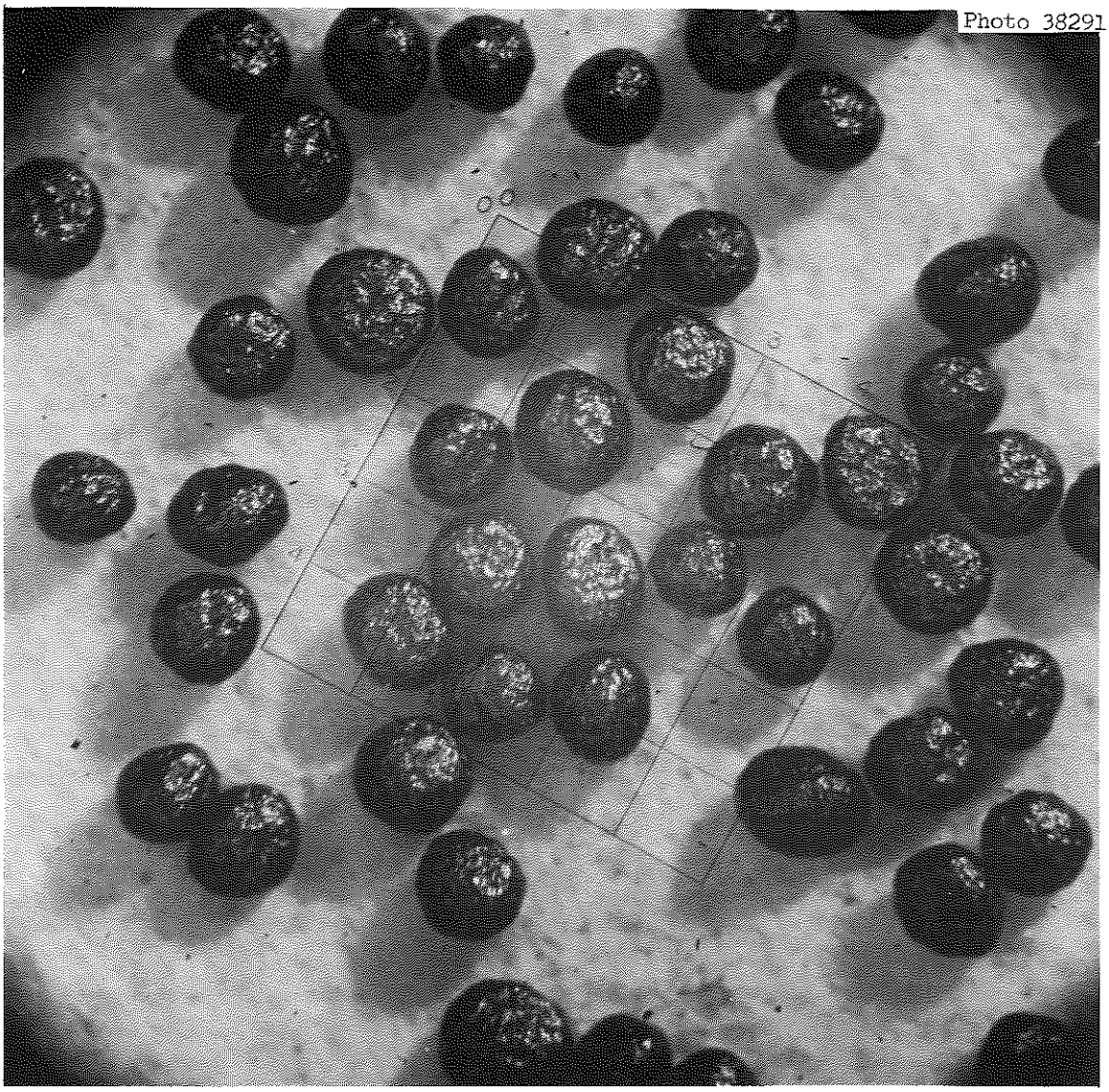

Fig. 8.3. Spheroidal UO_2 particles after sintering at 1750°C in hydrogen. Grid squares are approximately 350 μ. Submitted by Oak Ridge National Laboratory, July 1968.

Various melting processes may be used for carbides. The most important processes are (1) bed melting, (2) plasma melting, and (3) consumable electrode arc melting.

In the bed-melting process, granules of UO_2, ThO_2, or mixed oxides of the proper size, which are produced by techniques described in the previous section, are blended with a large excess of graphite powder or lampblack. The beds, with widely separated fuel particles, are then heated in vacuum to above 2450°C, the approximate eutectic melting points of the carbides. A controlled heating rate allows the CO to be removed during reaction of the oxides with the carbon. This step occurs in the temperature range 2000 to 2200°C. Spheres are formed upon melting because of the surface tension of the molten carbide phase. The bed is then cooled, and the fuel particles are separated from the carbon powder by sieving. Typical products are shown in Fig. 8.4.

An interesting feature of bed-melted carbide particles is the proeutectic graphite often found on the surface and as crystallites within the spheres. A microstructure showing the graphite is shown in Fig. 8.5. There is an advantage if the layer of graphite at the surface is continuous: It reduces the tendency for the fuel particles to react with impurities in the noble-gas atmosphere used in subsequent handling of the particles and inhibits uranium migration in service.

Plasma melting is an alternative to bed melting. This process was tried,[18] but not adopted, for fuel production for the Dragon Reactor and was used by Carbon Products Division of Union Carbide to produce fuel for the AVR Reactor.[19] Details of plasma melting have not been given in the literature, but the process simply consists of dropping

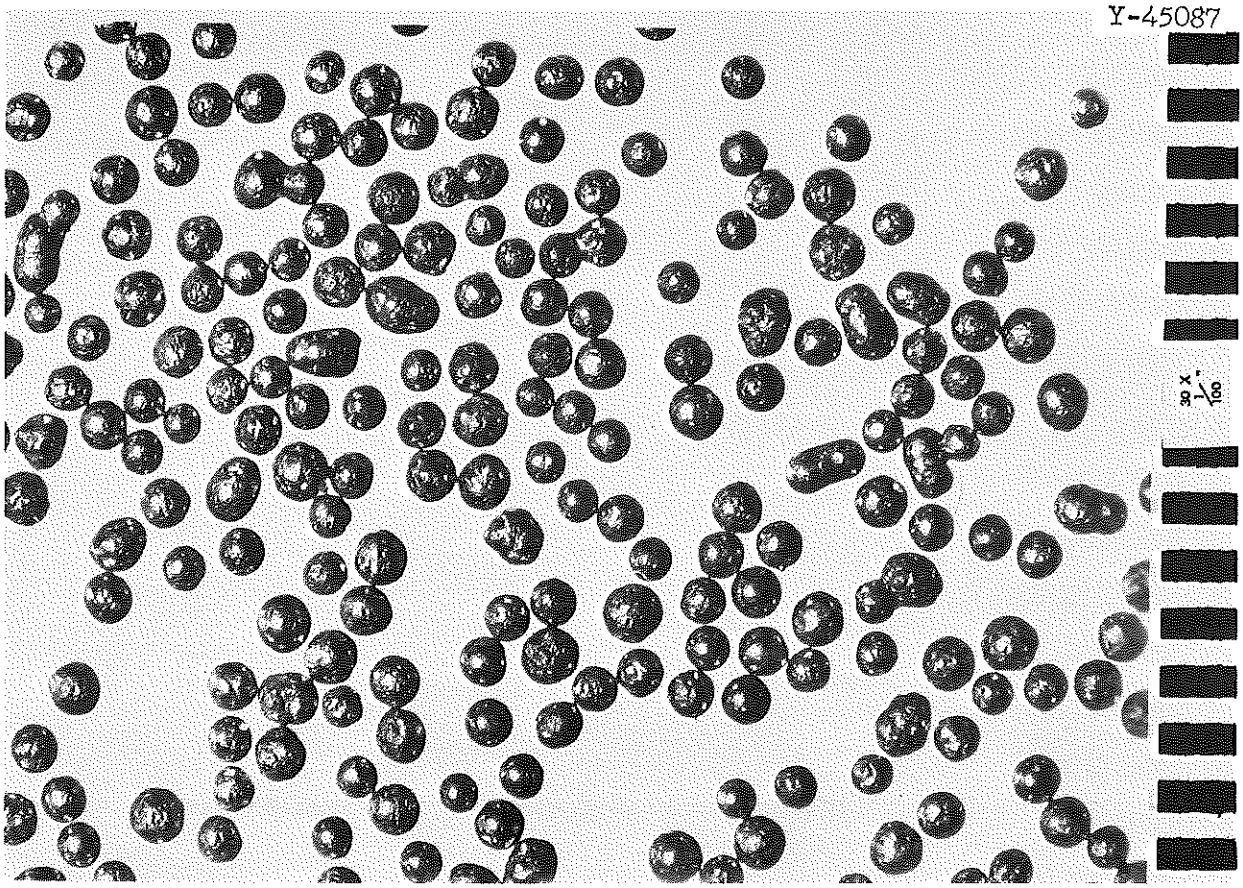

Fig. 8.4. Bed-melted UC_2 Microspheres, nominally 250 μ diameter. 30×. Submitted by Oak Ridge National Laboratory, July 1968.

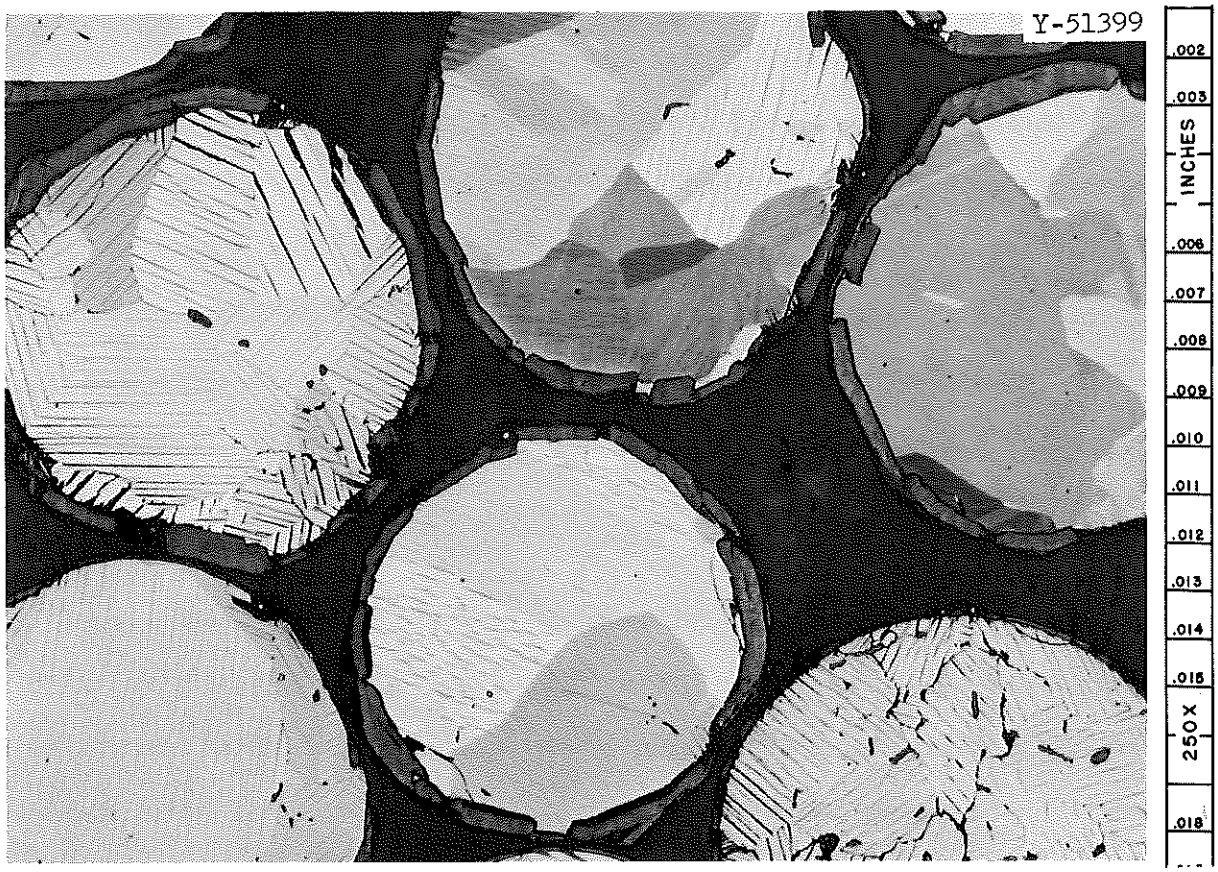

Fig. 8.5. Microstructure of bed-melted UC_2 microspheres showing proeutectic graphite surface layer and graphite stringers within the dicarbide grains. 250×. Submitted by Oak Ridge National Laboratory, July 1968.

suitable feed granules through a plasma. The process has the advantage that it is continuous instead of requiring intermittent batch production. The product is similar to the bed-melted product.

The fabrication of $(U_{0.3}Zr_{0.7})C$ microspheres by consumable-electrode arc melting has been described by Gibson.[20] The electrodes consisted of a homogeneous blend of UO_2, ZrO_2, and carbon. An arc was struck between two of these electrodes, and liquid (U,Zr)C, which formed at the ends of the electrodes, dropped off and solidified as microspheres. The density and shape of the product were good, but there is question regarding the ability to produce a product with good control of particle size. Gibson stated that the yield was over 90% in the −100 +325 region, but closer tolerances undoubtedly would result in higher rates of rejection.

Sol-Gel Process

The sol-gel process for fabricating fuel microspheres consists of three steps: (1) preparation of an aqueous sol, (2) removal of water to give gel particles, and (3) firing of the gel particles under controlled conditions to remove volatiles, sinter to high density, and cause chemical conversion if needed.[21–28] The process has the advantages of being amenable to a remote fuel recycle process and of yielding fully dense spheres at much lower sintering temperatures than are required for alternate processes. The sol-gel process was developed originally for ThO_2 sols,[21,22] but has been applied more recently to UO_2, PuO_2, and mixed oxides.[23–27,29] Spherical products with diameters of 50 to 700 μ and densities of 90 to 100% of theoretical have been produced.[29] By adding carbon sols to appropriate oxide sols and going through a final reaction step, one can also produce sol-gel carbide fuels.[25]

Sol Preparation. – Fuel materials for sol preparation generally consist of nitrate solutions of thorium, uranium, or plutonium since they are the normal form of product of an aqueous reprocessing scheme. Thus, the use of nitrate leads to a direct fuel cycle. Conversion of the nitrate into an oxide sol involves the following four steps.[29]

1. Reduce or oxidize to the best valence. U(IV) and Pu(IV) are preferred for urania or plutonia sols.

2. Convert the metal nitrate into a hydrated oxide.

3. Remove excess nitrate and nonvolatile impurities. For instance, NH_4NO_3 or $NaNO_3$ must be removed if the hydrous oxides are precipitated by NH_4OH or NaOH.

4. Disperse the oxide as a stable sol. Thoria colloidal particles are formed by steam denitration at temperatures up to 500°C. Sol formation involves dispersion of these particles in an aqueous medium of the proper pH. For urania and plutonia, colloidal particles are formed in solutions or as wet precipitates. Since urania readily oxidizes to the (VI) valence state, particle formation is carried out under reducing conditions in an inert atmosphere. Since thorium, however, has only the (IV) valence state, step 1 is not required nor is it necessary to provide a controlled atmosphere.

Mixed sols may be formed in two ways. One way is to mix two pure sols. This may be done readily if attention is paid to the pH of each sol. Mixed urania-plutonia-thoria sols may be prepared in any proportions desired. Thoria-urania sols with uranium-to-thorium ratios of less than 0.1 may be prepared by adding UO_3 or uranyl nitrate to thoria sols. The

U(VI) is adsorbed on the surface of the thoria particles. Reduction to the (IV) state is accomplished during or after sintering.

Since the formation of urania sol is more complicated than the formation of thoria or plutonia sols, which have (IV) valence in the fully oxidized state, the general flowsheet for urania sol formation has been chosen for illustration in Fig. 8.6. First, a uranous nitrate solution is prepared by reduction of uranyl nitrate with hydrogen in the presence of a platinum catalyst. Next, the solution is adjusted to a pH of 9 by addition of NH_4OH resulting in the formation of the hydrous uranous oxide. After being washed, the oxide is dispersed by the addition of nitric and formic acids and then by heating. The presence of formic acid helps maintain U(IV) and simplifies precipitation and washing.[24] The final urania sol is about 4 M with a NO_3-to-uranium ratio of about 0.17, a $COOH^-$-to-uranium ratio of about 0.1, and a U(IV)-to-uranium ratio of about 0.85.

Formation of Gel Microspheres. — After the appropriate sol is prepared, it is converted to gel microspheres by forming droplets in an appropriate anhydrous organic liquid, such as 2-ethyl-1-hexanol, and extracting the water. Spherical particles of 10 to 1000 μ diameter have been obtained in this way. The maximum droplet size is limited since very large drops will distort. A surfactant is added to the sol to prevent coalescence of sol drops with each other.

A variety of techniques has been used to disperse sol droplets in the organic drying medium, including two-fluid nozzles, rotary feeders, vibrating capillaries, electrostatic nozzles, falling drop dispersions,[29,30] and stirring of the two immiscible liquids. Characteristics

ORNL DWG 66-10980

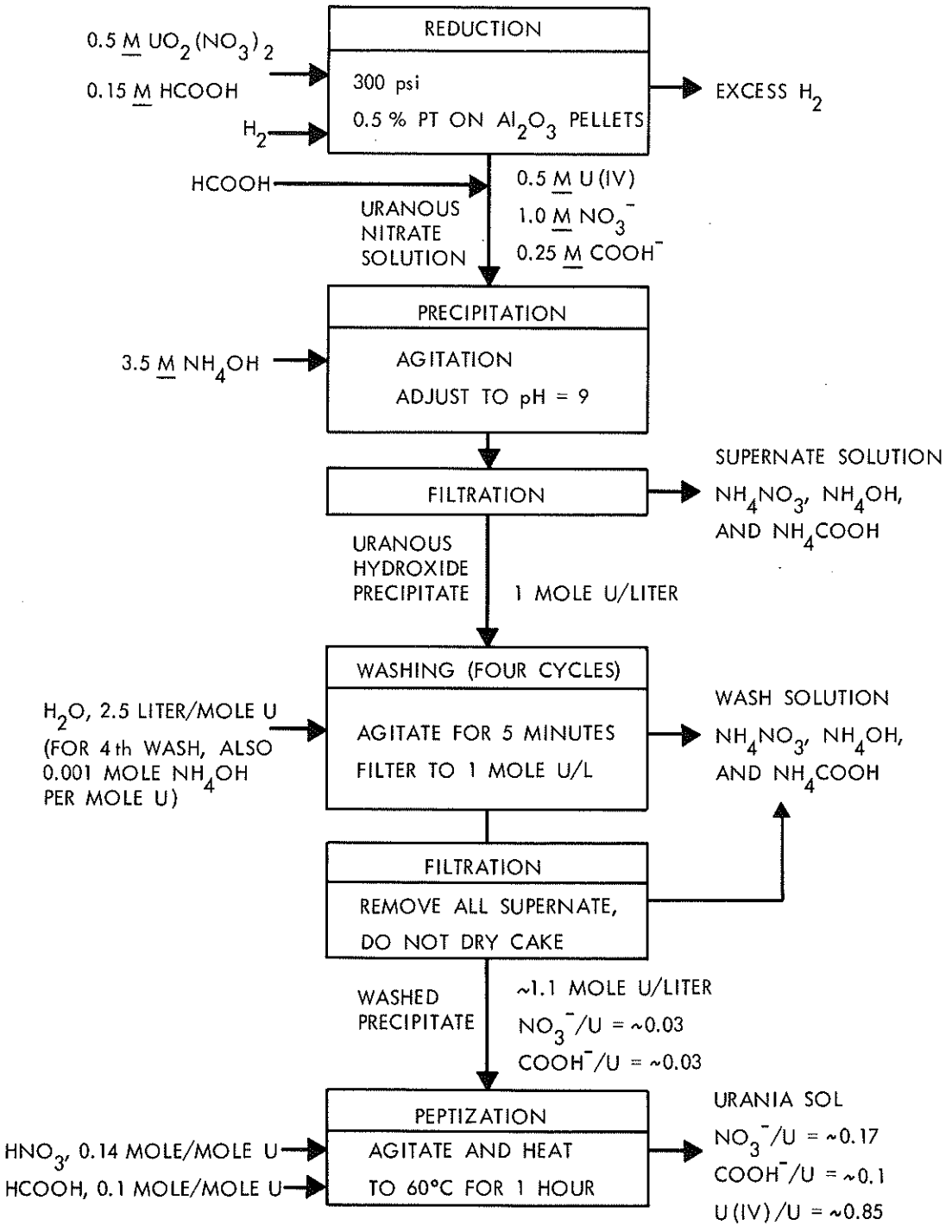

Fig. 8.6. Batch agitated-filter preparation of urania sol. Reprinted from reference 29.

of the products of the three most used techniques for producing the larger sizes are given in Table 8.2. Size yields for a stirred system are shown in Table 8.3. Although vibrating capillaries show the greatest uniformity of product, two-fluid nozzles are generally preferred because of their reliability and ease of control over a wide range of drop sizes. Single two-fluid nozzles consistently give 90 wt % of the product within ±15% of the mean diameter.[29] A schematic diagram of the single two-fluid nozzle is shown in Fig. 8.7. Typical 8% UO_2–ThO_2 microspheres produced by this method are shown in Fig. 8.8 as gels and after sintering.

A schematic of the column for forming sol-gel microspheres is shown in Fig. 8.9. The sol is injected at the top of a typical glass column. The droplets are suspended or fluidized by a circulating upflow stream of 2-ethyl-1-hexanol, which is continuously dried by distillation. As water is extracted from the droplets, their density increases so that their settling velocity increases. Eventually they settle to the bottom of the column and are transferred to the product drier. After being dried, they are calcined to form dense microspheres.

Sintering of Gel Microspheres. – Gel microspheres as extracted from the spheroidizing column are less than 40% of final density, contain large quantities of volatile compounds such as water, nitrates, organic solvents and surfactants, and yet have remarkable strength and abrasion resistance. The physically adsorbed volatiles are removed by heating in steam or in vacuum at temperatures in the range 200 to 400°C. Care is required during heating to prevent a rapid reaction which occurs near 350°C between the organics and nitrates in the gel. Too rapid energy release will result in explosion of the particles. Above 350°C, the

Table 8.2. Product Sizes of Calcined Thoria Microspheres from Three Dispersers[a]

	Two-Fluid Nozzles		Vibrating Capillaries			Free-Fall Drop
Number of feed capillaries	Single	Six	Single	Four	Four	19
Capillary diameter, μ	250	425	425	480	480	400
Sol feed rate, cm^3/min	1.2	24.7	1.2	19.2	9.6	9.6
Vibration frequency, cps			40	200	50	
Predicted mean size, μ	270[b]	230[b]	330[c]	310[c]	390[c]	
Amount of sample, g	540	10,200		314	720	480
Weight per cent in:[d]						
30/35 or 500–590 μ						97.9
35/40 or 420–500 μ					0.1	0.8
40/45 or 350–420 μ			0.2		61.9	1.1
45/50 or 297–350 μ	2.9	0.2	98.3	30.4	37.6	
50/60 or 250–297 μ	92.0	3.0	1.5	62.6	0.4	
60/70 or 210–250 μ	0	85.8		7.0		
–70 or < 210 μ	5.3	10.9				

[a]Sol feed: Thoria sols of 3.0 M Th, sol drop diameters of 2.35 times diameters of theoretically dense ThO_2 product.

[b]From two-fluid nozzle equation.

[c]From number of drops per cycle and flow rate.

[d]From use of U.S. Sieve Series screens.

Table 8.3. Size Yields for Thoria Microspheres from Stirred System[a]

Stirring Speed, rpm	Weight Percent in Size Range			
	< 150 μm	150–210 μm	210–250 μm	> 250 μm
330	31.8	24.0	20.7	23.5
350	34.2	27.4	22.8	15.6
370	42.5	35.0	21.2	1.3

[a]Yields are very system-dependent.

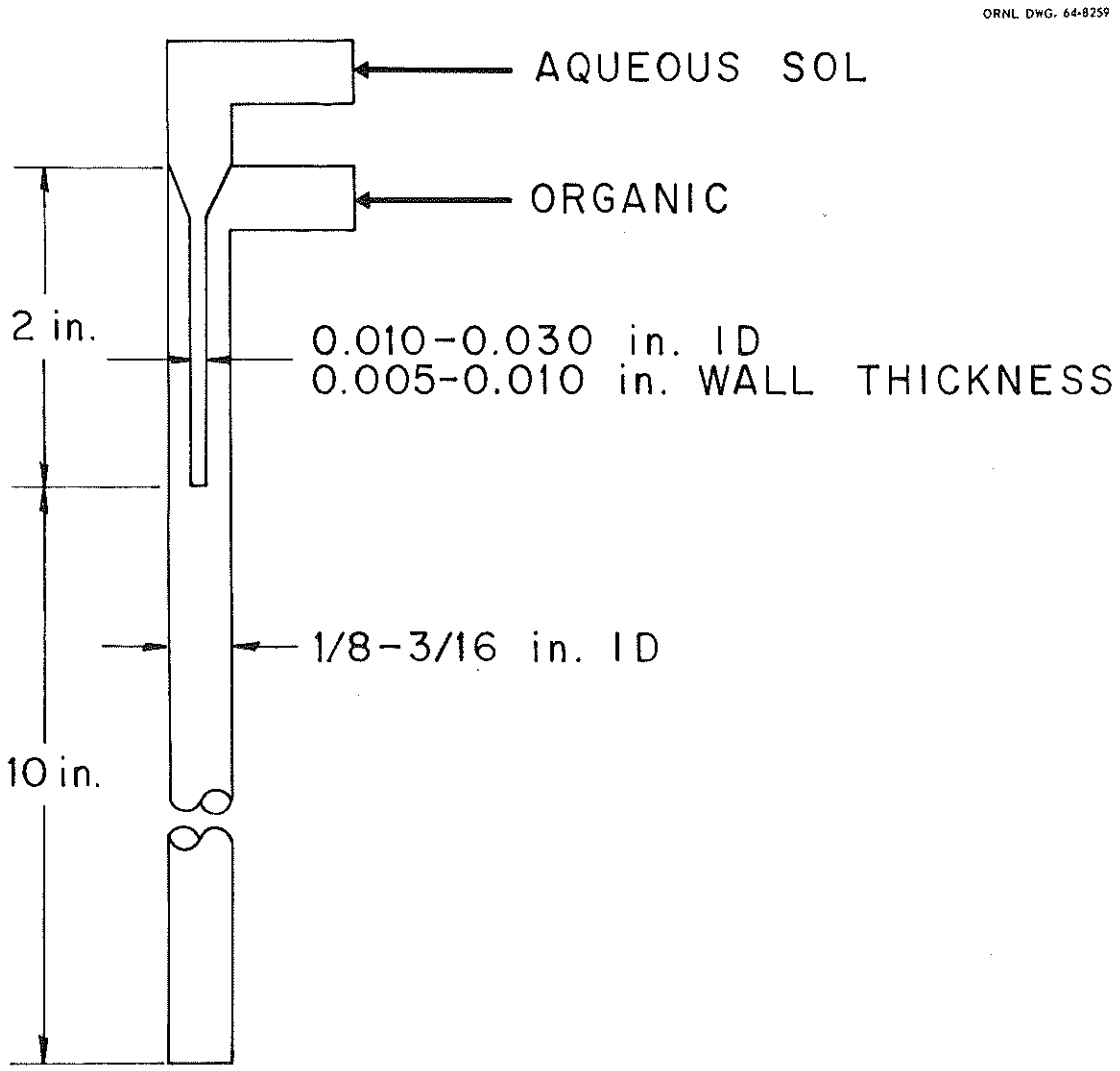

Fig. 8.7. Two-fluid nozzle for forming sol droplets. Reprinted from reference 24.

PHOTO 67083

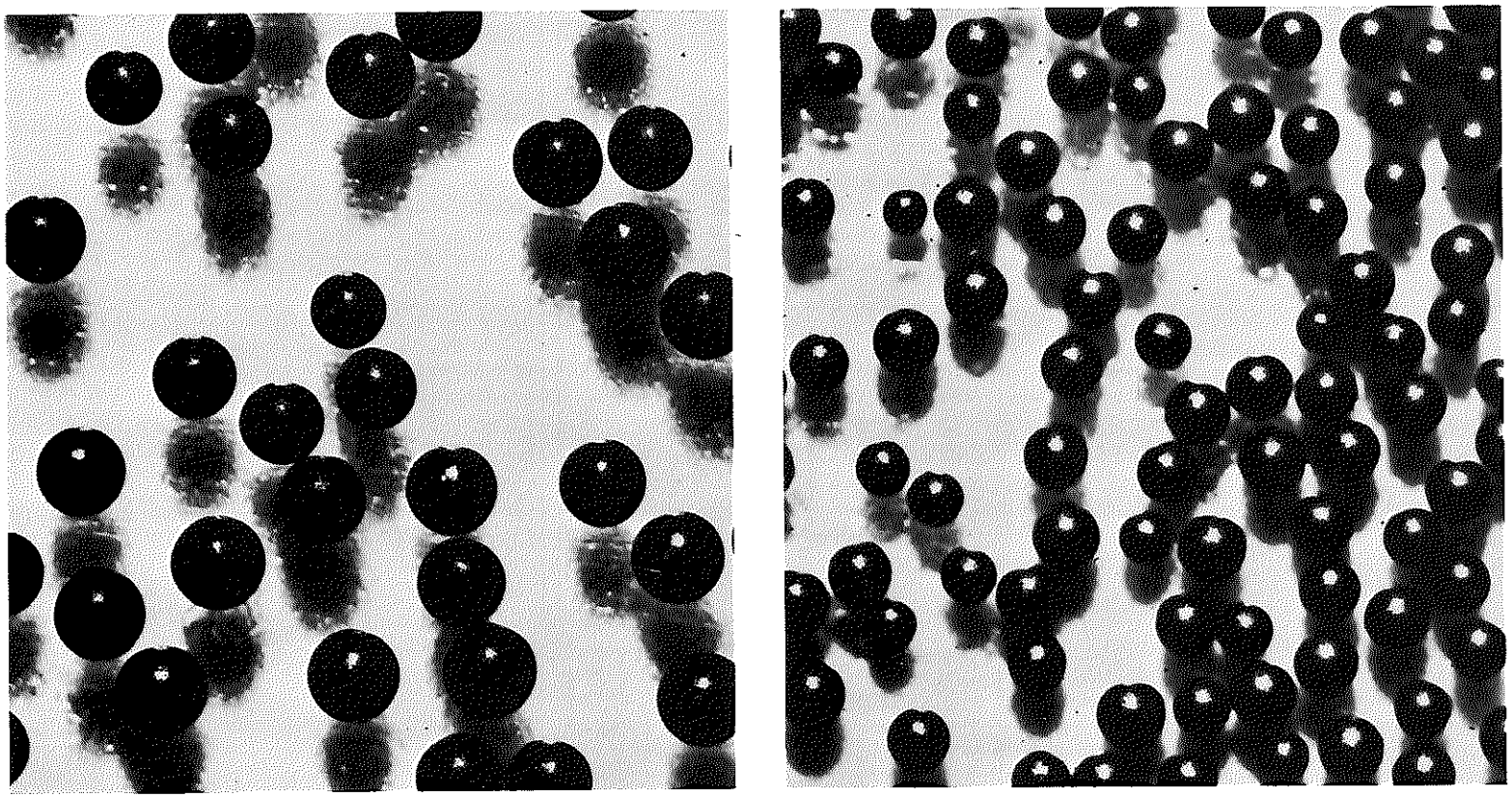

Fig. 8.8. Gel and 1150°C sintered 8% urania-thoria microspheres. Reprinted from reference 31.

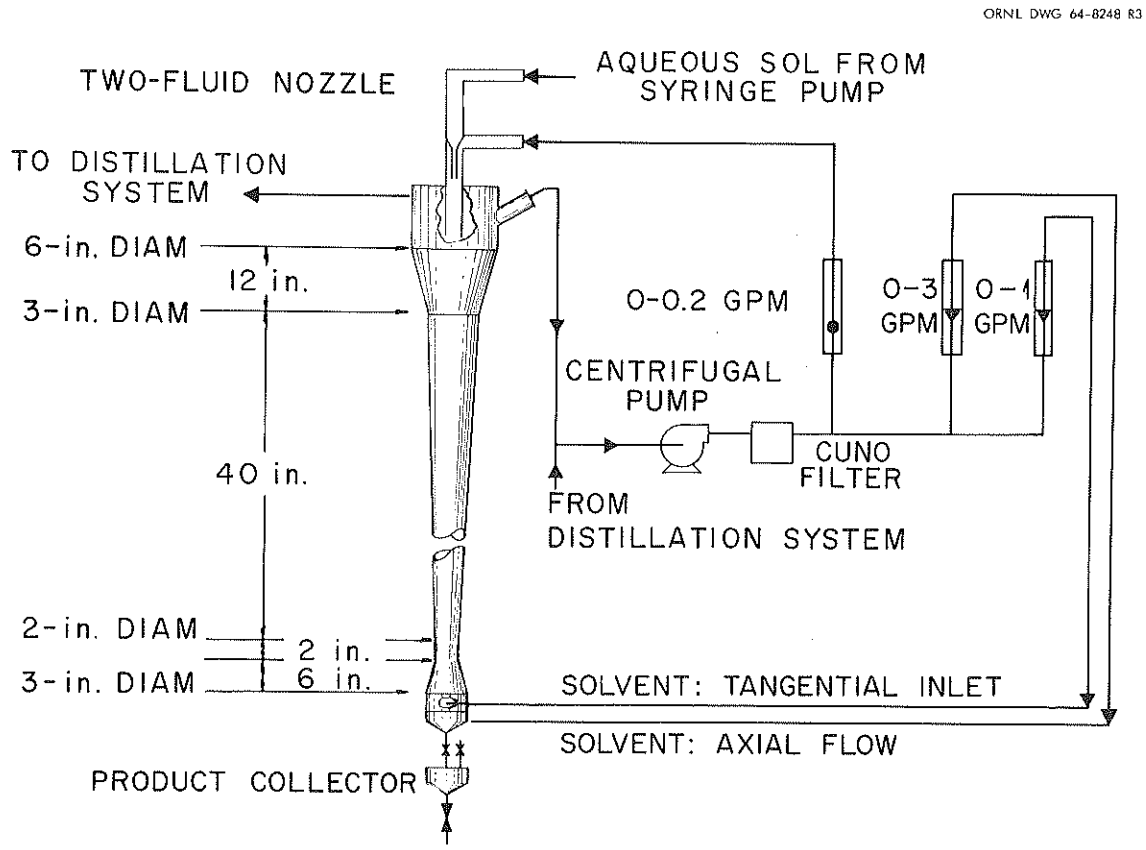

Fig. 8.9. Gel microsphere forming column. Reprinted from reference 24.

chemisorbed species are evolved. Finally, sintering begins above about 600°C. Densities above 90% of theoretical are readily achieved at 1150°C if the proper heating sequence is followed.

Alternatively to the nitrate feed process for making sol-gel microspheres, a variety of other processes may be used. Chloride solutions have been substituted for the nitrate with varying success. Urania sols of much higher molarity have been made, but the fired microspheres sometimes have an undesirably high chlorine content. Other gelation processes have also been used. A process was developed by which hexamethylene tetramine is added to a carbon-bearing sol immediately before formation of spheroids.[31] When these sols are injected into hot paraffin at 90°C, they harden in a few seconds. Spheres 70 to 80% dense were obtained by sintering to 2000°C. Care was required in removing the ammonium nitrate formed on decomposition of hexamethylene tetramine. The explosive nature of ammonium nitrate limits the batch size for the internal gelation process.

8-2.2 Coating Processes

A wide variety of devices has been used for coating particles, including fluidized beds,[2,32–42] entrained beds,[43] and rotary drum coaters.[43] For one or more reasons the last two processes have been abandoned. Thus, discussion will be limited to the fluidized-bed process. Equipment design, operating procedures, and materials selection vary widely, depending upon coating material — whether pyrolytic carbon, oxide, or carbide — and details of coating structure desired.

Further process modifications are dictated by production rate, batch size, and necessity for semiremote or remote operation when recycled fuel is being handled. Since the most important single variable in the coating process is coating material, this section will be divided into subsections on pyrolytic carbon, oxides, and carbides.

Pyrolytic-Carbon Coatings

The process for coating fuel particles with pyrolytic carbon in a fluidized bed involves the pyrolytic decomposition of a hydrocarbon gas at suitable elevated temperatures. Commonly used hydrocarbons include acetylene, methane, propane, propylene, and benzene. All these hydrocarbons are sufficiently unstable that essentially complete decomposition to carbon and hydrogen will occur at useful coating temperatures (above 1000°C). The decomposition processes are complex, and a series of different species of high molecular weight is produced before complete decomposition is achieved.[44] The production of tars and other wastes is a common problem in improperly operated coaters.

Even though decomposition is nearly complete at equilibrium for the hydrocarbons commonly used in coating, the process may be endothermic or exothermic, depending upon the particular hydrocarbon used. Standard heats of formation for various hydrocarbons are shown in Table 8.4. Acetylene decomposition is highly exothermic, whereas methane and propane decompose endothermically. Propylene decomposition is essentially athermal. The absorption or release of energy during decomposition plays an important role in temperature control of a bed during the coating process and must be considered in production scaleup of research-type

Table 8.4. Properties of Gases Used in Pyrolytic-Carbon Coating

Gas	Structure	C_p (298°K) (cal deg^{-1} $mole^{-1}$)	$\int_{298}^{1500} C_p dT$ (kcal/mole)	ΔH_f° (298°K) (kcal/mole)
Helium	He	5.0	6.0	0
Hydrogen	H-H	6.9	8.67	0
Methane	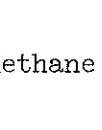	8.5	18.75	−17.9
Ethyne (acetylene)		10.6	19.29	54.2
Ethene (ethylene)	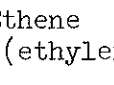	10.6	24.65	12.5
Ethane	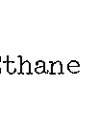	12.5	31.67	−20.2
Propyne (methyl acetylene)	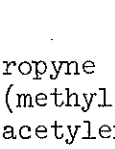	14.7	30.56	44.3
Propadiene (Allene)	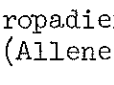	14.2	30.79	45.9
Propene (propylene)	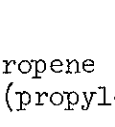	15.5	37.81	4.9
Propane		17.5	45.39	−24.8
1,3 Butadiene	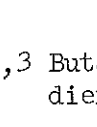	19.1	44.36	26.8
Butane	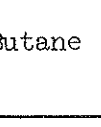	23.6	58.63	−29.8

coaters or in comparing data obtained using different coaters, flow rates, or gas compositions.

The heat contents of reactants and products in a coating process are also important in determining whether or not heating or cooling of the bed occurs during coating. Specific heats and heat contents for various coating gases are also shown in Table 8.4.

From a given hydrocarbon, a wide variety of structures may be produced depending upon temperature, hydrocarbon flux, extent of dilution, gas composition, and coater design.

A schematic diagram of a typical coating apparatus is shown in Fig. 8.10. The coating chamber consists of a graphite reaction tube that is maintained at the coating temperature, generally 1000 to 2200°C, by induction or resistance heating. Helium or another inert carrier gas is admitted to the reaction tube through a nozzle at the bottom at a rate which fluidizes the bed of particles, but does not blow them out the top. The proper flow rate is established prior to pouring a batch of particles in the top of the coater tube. The gas composition is changed by admitting the desired reactant hydrocarbon while the helium supply rate is simultaneously decreased. Flow is generally controlled automatically by electric timers and solenoid switching valves. When multiple coatings are desired, the input gas composition or coating temperature may be shifted abruptly during a run. During the coating process the bed of particles is agitated severely, and each particle is coated with about the same amount of material. Since heat transfer rates are very high in a fluidized bed, thermal gradients are generally very low within the bed of particles. Temperatures are generally monitored with optical pyrometers

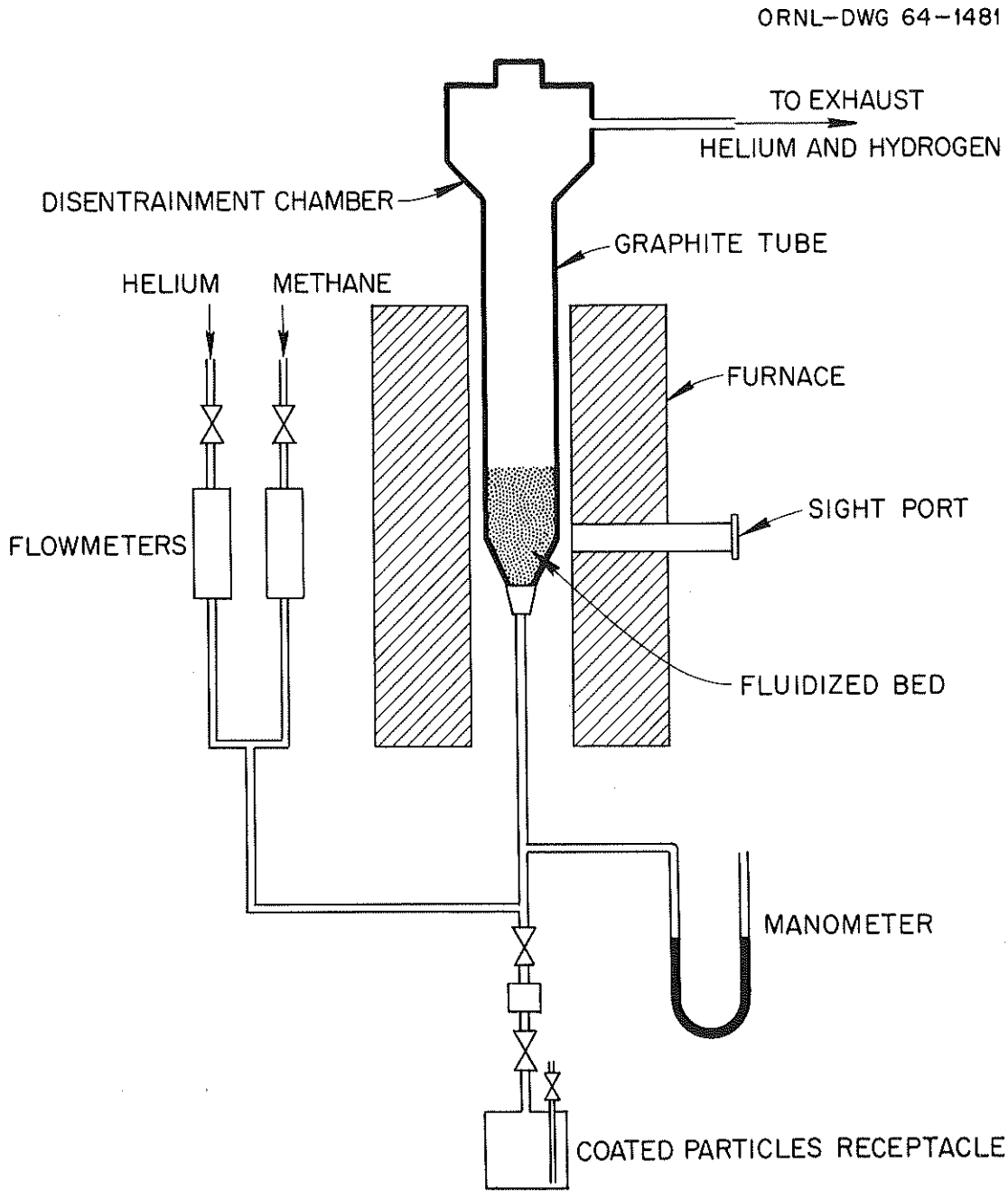

Fig. 8.10. Schematic diagram of a fluidized-bed coated. Reprinted from reference 45.

through ports in the side of the furnace or the top of the coater. When the desired coating has been achieved, the flow is reverted to pure inert carrier gas. Particles may be removed by lowering the flow so that they fall out the bottom if the gas inlet orifice is large enough or by lowering a suction tube into the fluidized bed and withdrawing particles out the top into a collector.

When the hydrocarbon is pyrolytically decomposed, carbon and hydrogen are produced. Problems arise in handling the off-gas because of the explosive potential of hydrogen-air mixtures. There are also problems associated with the deposition of carbon on the walls of the reactor tube and at the inlet nozzle. Furthermore, under certain conditions large amounts of soot are produced and must be considered in the coater design.

Important variables in the design of the coater are the shape of the inlet nozzle and of the cone at the inlet to the reactor tube. The cone nozzle, which is generally in the range 30 to 90° included angle, affects the refluxing action of the fluidized bed, the tendency for plugging by soot, and the gas flow distribution in the bed. The exact nature of these effects is not well established, but because of them the structures produced in coaters of different designs may vary even though the nominal coating conditions of temperature, gas composition, and flow rate are the same.

Pilloton has shown that the minimum flow rate for fluidization in a uniform tube is approximated by this expression:[45]

$$G_{mf} = 2.04 \times 10^{-6} \frac{D^2}{\mu} g \, (\rho_s - \rho_f) \, \rho_f \, , \qquad (1)$$

where

G_{mf} = gas flow rate, g hr^{-1} cm^{-2} ,

D = particle diameter, μ ,

μ = gas viscosity, centipoises ,

g = gravity acceleration, cm/sec^2 ,

ρ_s = density of the particles, g/cm^3 , and

ρ_f = density of the gas, g/cm^3 .

Several complicating factors arise which make difficult a quantitative description of the actual conditions. Since the gas is heated as it enters the reaction chamber, its velocity and viscosity change markedly. Furthermore, the gas composition changes as a result of the cracking of the hydrocarbon. The bed may be heated or cooled by the cracking process depending upon whether the reaction is endothermic or exothermic. Finally, as the particle diameter increases as the coating is applied, the average density decreases. For these reasons gas flow velocities are established empirically for a given coating, hydrocarbon, and temperature of operation. Generally the inlet gas flow rate is much higher than that given in Eq. (1) so that the bed is actually a spouting bed instead of a fluidized bed.

Some differences in procedure are noted when oxide kernels are used instead of carbide. Since uranium dioxide will react rapidly with carbon above about 1500°C, a sealer layer must be applied at a lower temperature. This layer retains CO formed by the reaction between the oxide kernel and the carbon coating so that equilibrium is established and further reaction ceases. Coatings can then be applied at higher temperatures without further visible reaction. For coatings applied at 2000°C, greater

migration of uranium through the coating is seen in carbide kernels than for oxide kernels.[42] This migration results in surface contamination and higher fission-gas release during irradiation.

Oxide Coatings

High-density Al_2O_3 and BeO coatings have been applied to UO_2 fuel particles by the hydrolysis of the appropriate metal chlorides.[34] Alumina is porous when applied between 500 to 900°C and fully dense when applied at 1000 to 1100°C. The coating reaction is

$$2\ AlCl_3(g) + 3\ H_2O(g) = Al_2O_3(s) + 6\ HCl(g)\ . \qquad (2)$$

The process of coating with beryllium oxide is similar except that deposition temperatures of 1300 to 1400°C are used. Other oxides looked at briefly were MgO and ZrO_2.

The coating process for forming oxides is similar to that for pyrocarbon except ceramic oxide reactor vessels are used and the acids in the off-gas lines must be accommodated.

Silicon Carbide Coatings

Silicon carbide was formerly deposited on static substrates by the simultaneous thermal reduction or decomposition of various compounds independently containing silicon and carbon. During the last two decades, however, a family of methylchlorosilanes has become commercially available which, by combining the carbon and silicon in a single compound, offer a simplified process. One of these compounds, methyltrichlorosilane (CH_3SiCl_3), has been used almost exclusively for fluidized-bed deposition of SiC coatings,[18,42,46–50] though one recent study has employed methyldichlorosilane (CH_3SiHCl_2).[51]

The characteristics of SiC coatings are influenced by variations in fabrication parameters, but their sensitivity to these variables is not nearly so great as that of pyrolytic carbon. Silicon carbide is deposited in the range from 1200 to 1800°C. The reaction is carried out in the presence of excess hydrogen which also serves as a carrier gas for the above-mentioned reactants, which are liquid at ambient conditions. The fabrication parameters can readily be adjusted to produce SiC coatings of near theoretical density, though particular care must be exercised to avoid deposition of free silicon near the lower end of the temperature range.

Control of the vapor flux or partial pressure of the reactant can be obtained by use of an evaporating apparatus such as that shown in Fig. 8.11. A carrier gas is supersaturated relative to a control temperature by passage over a heated bath of reactant and is then passed through a controlled-temperature reflux condenser to produce the desired concentration.

Components of a SiC deposition apparatus as well as the material being coated must be able to withstand a hot HCl atmosphere.

8-2.3 Fuel Element Fabrication

In fuel elements, coated particles may be loose or bonded. Loose beds of particles have the advantages of ease of manufacture and low cost, since the particles are simply poured into holes machined into graphite parts. Fear of an accident, in the reactor or during shipping after irradiation, whereby the radioactive particles would spill out and cause gross contamination has, however, precluded the use of loose beds up to now.

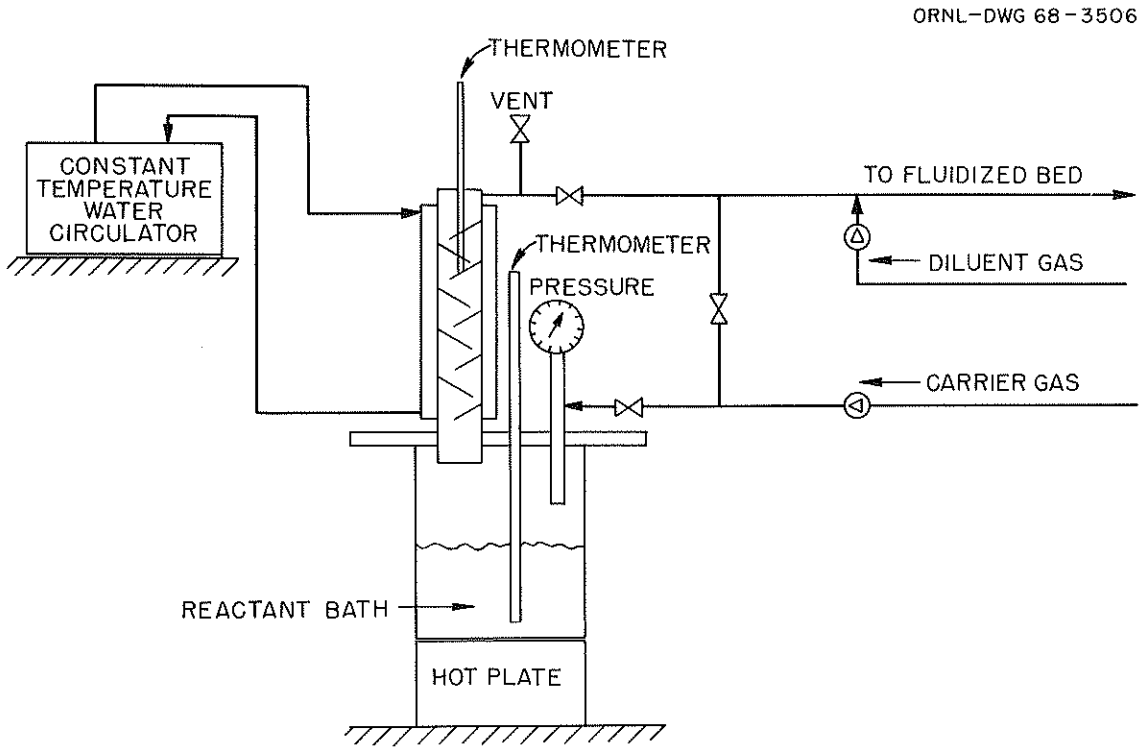

Fig. 8.11. Liquid reactant evaporating apparatus. Submitted by Oak Ridge National Laboratory, July 1968.

Bonded beds consist of coated particles and carbon flour bonded with a suitable agent, such as pitch, furfuryl alcohol, or a phenolic resin. Fabrication techniques include cold pressing, warm pressing, hot pressing, extrusion, and mold injection followed by curing and baking cycles for the particular bonding agent employed if these cycles were not part of the basic forming scheme as they are in hot pressing. Bodies have been fabricated in the form of solid or hollow cylinders for the Peach Botton, UHTREX, and Dragon Reactors and as spheres for the German Pebble-Bed Reactor (AVR). The fuel element for the Fort St. Vrain-HTGR consists of bonded, closely packed beds of coated particles in fuel holes interspaced with coolant holes in a hexagonal block of graphite. A description of the fuel elements and operating conditions for these reactors is given in Table 8.5. Typical fueled graphite elements are illustrated in Figs. 8.12 to 8.16.

The two major problems associated with fabricating elements containing coated particles are fuel homogeneity and the damaging of coated particles during fabrication. Fuel homogeneity is obtained by careful control of blending and molding techniques. Overcoating the particles with the matrix ingredients before pressing improves fuel homogeneity but is most effective for low volume loadings of coated particles. Since damage to coatings can occur during the pressing operation, particularly for high fuel loadings and weak particle coatings, care must be exercised to avoid excessive pressures. The effect of isostatic forming pressure on damage rate is shown graphically in Fig. 8.17 for laminar coated particles (coating thickness approximately 100 μ) as a function of fuel loading. Pressures as high as 6000 psi are acceptable for loadings up to 21 vol %.

Table 8.5. Summary of High-Temperature Gas-Cooled Reactors Utilizing Coated-Particle Fuel

	Peach Bottom HTGR	PSC[a] HTGR	DRAGON Reactor	AVR	UHTREX	AGR
Reactor type	Prototype	Power demonstration	Experimental	Prototype	Experimental	(no specific plant)
Criticality date	March 1966 (electricity produced on January 27, 1967)	(Scheduled for 1971)	August 1964 (full power on April 24, 1966)	August 1966	(Scheduled for 1967)	
Thermal power, Mw	115	837	20	46	3	
Net electric power, Mw	40	330	None	15	None	
Coolant	Helium	Helium	Helium	Helium	Helium	CO_2
Inlet temperature, °C	350	400	350	180	870	
Outlet temperature, °C	750	785	750	850	1300	
Pressure, atm	24	48	20	10	34	20
Moderator	Graphite	Graphite	Graphite	Graphite	Graphite	Graphite (metal clad)
Fuel	Pyrolytic-carbon (PyC)-coated $(Th,U)C_2$ particles in hot-pressed, graphite-matrix compacts (2.75-in. OD × 1.75-in.-ID × 3 in. long)	Buffer-isotropic PyC-coated $(Th,U)C_2$ and ThC_2 particles in packed beds	PyC-coated (Zr,U)C and PyC-SiC-PyC-coated $(Th,U)C_2$ and UC-10 particles in warm-pressed, resin-bonded, graphite-matrix, annular fuel compacts (1.7-in.-OD × 2.1 in. long)	Duplex PyC-coated $(Th,U)C_2$ particles in graphite spheres	Triplex PyC-coated UC_2 particles in extruded graphite cylinders	PyC-SiC-PyC-coated UC or UC_2 particles in a SiC matrix
Fuel elements	Low-permeability graphite tubes (3.5 in. OD) containing 7.5-ft columns of fuel compacts	Hexagonal graphite blocks (14 in. across flats × 31 in. long) containing bonded channels of fuel particles interspaced with coolant channels	Seven-rod clusters of low-permeability graphite tubes containing 63-in. columns of fuel compacts	Machined graphite spheres (6 cm OD × 4 cm ID) filled by injection molding with carbonaceous matrix containing dispersed coated particles	Graphite cylinders (1 in. OD × 0.5 in. ID × 5.5 in. long)	Dense self-bonded SiC rods containing up to 40 vol % coated particles
Coated-particle loadings in compacts or beds, vol %	22–28	60–65	12 (fissile); 24 (fertile)	22	8–27	Up to 40
Heat removal from fuel elements	External	Internal	External	External	Internal	External
Fission-product purge system	Yes	No	Yes (Charge I); driver fuel elements only (Charge II)	No	No	No
Core power density, average, kw/liter	8.3	6.3	14	≈3	1.3	
Fuel temperature, °C						
Maximum	1330	1260	1250	1250	1590	≈1000–1100
Average	980	815			1430	
Minimum	570	480			1080	
Fuel burnup, % FIMA[b]						
Fissile particles, max	14	20	Charge I: 4.5 Charge II: 35–70	14 (average)	13 in 1 year (100% plant factor)	5
Fertile particles, max	7	7	Charge I: < 1 Charge II: 3–6	None	None	None
Fast-flux exposure, neutrons/cm^2 (E > 0.18 Mev)						
Maximum	4.7×10^{21}	8.5×10^{21}	2.2×10^{21} (E > 0.1 Mev) per year	7.6×10^{21} (E not specified)	1×10^{21} in 2 years	
Average	3.6×10^{21}	5.5×10^{21}	1.7×10^{21} (E > 0.1 Mev) per year		≈0.7×10^{21} in 2 years	
Fuel lifetime, year	3	6	Various (experimental)	5.4	Not specified	

[a] Public Service Company of Colorado.

[b] Fissions per initial metal atom.

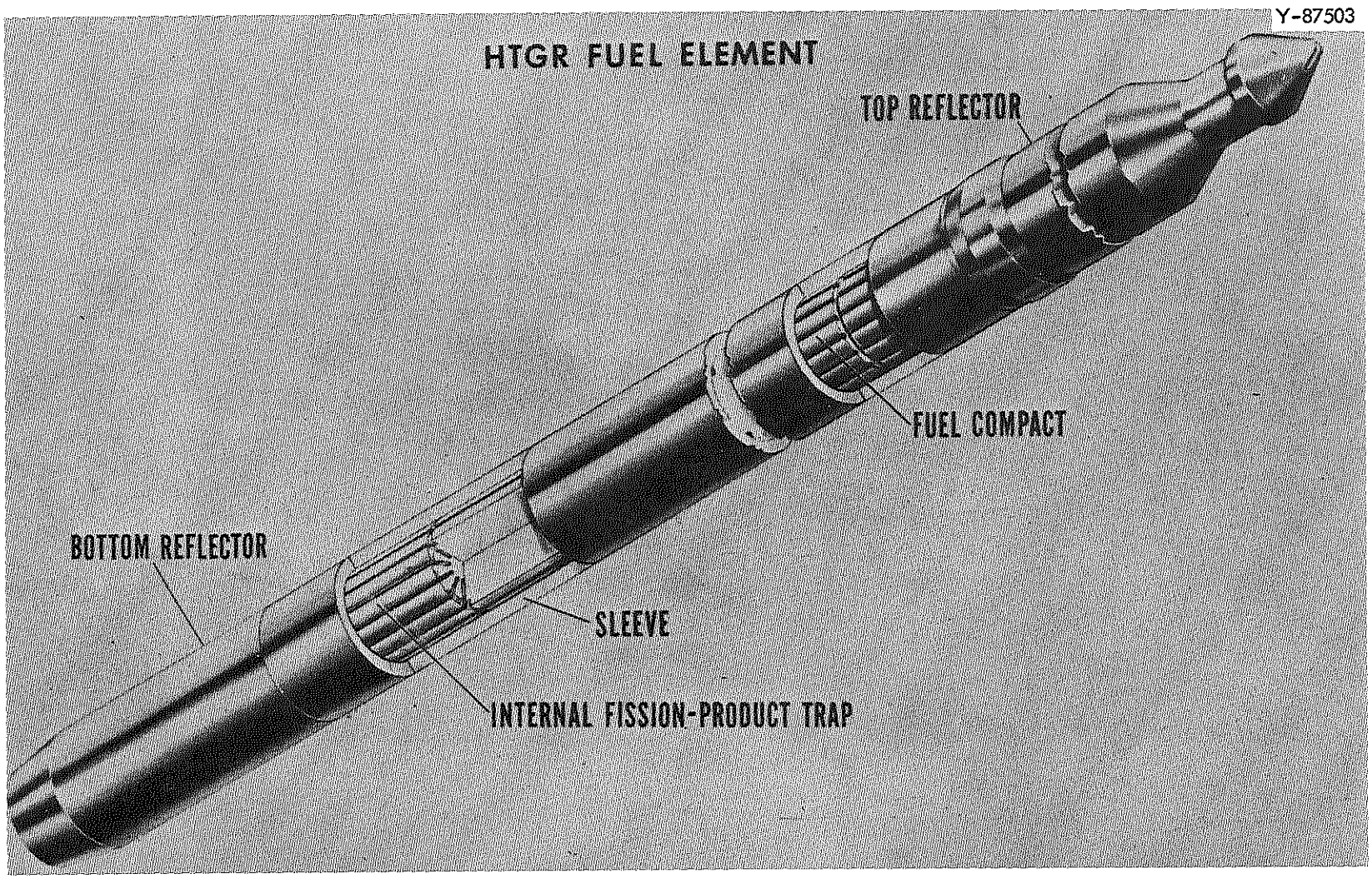

Fig. 8.12. Peach Bottom fuel element. Reprinted from reference 52.

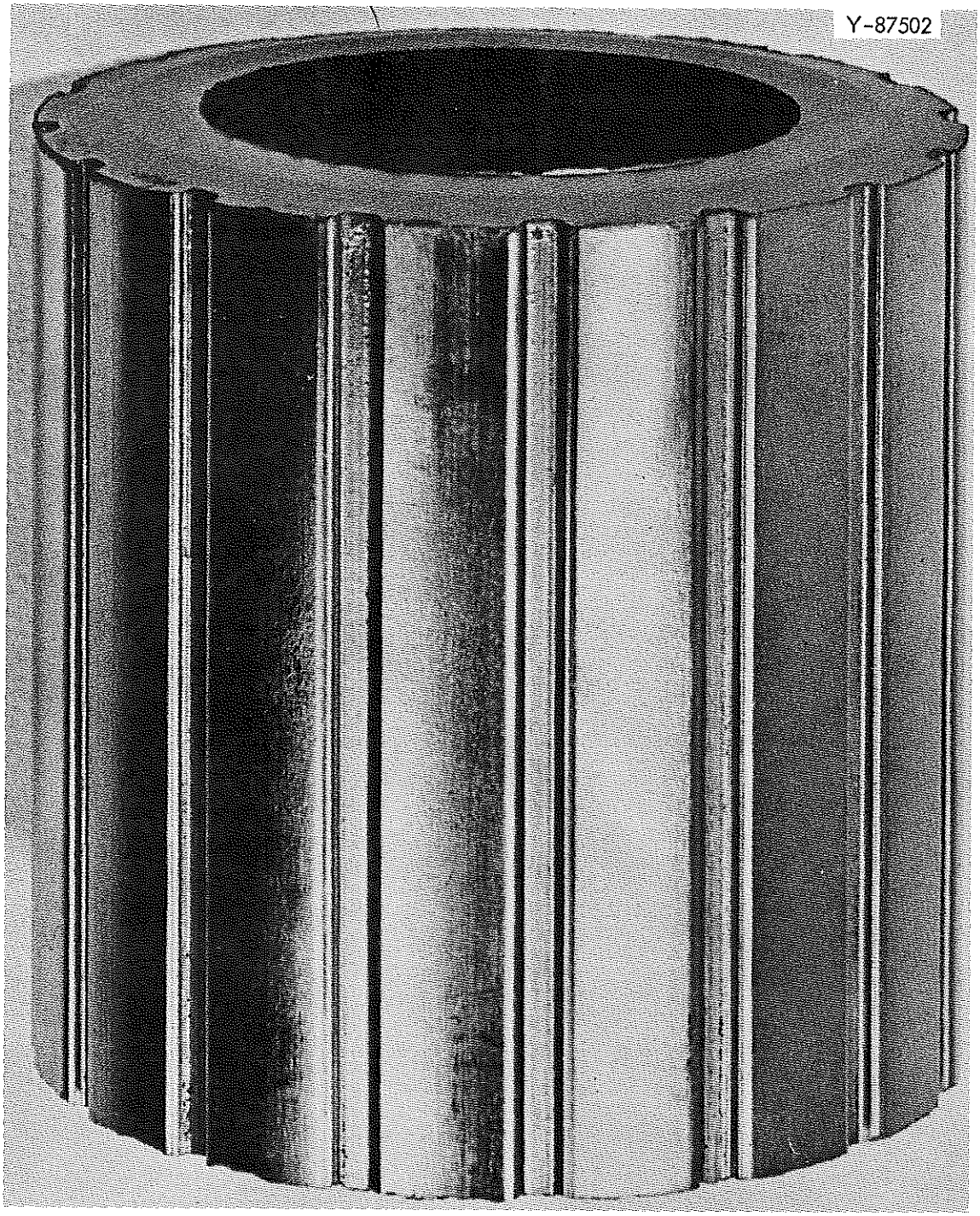

Fig. 8.13. Hot-pressed, graphite-matrix fuel compact for the Peach Bottom HTGR. Coated particles are uniformly dispersed in the 2.75-in. o.d. × 1.75-in. i.d. × 3.0-in.-long compacts. Reprinted from reference 52.

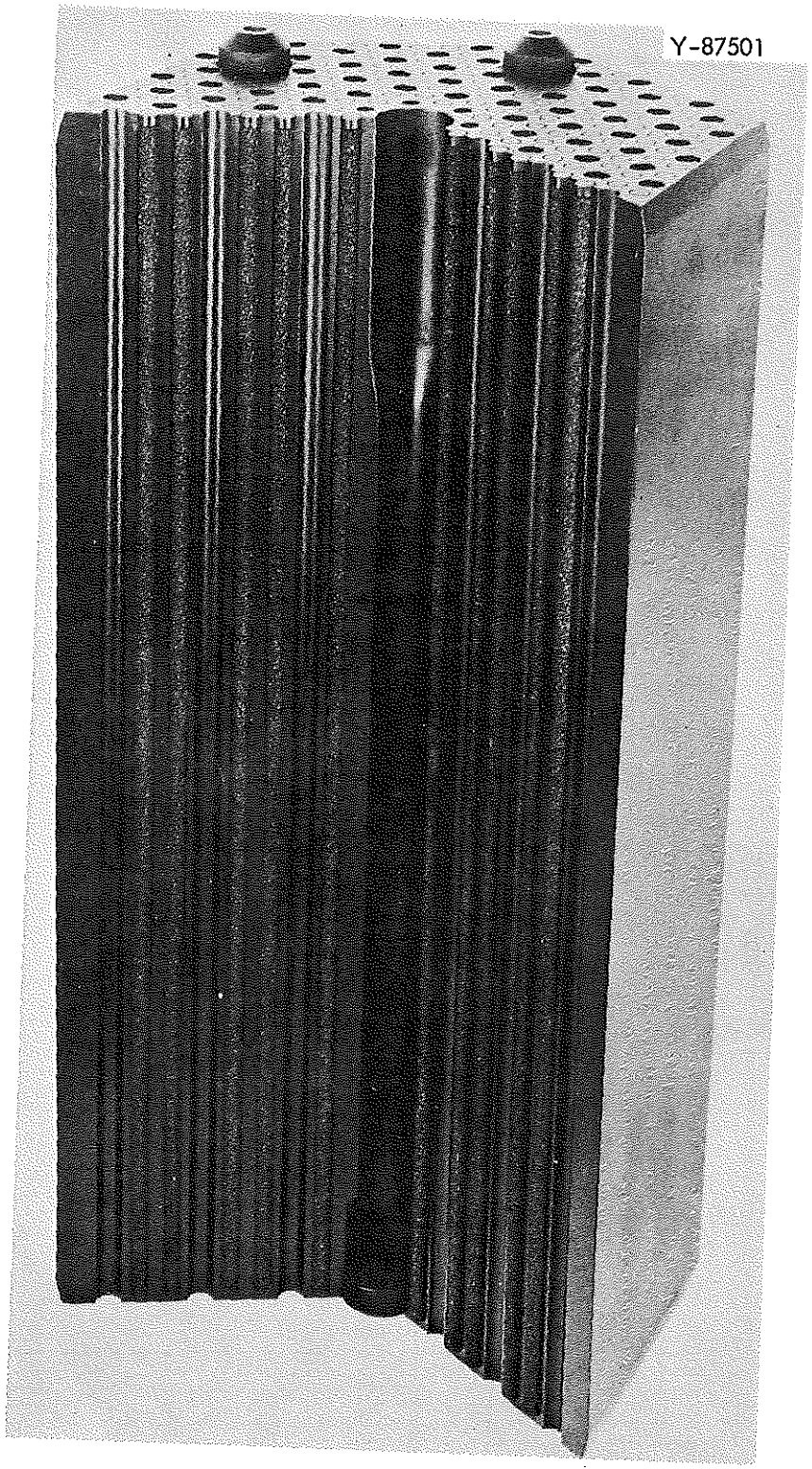

Fig. 8.14. HTGR hex block fuel element showing channels of coated-particle fuel interspaced with coolant channels. The fuel element is 31 in. tall and 14 in. across the flats. Reprinted from reference 52.

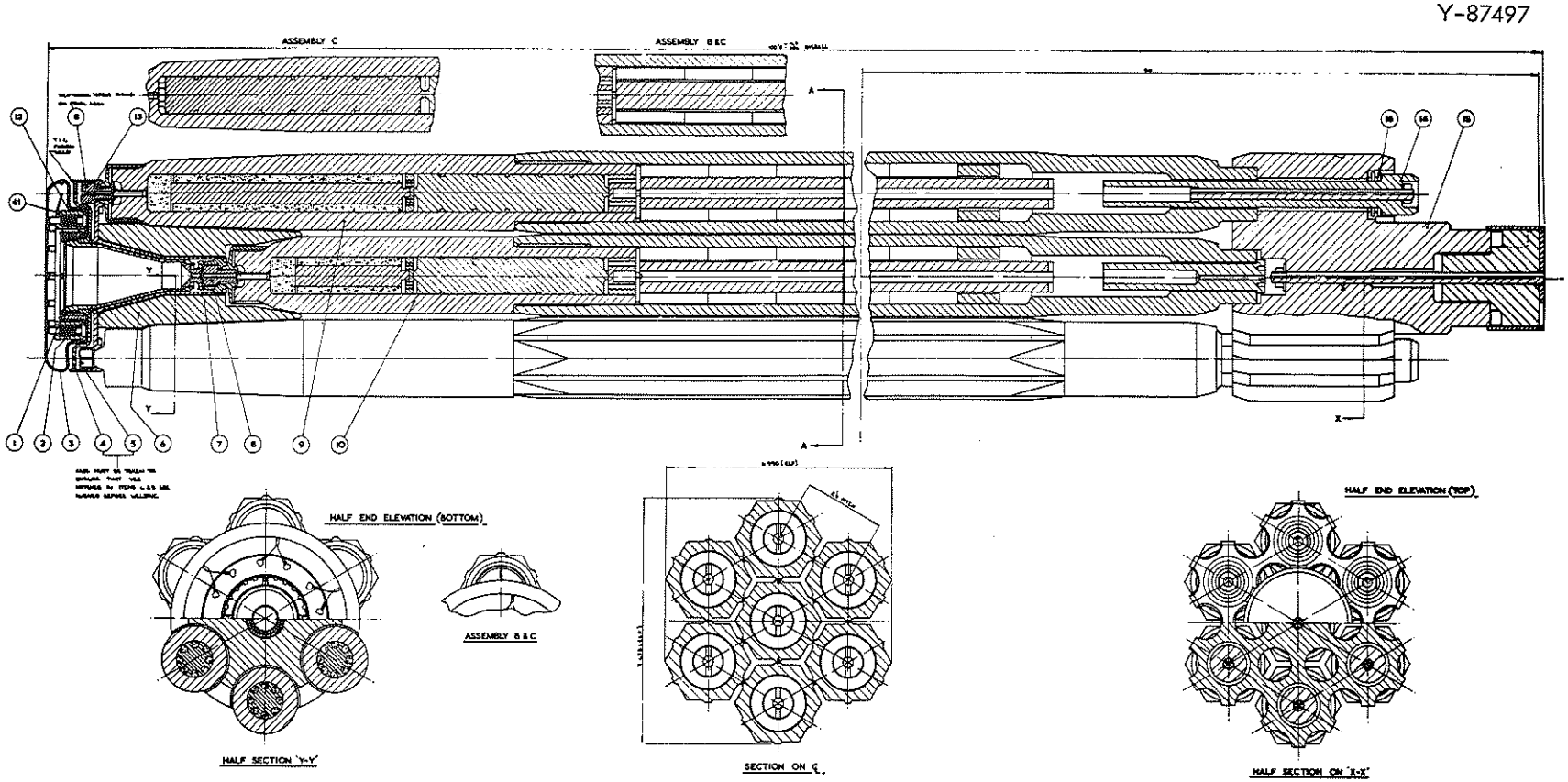

Fig. 8.15. DRAGON fuel element: a cluster of seven low-permeability graphite tubes containing annular fuel inserts. Reprinted from reference 38.

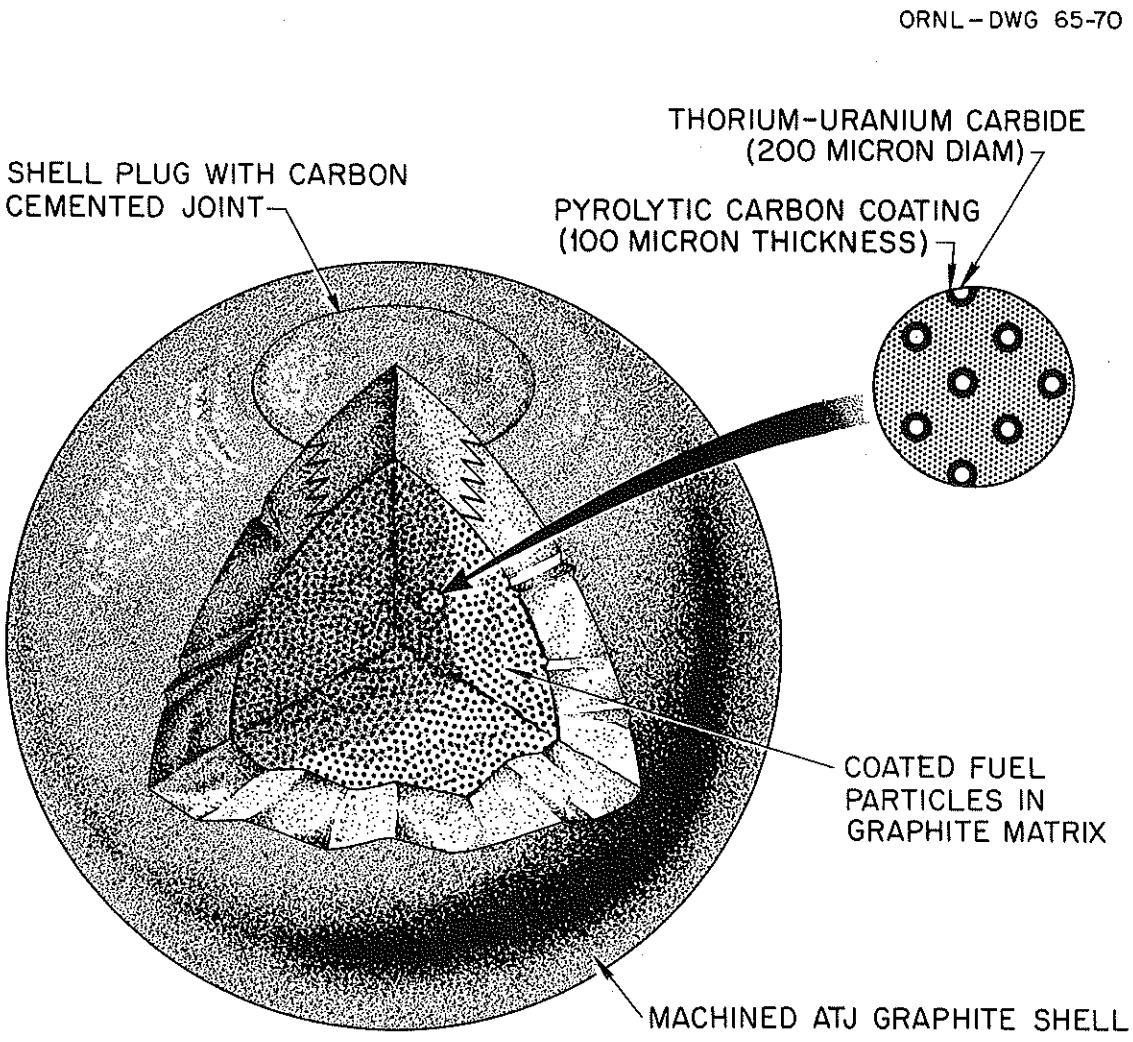

Fig. 8.16. Spherical AVR fuel element consisting of dispersion of coated-fuel particles in a carbonaceous matrix contained within a machined graphite shell. The sphere is 6 cm in diameter. Reprinted from reference 19.

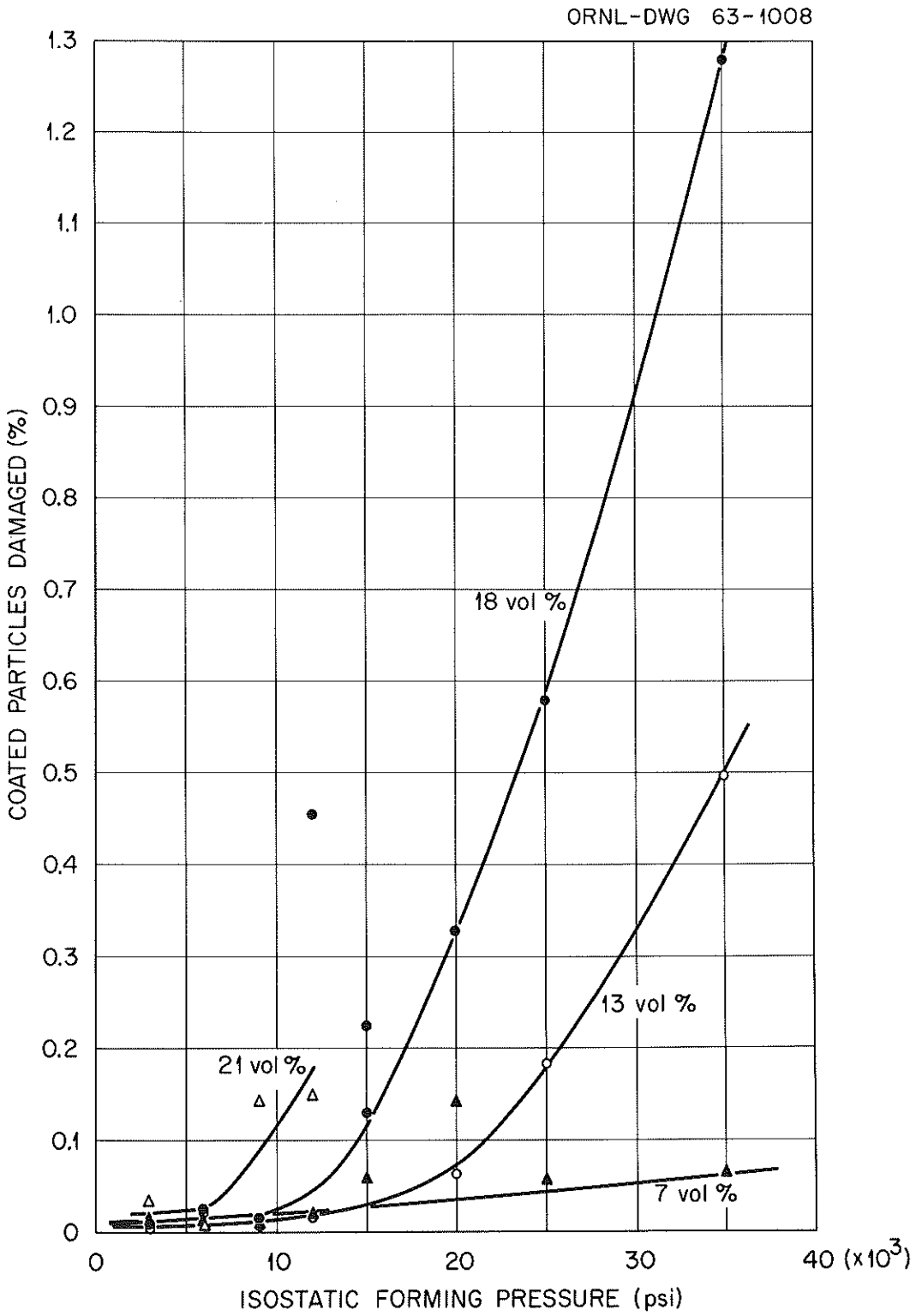

Fig. 8.17. Effect of isostatic forming pressure and fuel concentration on damage to laminar-pyrolytic-carbon-coated particles in graphite matrices. Reprinted from reference 53.

Since the fabrication conditions leading to little damage to coated particles are not those leading to the optimum strength and thermal conductivity, compromise is unavoidable. Fortunately, volume heat generation rates are low so that thermal stresses and temperature gradients are generally low and matrix properties inferior to those of graphite can be tolerated. Because of limited experience and because of the great number of variables in fuel body fabrication, comprehensive tabulation of properties of various fueled graphite bodies is not of great value. The data on fuel compacts for the Peach Bottom HTGR shown in Table 8.6 are typical of the properties that can be achieved.[17]

Table 8.6. Typical Properties of Graphite-Matrix Fuel Compacts

Graphite density	1.90–1.95 g/cm^3
Crushing strength:[a]	
Transverse	8500 psi
Longitudinal	7500 psi
Thermal expansion[a] (to 1000°C):	
Transverse	7.5×10^{-6}/°C
Longitudinal	2.25×10^{-6}/°C
Thermal conductivity at 2000°C, radial	0.3 w cm^{-1} °C^{-1}
Electrical resistivity	3.5×10^{-3} ohm-cm
Permeability (He at 1 atm)	2×10^{-3} cm^2/sec
Pore structure	< 1% of porosity due to pores > 1 μ in diameter
Radiation stability	< 0.1% contraction after 6×10^{19} fissions/cm^3 at 1100 to 1500°C

[a]Direction with reference to grain orientation.

8-3 PROPERTIES OF PYROLYTIC-CARBON COATINGS

The mechanical and thermal properties of pyrolytic-carbon coatings deposited in fluidized beds vary with coating temperature, coating hydrocarbon gas, hydrocarbon flux and partial pressure, bed volume, and coater geometry. Thus, coatings with a wide variety of properties may be produced, and this flexibility is one of the greatest advantages of pyrolytic-carbon coatings.

8-3.1 Structural Features and Physical Properties

Originally, the examination of microstructures was the primary method for characterizing coatings, and terms such as laminar, columnar, and featureless coatings were used. Laminar coatings have a characteristic onionskin appearance shown in Fig. 8.18. Columnar coatings are similar to massive pyrolytic carbon, and growth cones are visible as shown in Fig. 8.19. Featureless coatings are isotropic and, unlike the other two, do not respond to polarized light. A coating of this type is shown in Fig. 8.20.

But since coatings with similar appearance may vary widely in properties, the crude microstructural designations have given way to more precise characterization in terms of density, anisotropy, and crystallite size. Coating densities are measured on coatings cracked off particles or on disks stripped from graphite substrates coated simultaneously with a batch of particles. To be representative, these disk coatings must have the same thickness and appearance as the particle coatings. Densities are measured with a helium pycnometer or by a sink-float technique, generally with mixtures of methyl alcohol and tetrabromoethane.

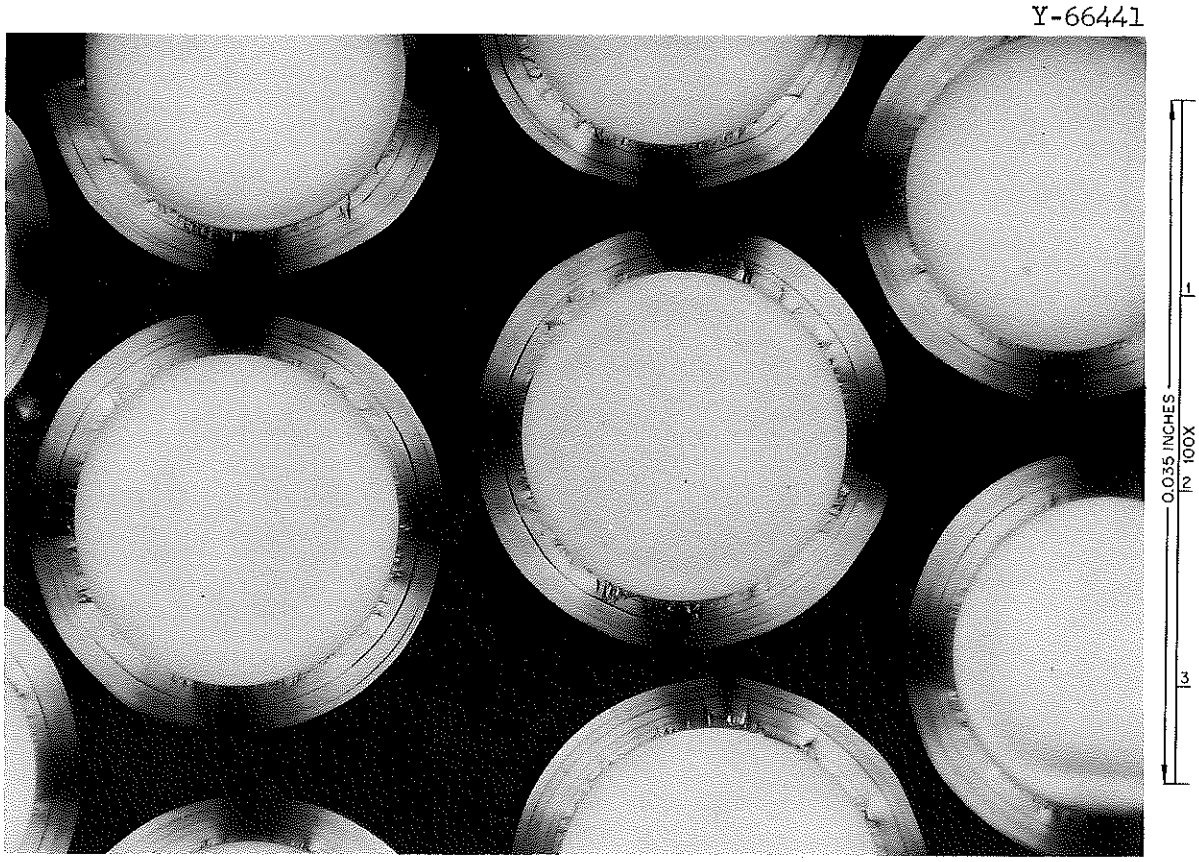

Fig. 8.18. Polarized light photomicrograph of laminar pyrolytic carbon on ThO_2 microsphere. As polished. Submitted by Oak Ridge National Laboratory, July 1968.

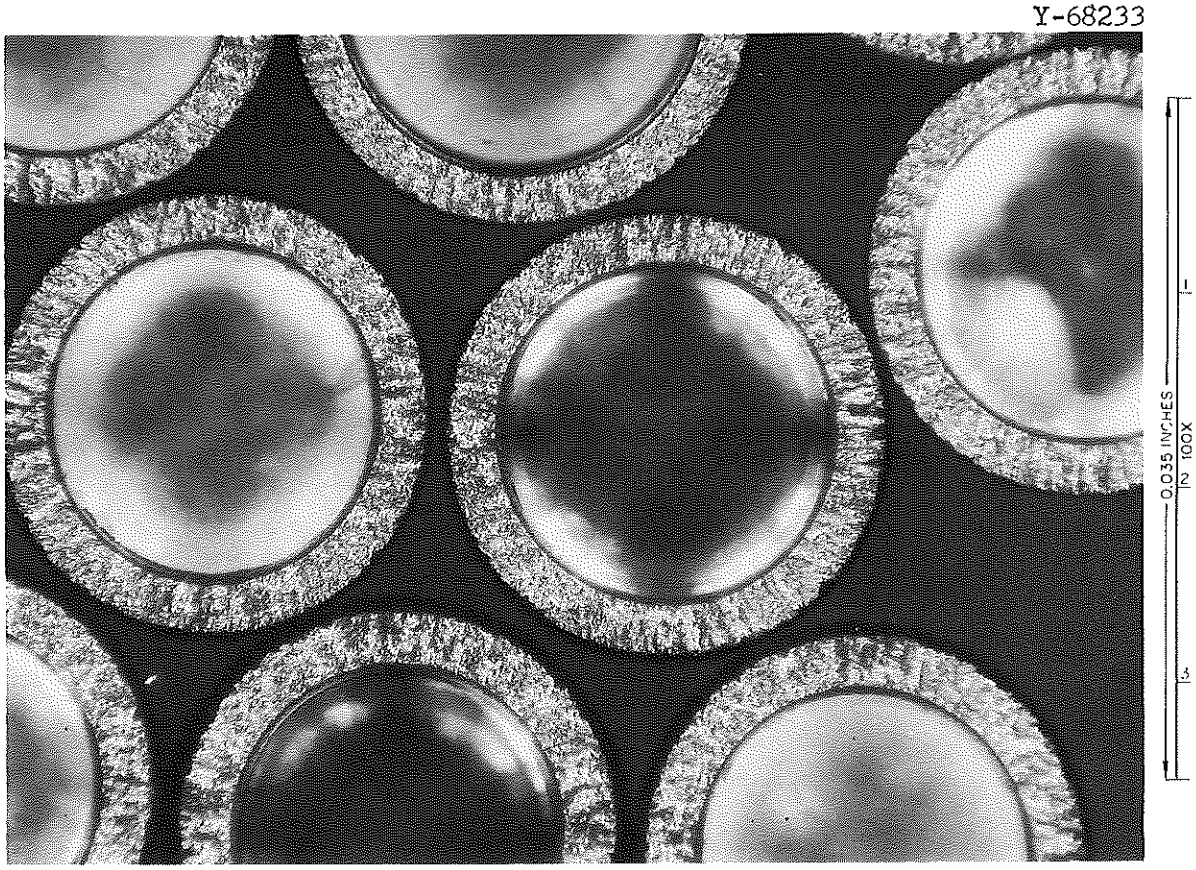

Fig. 8.19. Polarized light photomicrograph of columnar pyrolytic carbon on ThO_2 microsphere. As polished. Submitted by Oak Ridge National Laboratory, July 1968.

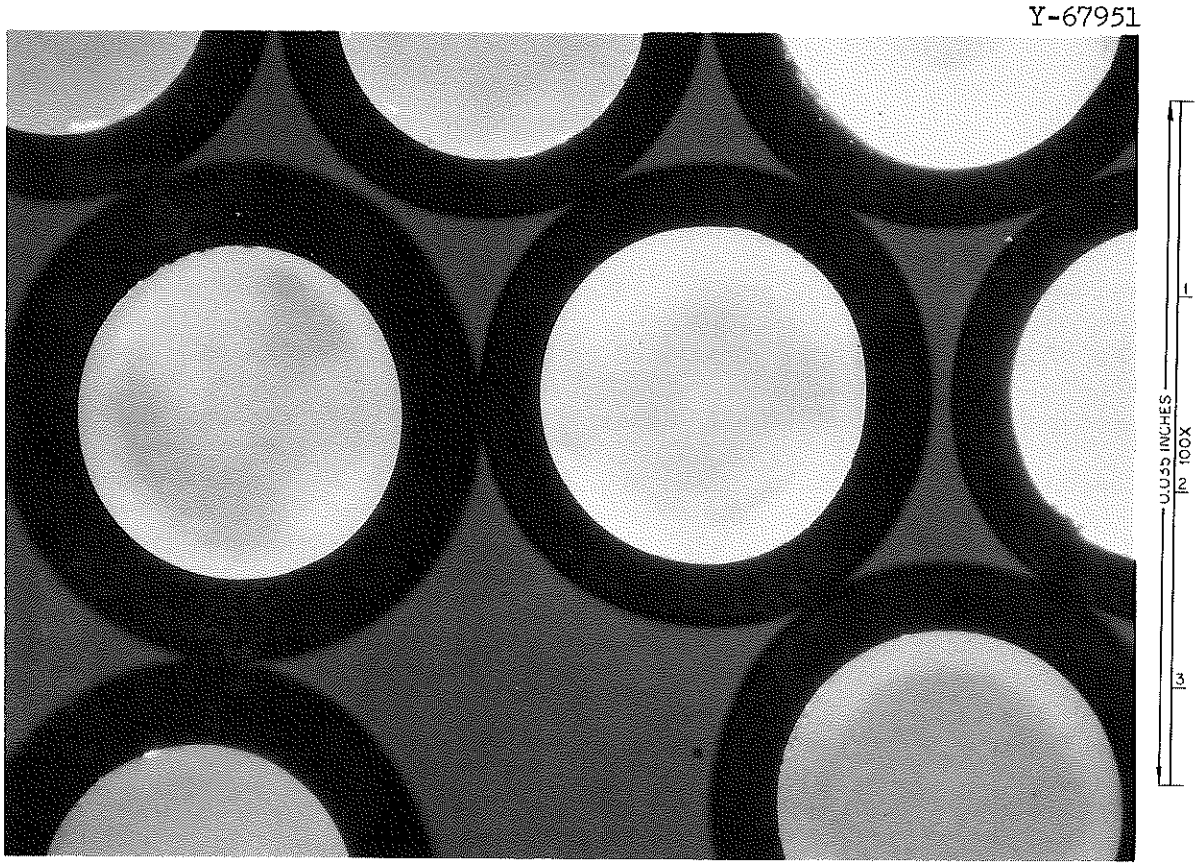

Fig. 8.20. Polarized light photomicrograph of featureless pyrolytic carbon on ThO_2 microsphere. As polished. Submitted by Oak Ridge National Laboratory, July 1968.

Crystallite size and anisotropy of pyrolytic-carbon coatings are measured by x-ray techniques. The crystallite size is measured from the line breadth of the (00.2) reflection from a bed of coating fragments. The apparent crystallite size perpendicular to the basal plane is then calculated using the relation

$$L_c = \frac{0.89\ \lambda}{(\beta \cos \theta)} \tag{3}$$

where λ is the wavelength of the incident x rays, β is the width at half height in 2θ radians of the (00.2) reflection corrected for sample thickness, and θ is the Bragg angle. Anisotropy measurements are made on flat disks of pyrolytic carbon deposited on graphite substrates in a bed of coated particles. The method, described by Bokros,[40] involves the use of Bacon's[54] fiber-texture technique which yields the relative number of (00.2) poles per unit solid angle at the angle ϕ with the normal to the substrate. The symmetry around the normal to the substrate allows the data to be presented as a single distribution curve, $I(\phi)$ vs ϕ. The Bacon Anisotropy Factor (BAF), σ_{oz}/σ_{ox}, which is the ratio of the thermal expansion coefficients in the perpendicular and parallel directions with respect to the deposition surface is given by

$$\sigma_{oz}/\sigma_{ox} = \frac{2\int_0^{\frac{\pi}{2}} I(\phi) \cos^2 \phi \sin \phi \, d\phi}{\int_0^{\frac{\pi}{2}} I(\phi) \sin^3 \phi \, d\phi} . \tag{4}$$

This relationship was derived by assuming the thermal expansion coefficient in the direction parallel to the basal planes of pyrolytic carbon single crystals to be zero.

The effects of deposition temperature and methane flow rate on the properties of coatings deposited from methane are shown in Fig. 8.21 from the work of Beatty et al.[39] The fuel particles for these determinations were UC_2 microspheres with a mean particle diameter of 188 μm and a measured density of 10.7 g/cm^3. Below 1500°C a 3/4-in.-ID reaction tube was used with batches of 10 g (300 cm^2 surface area); above 1500°C a 1-in.-ID tube was used with batches of 25 g (750 cm^2). The total flow rate was 760 cm^3/min for low-temperature runs and 2500 cm^3/min for high-temperature runs. The total coating thickness was 50 μm for each run. The results should be considered specific to these conditions and serve primarily to illustrate the range of properties which may be achieved.

The density contour map in Fig. 8.21 shows that a low-density range extends from 1300 to 1500°C with the minimum densities occurring at 1400°C at supply rates between 0.13 to 0.20 cm^3/min per cm^2 of particle surface. The density increases at lower or higher supply rates and coating temperatures. Maximum densities are above 2.0 g/cm^3.

The anisotropy contour map shows that very anisotropic coatings form at low supply rates and high temperatures and at intermediate supply rates and low temperatures. At supply rates above 0.2 cm^3/min per cm^2 of particle surface the anisotropy decreases with increasing supply rate. The variation in anisotropy with coating conditions is illustrated dramatically by the varying responses of the different coatings to polarized light, as is shown in Fig. 8.22. Anisotropic coatings show a characteristic "Maltese Cross" when examined under polarized light, whereas isotropic coatings are uniformly gray. Thus, metallography can be used for semi-quantitative evaluation of anisotropy. The contour map for apparent

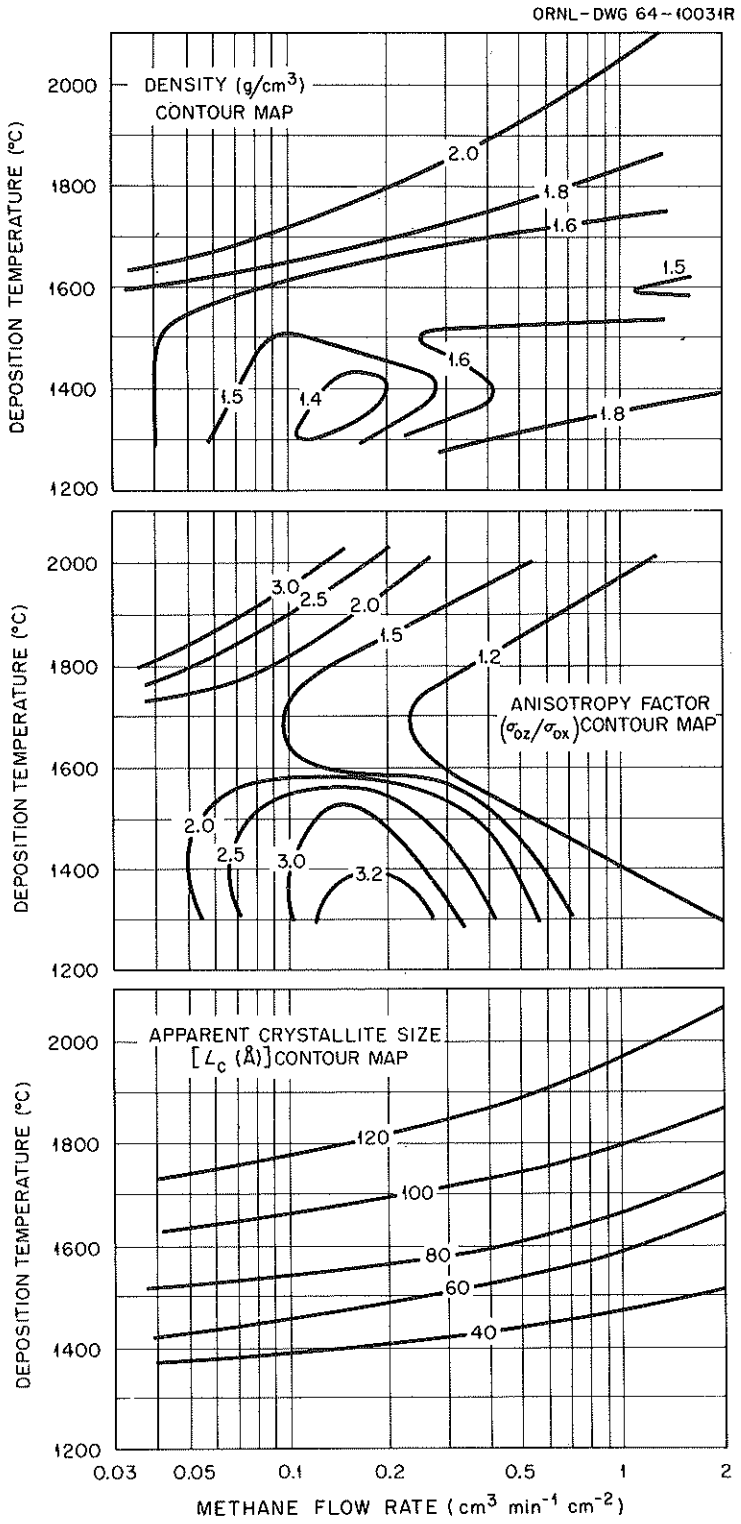

Fig. 8.21. Effect of deposition conditions on properties of 50-μ-thick pyrolytic-carbon coatings deposited from methane in a fluidized bed. Reprinted from reference 39.

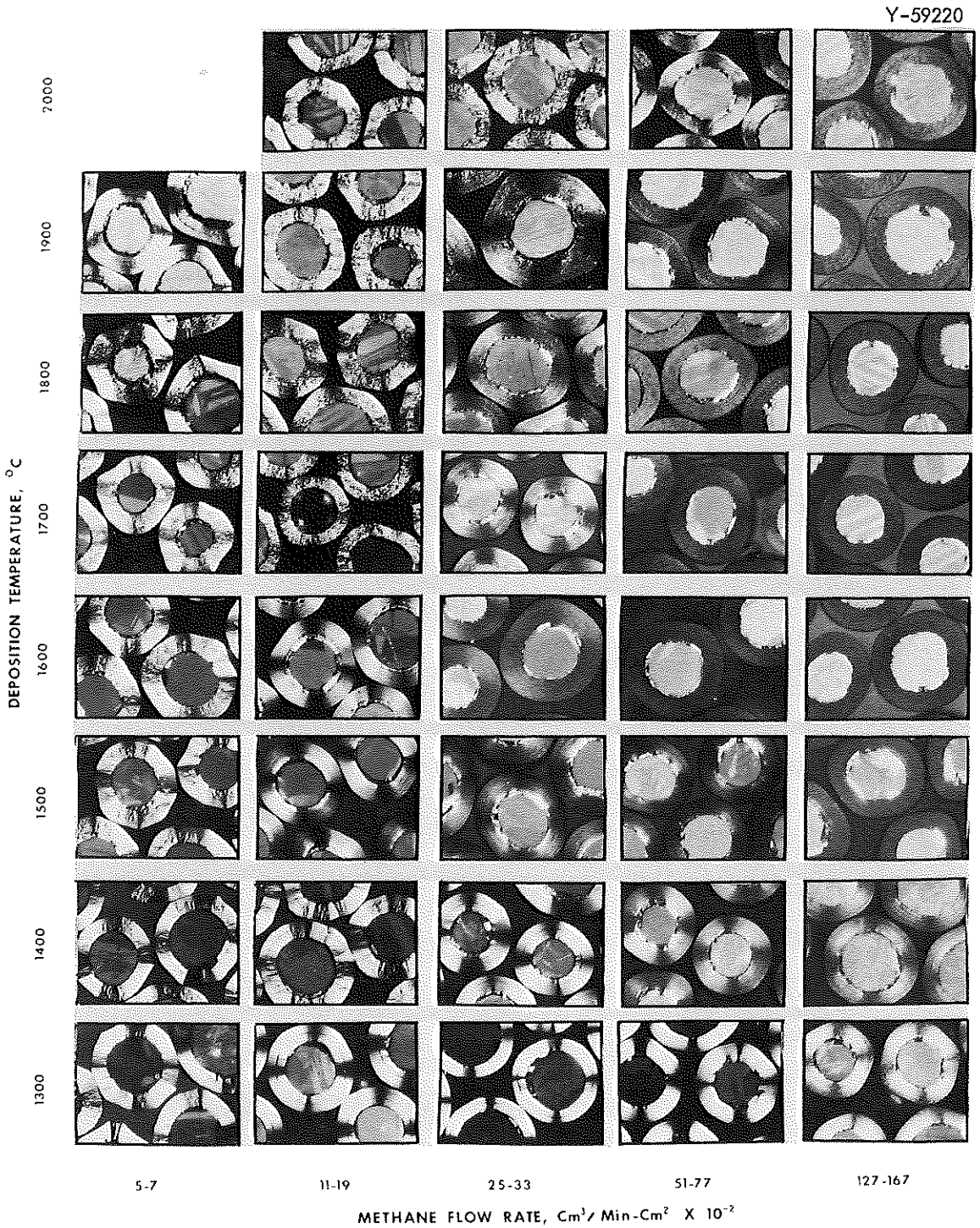

Fig. 8.22. Effect of deposition conditions on microstructure of 130-μ-thick pyrolytic-carbon coatings deposited on UC_2 particles in a fluidized bed, as polished, polarized light. Reprinted from reference 39.

crystallite size (Fig. 8.21) shows that this parameter is primarily a function of coating temperature and is much less dependent on flow rate.

Results similar to those of Beatty et al.[39] were obtained by Bokros,[40] who also used methane-helium mixtures. Some qualitative differences are noted, but these are to be expected with a different coater design, flow rate, and different technique for measuring bed temperature. Hewette and Beatty[55] produced with methane in a 2-in. coater coatings with properties very similar to those of Beatty et al.[39] simply by increasing the total gas flow rate by a factor of 4. Beatty also produced similar coatings with propane and propylene in a 1-in. coater.[56,57] With these latter reactants, much higher carbon supply rates were possible in the fluidized bed, and high density coatings were achieved at average deposition rates as high as 10 μ/min — five to ten times higher than coating rates when methane was supplied as reactant. Characteristics of these coatings are shown in Fig. 8.23.

Coatings with unique properties were obtained by Beutler et al.[41] by using acetylene as the reactant at three different partial pressures (490, 610, and 760 torr). A 1-in.-diam coater was used with a charge of 50 g of 460-μ-diam thoria particles at a total gas flow rate of 4 liters/min (STP). The coating densities and deposition efficiencies obtained are shown in Fig. 8.24. The deposition efficiency is the percentage of the carbon supplied which forms a coating. Note that coating densities were in the range 0.5 to 1.4 g/cm^3. Densities in this range are desired for the inner, buffer layers of duplex particles. At low temperatures, low deposition efficiencies were noted with corresponding large amounts of soot. With proper equipment design, however,

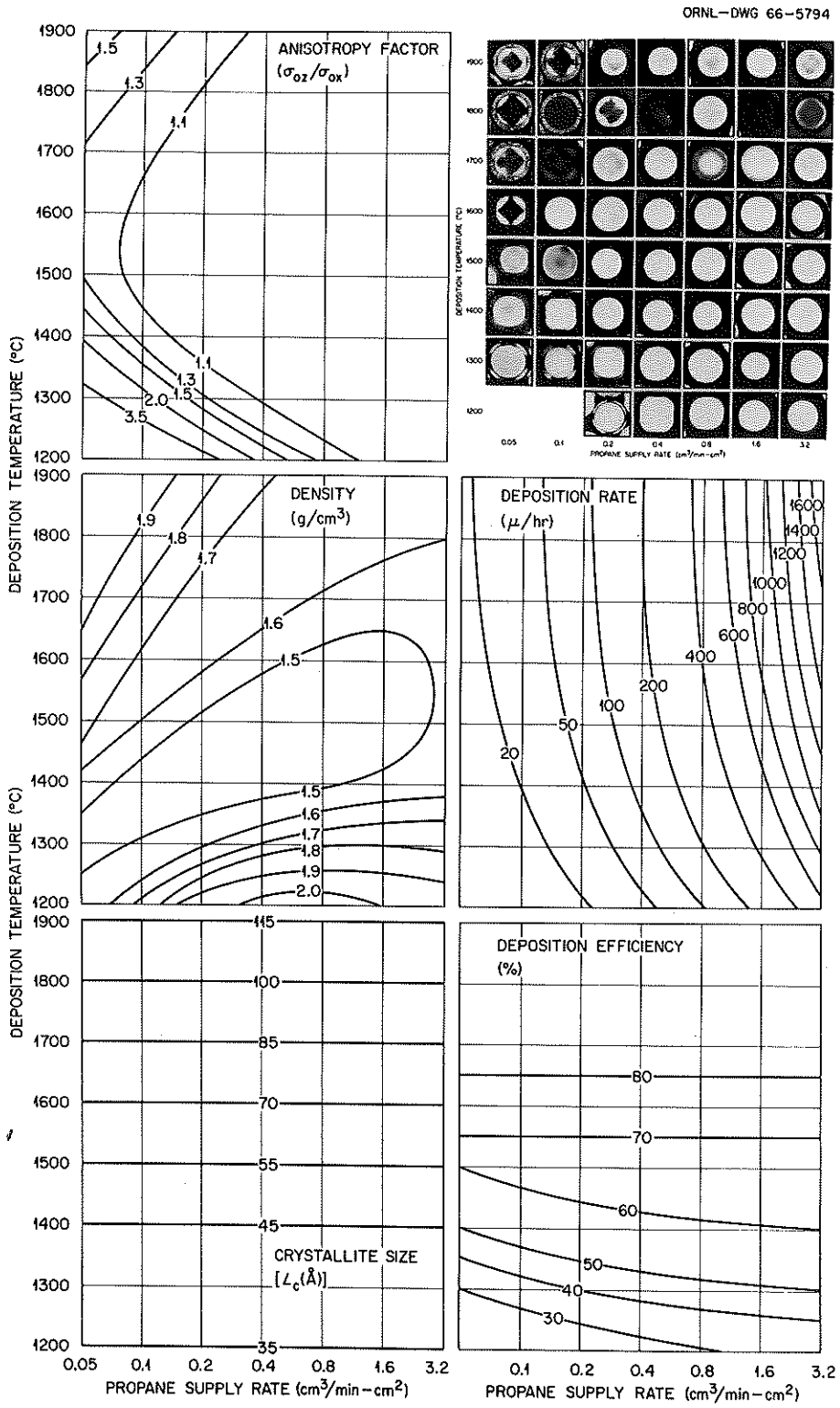

Fig. 8.23. Effect of deposition conditions and process characteristics on properties and microstructures of pyrolytic-carbon coatings deposited from propane. Reprinted from reference 56.

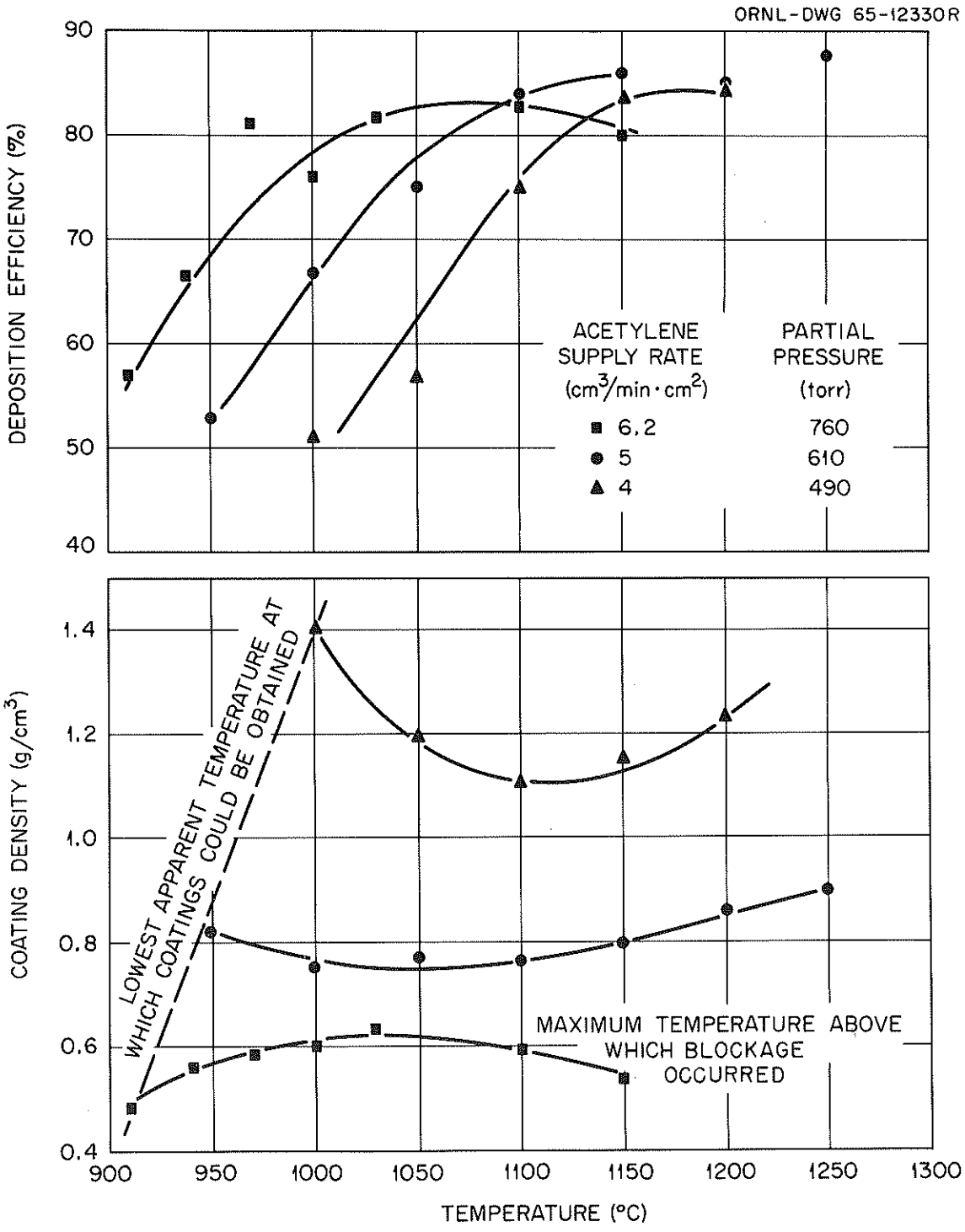

Fig. 8.24. Effects of temperature and acetylene supply rate on density and efficiency of porous coating deposition on 460-μ-diam particles. Reprinted from reference 41.

this problem can be accommodated. Typical porous coatings formed from acetylene are shown in Fig. 8.25. Note that the mounting material has penetrated the coatings to varying degrees. The mean pore diameter of these deposits, determined as porosity accessible to mercury, decreased with increased coating density as shown in Fig. 8.26.

8-3.2 Mechanical Properties

The mechanical properties of pyrolytic-carbon coatings vary with density, crystallite size, and anisotropy factors. Stress-strain curves for porous acetylene coatings, shown in Fig. 8.27, indicate that very low density coatings deform to a much higher degree than coatings with intermediate or high densities. A definite increase in crushing strength is noted with increasing coating density as indicated in Fig. 8.28.

The mechanical properties of impermeable pyrolytic carbons used for outer coatings also depend sensitively on structure, which in turn depends upon the coating conditions. Bokros and Price[58] have examined the mechanical properties of various pyrolytic carbons by three-point bending of strips cut from disks coated along with fuel microspheres. The dependence of properties on coating temperature for low and intermediate methane supply rates is shown in Figs. 8.29 and 8.30. The effect of methane supply rate at 1400°C is shown in Fig. 8.31. Properties of coatings deposited at 1730°C from 3% methane are shown in Table 8.7. A summary of properties for characteristic laminar, isotropic, and granular coatings is given in Table 8.8.

Annealing of pyrolytic carbons changed the mechanical properties as indicated in Figs. 8.32 and 8.33, and Tables 8.9 and 8.10. Results

Y-62483

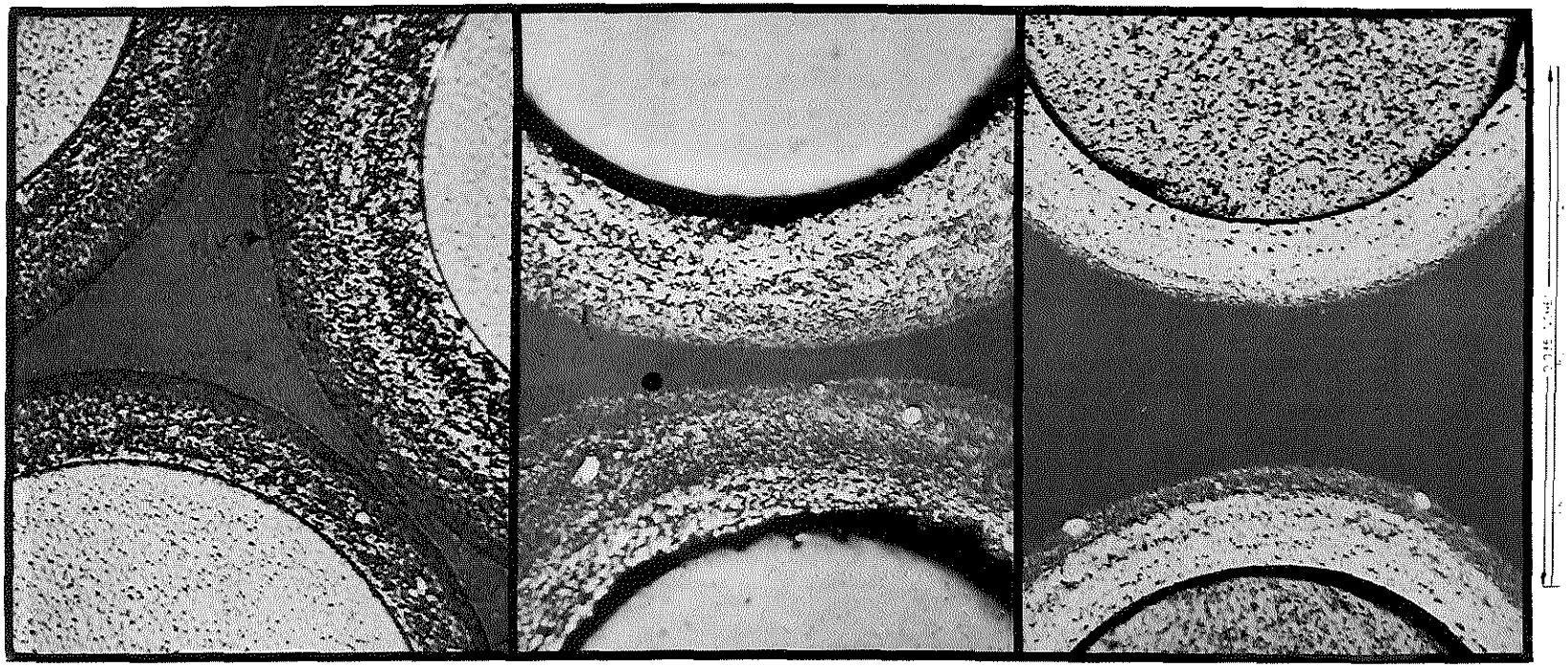

PC 98-4 Density 0.81 g/cm^3 PC 92-3 Density 1.0 g/cm^3 PC 91-3 Density 1.37 g/cm^3

Fig. 8.25. Comparison of photomicrographs of porous coatings of difference densities deposited from acetylene. Reprinted from reference 41.

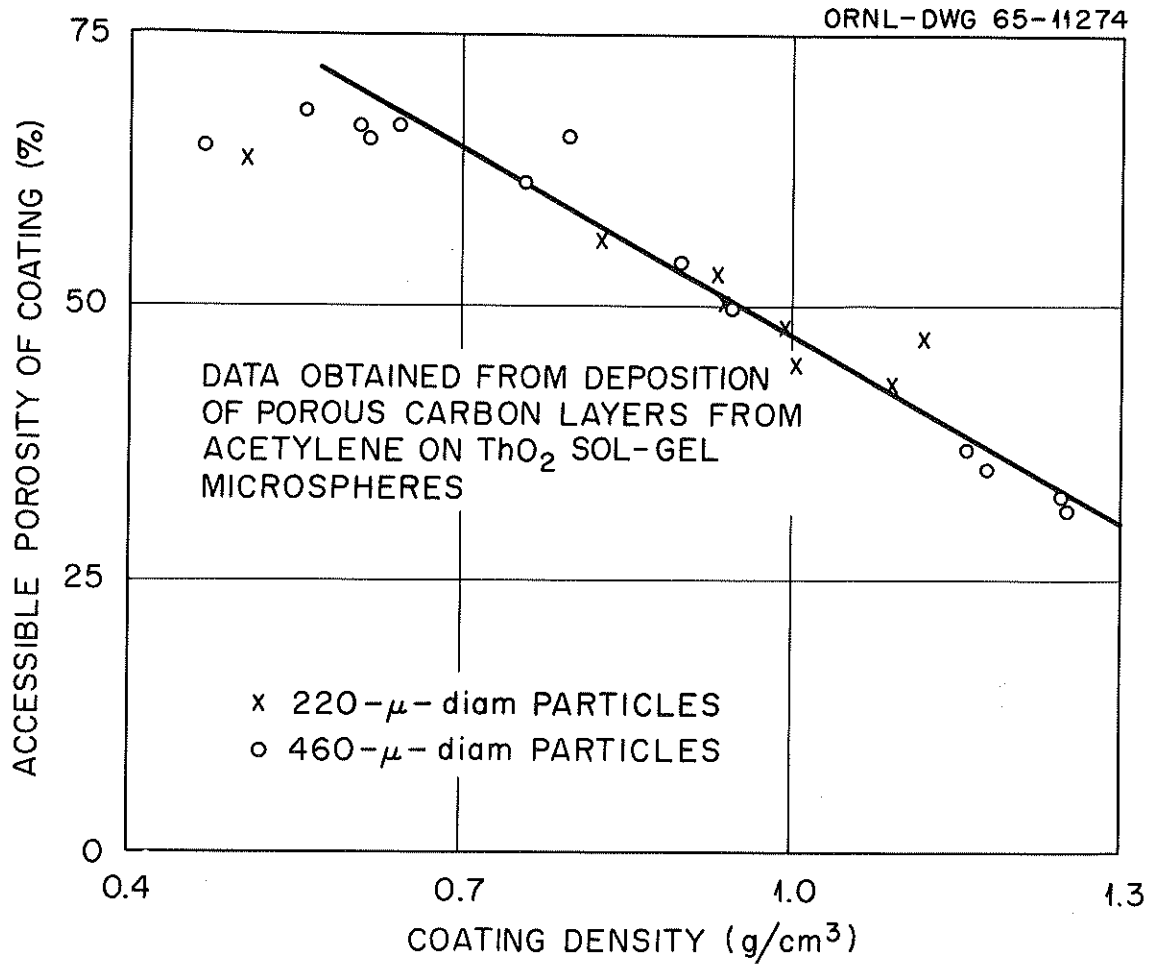

Fig. 8.26. Accessible mercury porosity versus density for low-density coatings deposited from acetylene. Reprinted from reference 41.

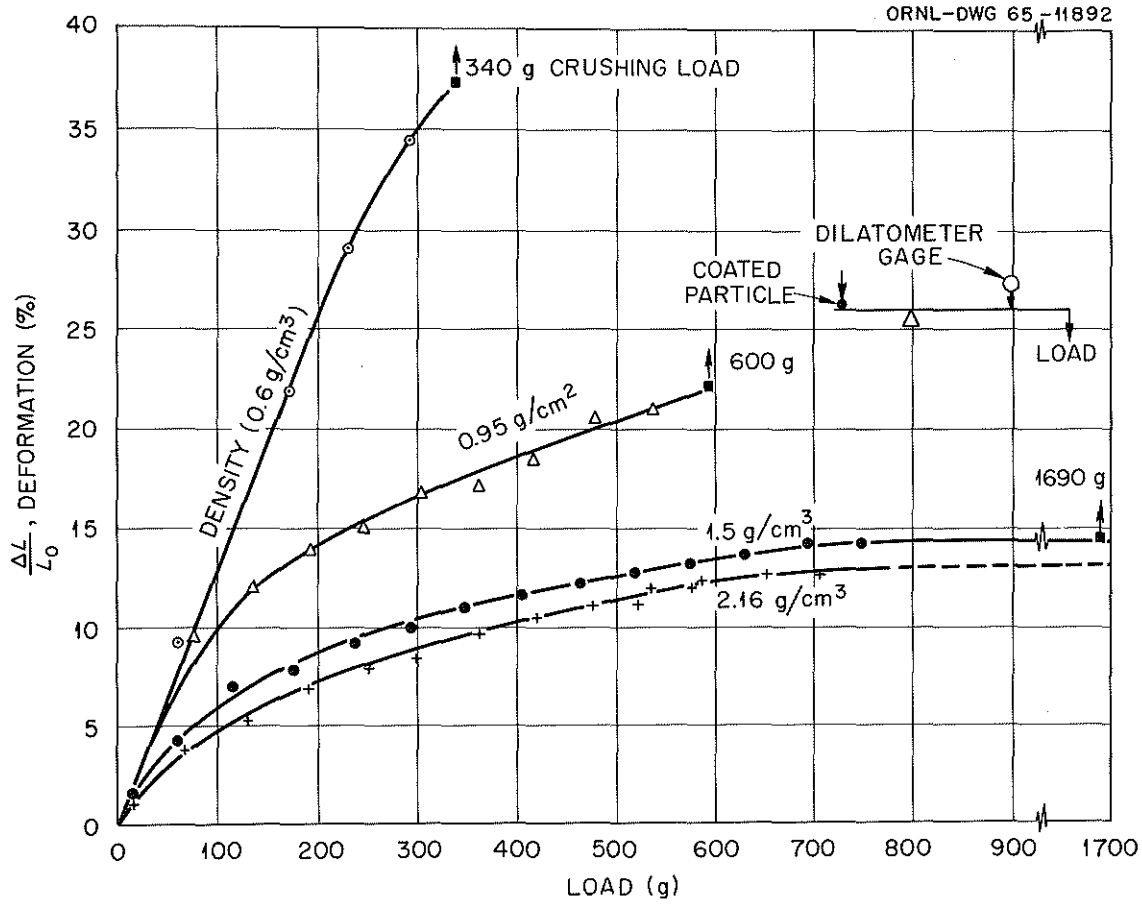

Fig. 8.27. Comparison of deformation characteristics of pyrolytic-carbon coatings of different density. Reprinted from reference 41.

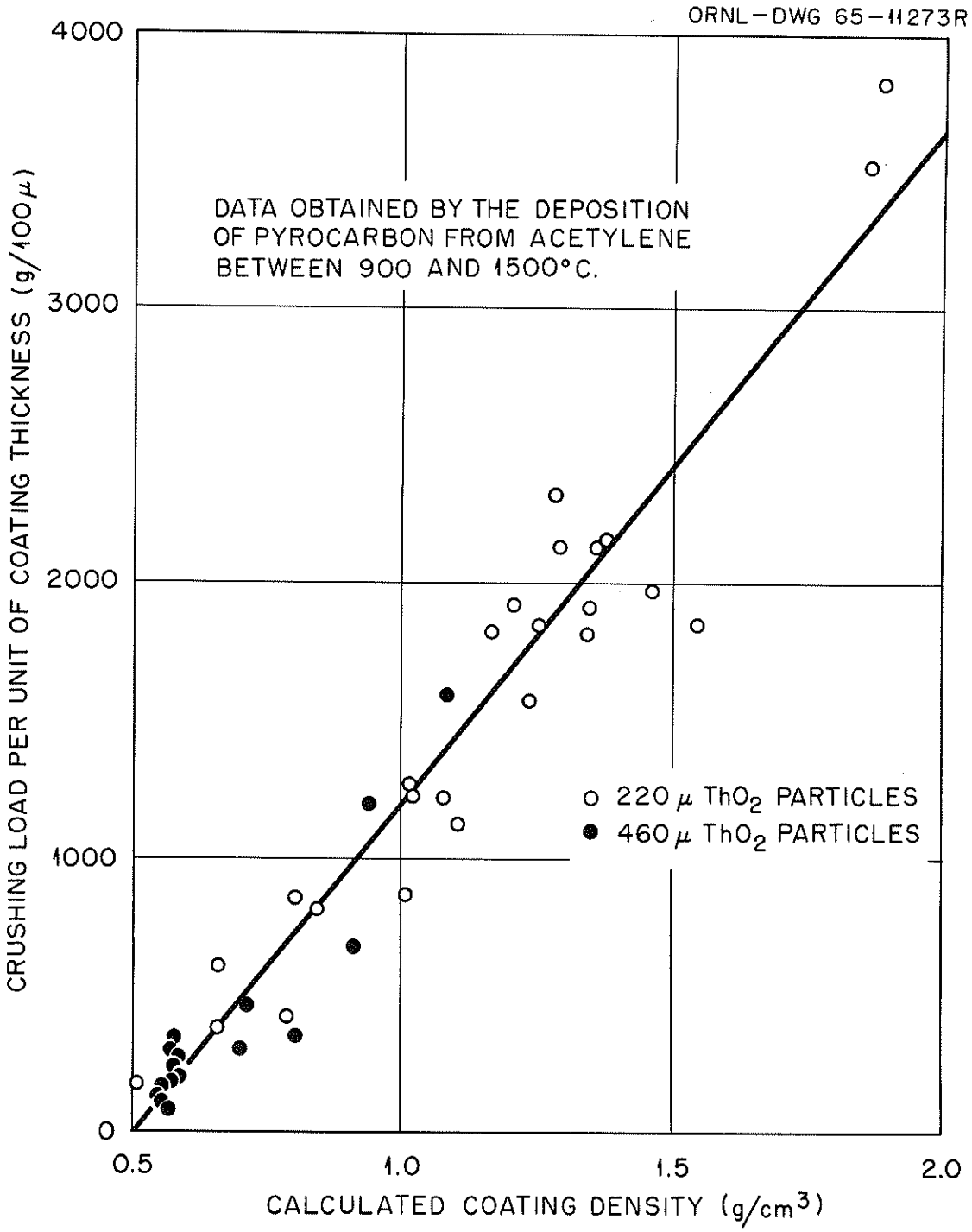

Fig. 8.28. Relationship of crushing load per unit of coating thickness to the coating density. Reprinted from reference 41.

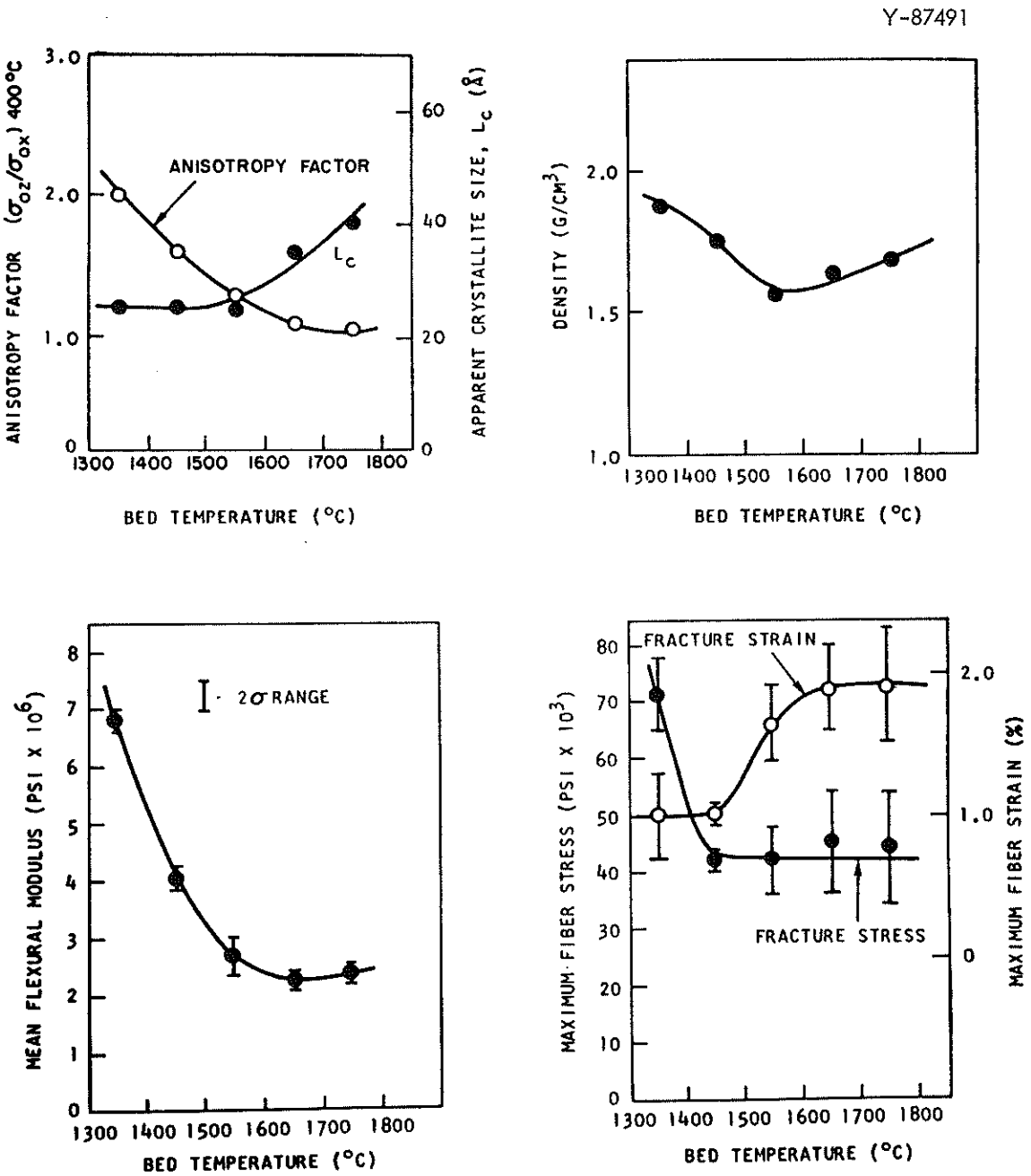

Fig. 8.29. Dependence of structural parameters and mechanical properties on deposition temperature for deposits produced in a 2.5-cm-diam coater, using 11% methane in helium and a 400 cm^2 initial charge. Reprinted from reference 58.

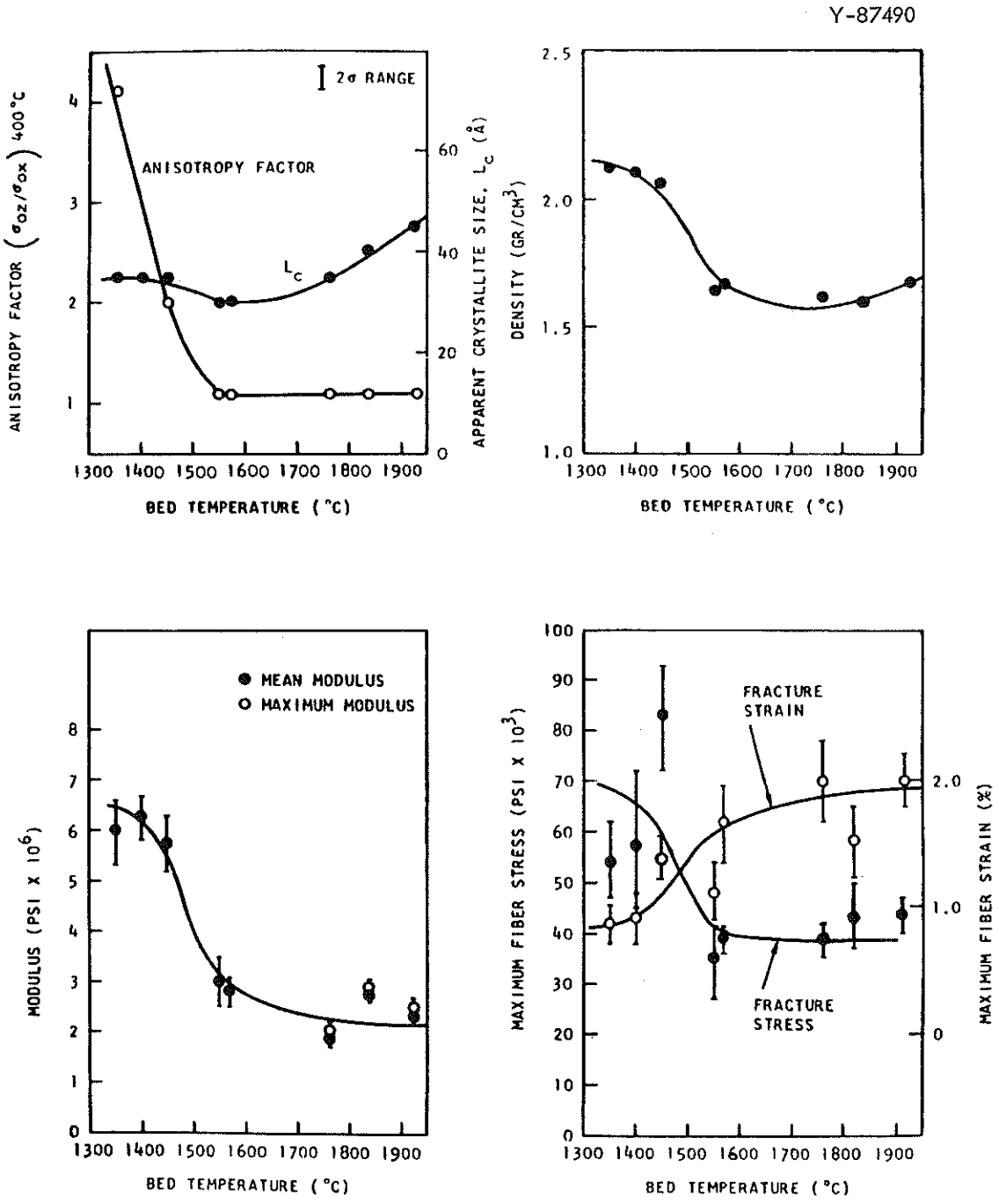

Fig. 8.30. Dependence of structural parameters and mechanical properties on deposition temperature for deposits produced in a 2.5-cm-diam coater, using 40% methane in helium and a 400 cm^2 initial charge. Reprinted from reference 58.

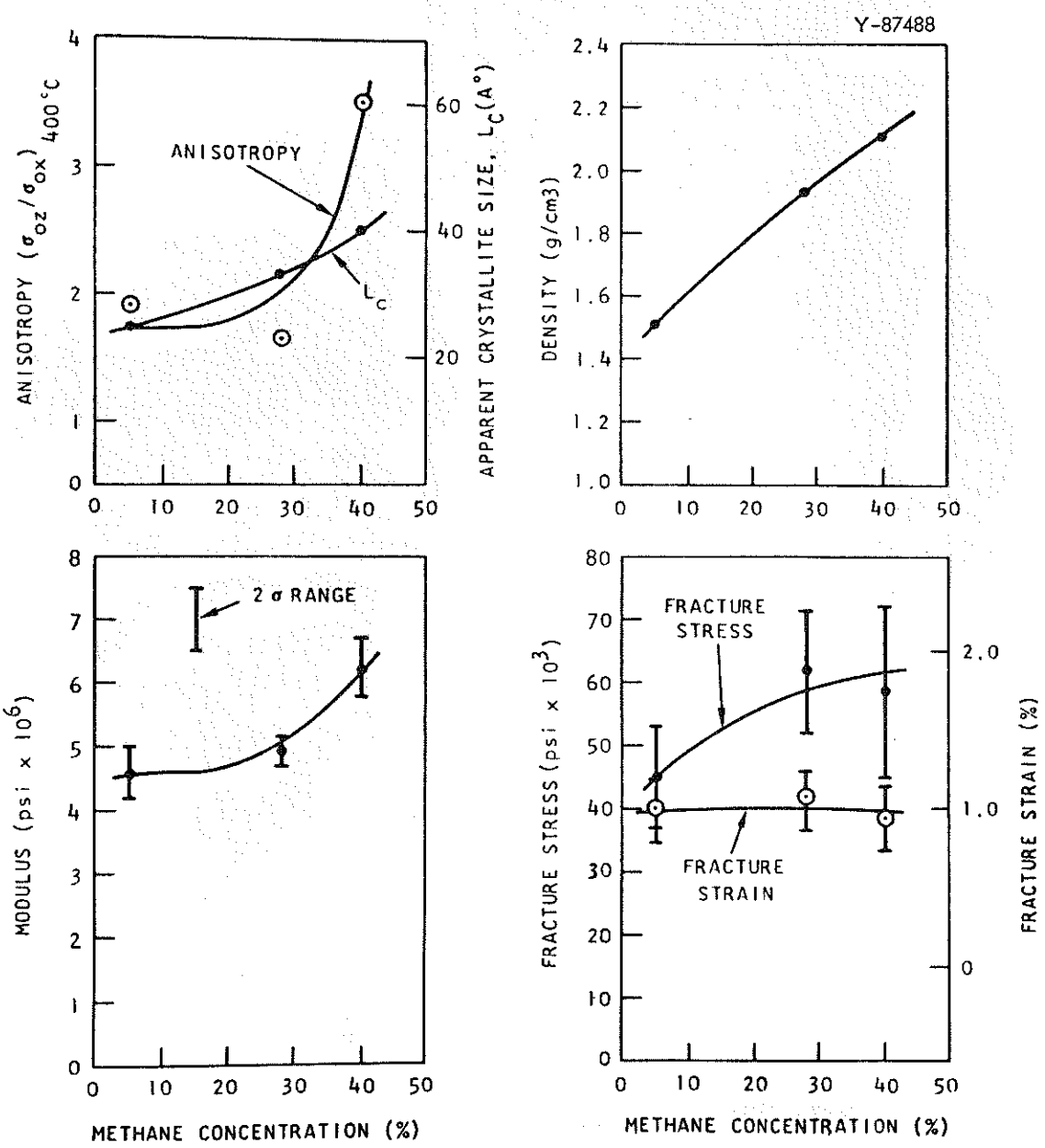

Fig. 8.31. Dependence of structural parameters and mechanical properties on methane concentration for pyrolytic carbon deposited at 1400°C (initial-charge area, 400 cm^2). Reprinted from reference 58.

Table 8.7. Structural Parameters and Mechanical Properties of Granular Pyrolytic-Carbon Structure Deposited at 1730°C from 3% Methane[a]

Density	2.00–2.02 g/cm^3
Bacon Anisotropy Factor	1.1
Apparent crystallite size, L_c	140 A
Layer spacing	3.43 A
Mean modulus[b]	$1.21 \pm 0.11 \times 10^6$ psi[c]
Maximum modulus[b]	$1.62 \pm 0.17 \times 10^6$ psi[c]
Fracture stress[b]	$17.8 \pm 1.7 \times 10^3$ psi[c]
Fracture strain[b]	1.48 ± 0.17%[c]

[a]Deposited in a 2.5-cm-diam coater using a 10-g charge of 420–495 μ $(U,Th)C_2$ particles (130 cm^2). The total flow rate was 3300 cm^3/min and the average deposition rate was 15 μ/hr.

[b]Average from ten specimens.

[c]The ± values are standard deviations of the determinations.

Table 8.8. Summary of As-Deposited Mechanical Properties of Laminar, Isotropic, and Granular Pyrolytic-Carbon Deposits Investigated

Structure	Mean Modulus (psi × 10^6)	Fracture Stress (psi × 10^3)	Fracture Strain (%)
Laminar	4.5–7	45–90	0.7–1.7
Isotropic	1.8–2.7	30–55	1.2–2.5
Granular	1.1–1.3	15–20	1.3–1.6

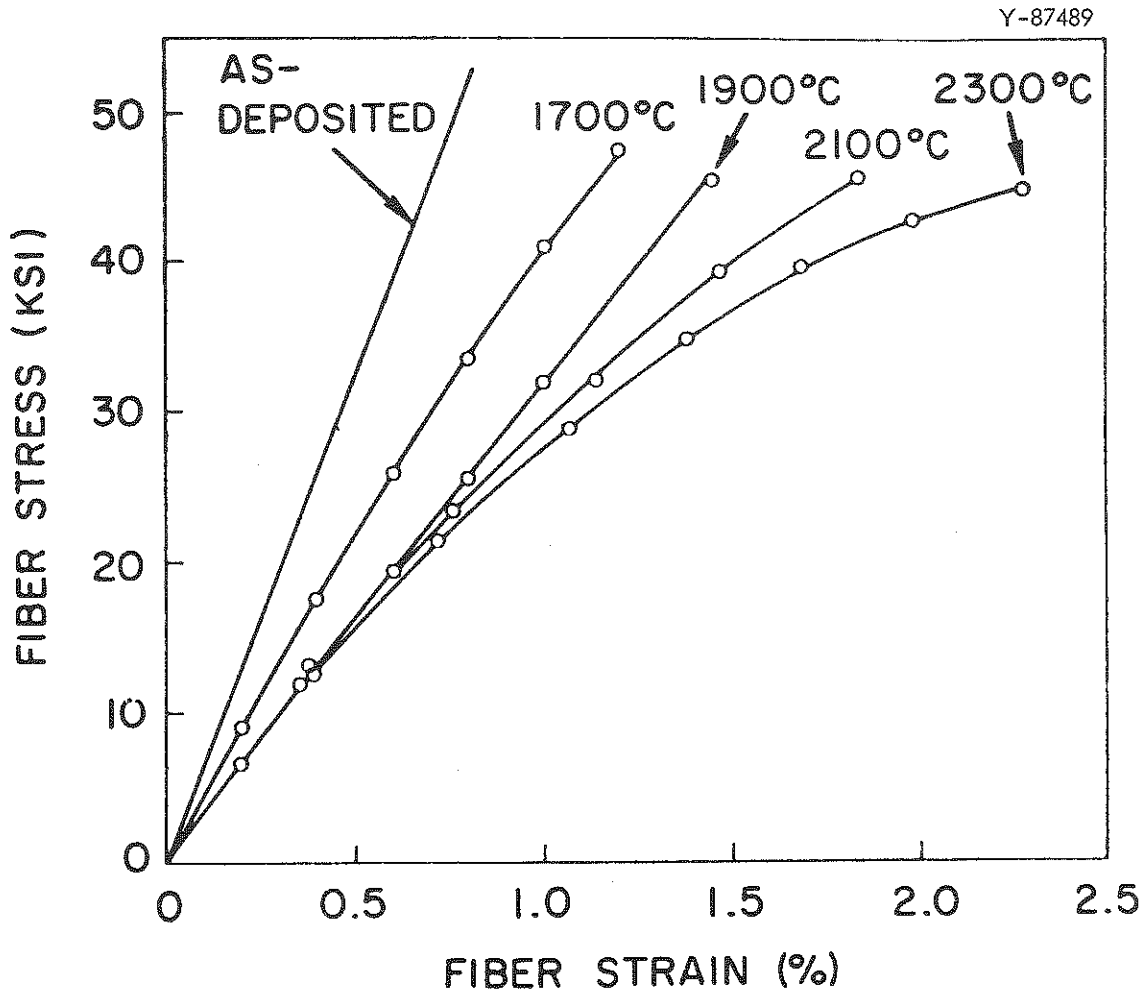

Fig. 8.32. Effect of annealing for 4 hr at various temperatures on stress-strain relationship for pyrolytic carbon deposited at 1450°C from 40% methane; charge area was 400 cm^2. Reprinted from reference 58.

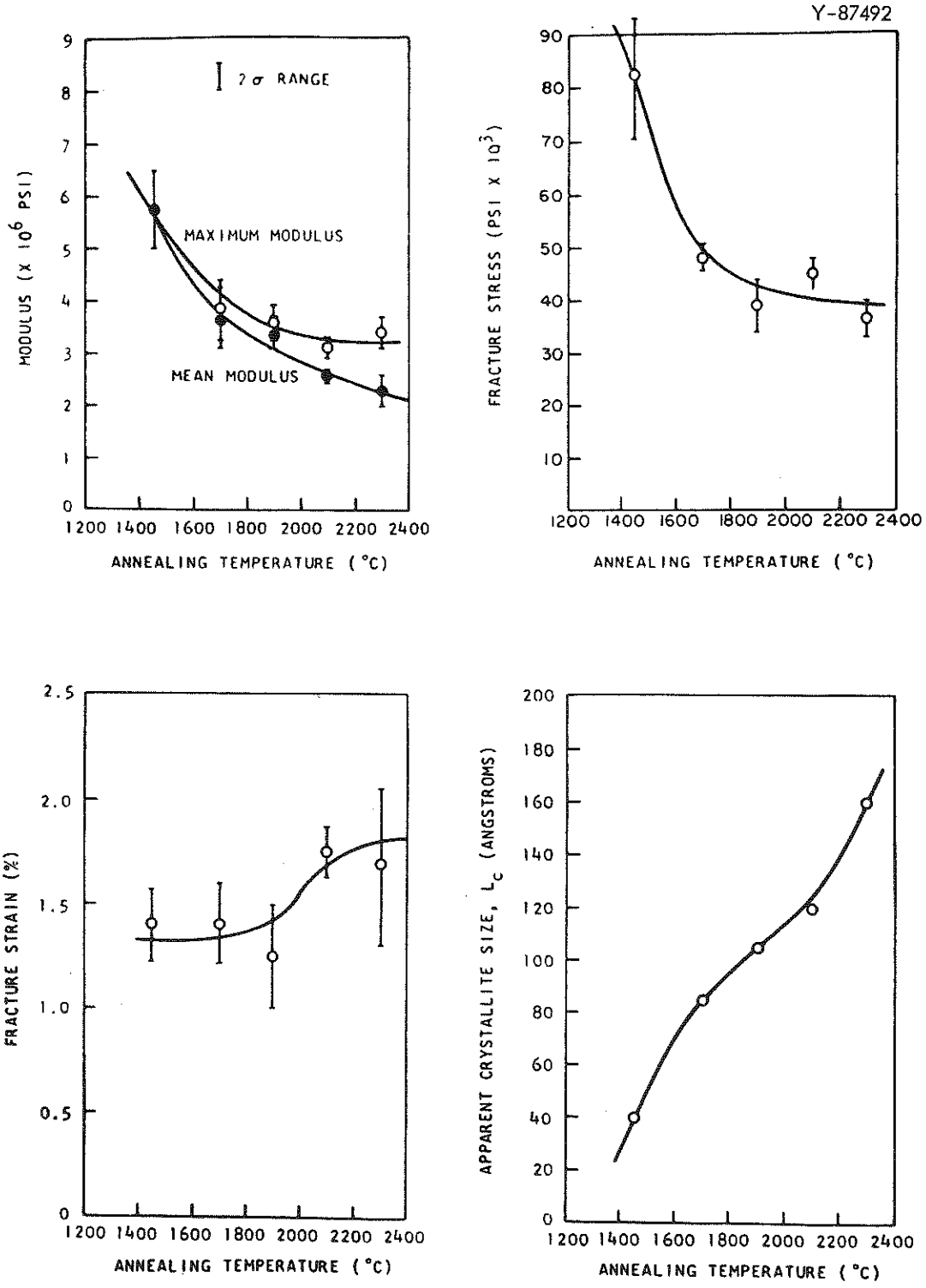

Fig. 8.33. Dependence of mechanical properties and L_c on annealing temperature for a 1450°C laminar structure deposited from 40% methane (400 cm^2 charge); annealing time was 4 hr in each case. Reprinted from reference 58.

Table 8.9. Effect of Annealing 4 hr at 2300°C on Mechanical Properties and Structure of Three Isotropic Pyrolytic-Carbon Structures[a]

Specimen Number	Coating Conditions			Mechanical Properties[b]					
				As Deposited			After Annealing		
	Bed Temperature (°C)	Methane Concentration (%)	Coating Rate (μ/hr)	Mean Modulus (psi×10⁶)	Fracture Stress (psi×10³)	Fracture Strain (%)	Mean Modulus (psi×10⁶)	Fracture Stress (psi×10³)	Fracture Strain (%)
2359-57	1650	11	29	2.4 ± 0.1	44 ± 6	1.9 ± 0.3	2.8 ± 0.1	44 ± 2	1.6 ± 0.1
2511-17	1760	40	67	1.9 ± 0.1	39 ± 3	2.0 ± 0.4	2.5 ± 0.1	37 ± 1	1.5 ± 0.1
2511-23	1925	40	56	2.2 ± 0.1	44 ± 3	2.0 ± 0.2	2.0 ± 0.1	40 ± 3	2.0 ± 0.2

Specimen Number	Coating Conditions			Structural Parameters					
				As Deposited			Annealed		
	Bed Temperature (°C)	Methane Concentration (%)	Coating Rate (μ/hr)	L_c (Å)	Bacon Anisotropy Factor	Density	L_c (Å)	Bacon Anisotropy Factor	Density
2359-57	1650	11	29	50	1.1	1.62	70	1.1	1.65
2511-17	1760	40	67	45	1.1	1.61	80	1.1	1.70
2511-23	1925	40	56	70	1.05	1.67	80	1.05	1.65

[a]Carbon was deposited in a 2.5-cm-diam coater; the initial charge area was 400 cm^2 and the total flow was 2600 cm^3/min.

[b]The ± figures are the standard deviations of the determinations.

Table 8.10. Effect of Annealing for 4 hr at 2800°C on Structure and Mechanical Properties of Pyrolytic Carbon Deposited at 2000°C from 14.7% Methane[a]

Property	As Deposited	Annealed	Change (%)
Density, g/cm^3	1.99–2.01	1.99–2.01	0
Bacon Anisotropy Factor	1.4	1.4	0
L_c, A	145	130	−10
Layer spacing, A	3.43	3.41	−0.6
Mean modulus, psi × 10^6[b]	1.54 ± 0.06[c]	1.59 ± 0.07[c]	+3
Maximum modulus, psi × 10^6[b]	1.81 ± 0.13[c]	1.72 ± 0.16[c]	−5
Fracture stress, psi × 10^3[b]	37.5 ± 2.7[c]	27.8 ± 4.7[c]	−39
Fracture strain, %[b]	2.44 ± 0.21[c]	1.76 ± 0.39[c]	−28

[a]Deposited in a 6.3-cm-diam coater using a 186-g charge of 350 to 420 μ $(U,Th)C_2$ particles (2600 cm^2). The total flow rate was 13,500 cm^3/min and the average deposition rate was 25 μ/hr.

[b]Average from 10 specimens.

[c]The ± values are standard deviations of the determinations.

indicate that the properties of high-density laminar coatings deposited from high methane concentrations are strongly affected by annealing. Their moduli can be decreased by a factor of 2 to 3, and their fracture strains can be doubled by annealing in the range 1700 to 2700°C. The mechanical properties of low-density laminar coatings and isotropic coatings are either not affected or only slightly affected by annealing. The effects of irradiation on mechanical properties are discussed later.

8-3.3 Thermophysical Properties

Like the mechanical properties, the thermophysical properties of pyrolytic-carbon coatings vary widely according to deposition conditions. This is, of course, what one would expect for a material of such anisotropic character. In general, coated-particle fuels are designed around mechanical properties and irradiation effects rather than thermophysical properties of the coatings. Thus, these properties may be considered of secondary importance but will be briefly discussed here for completeness.

Coefficient of Thermal Expansion

The thermal expansion characteristics of highly oriented pyrolytic carbon are similar to those of single crystals of graphite, which show at 400°C a coefficient of thermal expansion (CTE) parallel to the basal plane, α_a, of zero and a coefficient perpendicular to the basal planes, α_c, of 28×10^{-6} $°C^{-1}$ (ref. 59). The net thermal expansion for polycrystalline pyrolytic carbons is obtained by integrating the contributions of individual crystallites, with allowance made for the "accommodation" of a portion of the c-axis expansion. The data are best

presented in terms of preferred orientation parameters, R_{oz} and R_{ox}, referred to the normal to the deposition plane OZ, and the direction parallel to the deposition plane OX, respectively. These parameters are determined by x-ray techniques.

Price and Bokros[60] have shown that:

$$R_{oz} = \frac{\int_0^{\pi/2} I(\Phi) \sin^3 \Phi \, d\Phi}{\int_0^{\pi/2} I(\Phi) \sin \Phi \, d\Phi} \tag{5}$$

and

$$R_{ox} = 1 - \frac{R_{oz}}{2} \tag{6}$$

The Bacon Anisotropy Factor (BAF) is also related to R_{oz}:

$$BAF = 2\left(\frac{1 - R_{oz}}{R_{oz}}\right) . \tag{7}$$

The thermal expansion coefficients of various pyrolytic carbons with differing preferred orientations are shown in Fig. 8.34 relative to the preferred orientation parameter, R, defined by

$$R = R_{oz} \qquad \text{for } 0 \leq R \leq 0.66 \tag{8}$$

$$R = R_{ox} \qquad \text{for } 0.66 \leq R \leq 1 . \tag{9}$$

The dashed line is the curve predicted assuming no accommodation of the c-axis expansion. On this basis a randomly oriented pyrolytic carbon (R = 0.66) should have a CTE of 9.2×10^{-6} at 400°C. Measured values are lower and are in the range 4 to 6.5×10^{-6} $°C^{-1}$ with values for low-density carbons falling below those of higher density carbons. The accommodation of c-axis expansion is attributed to the effects of

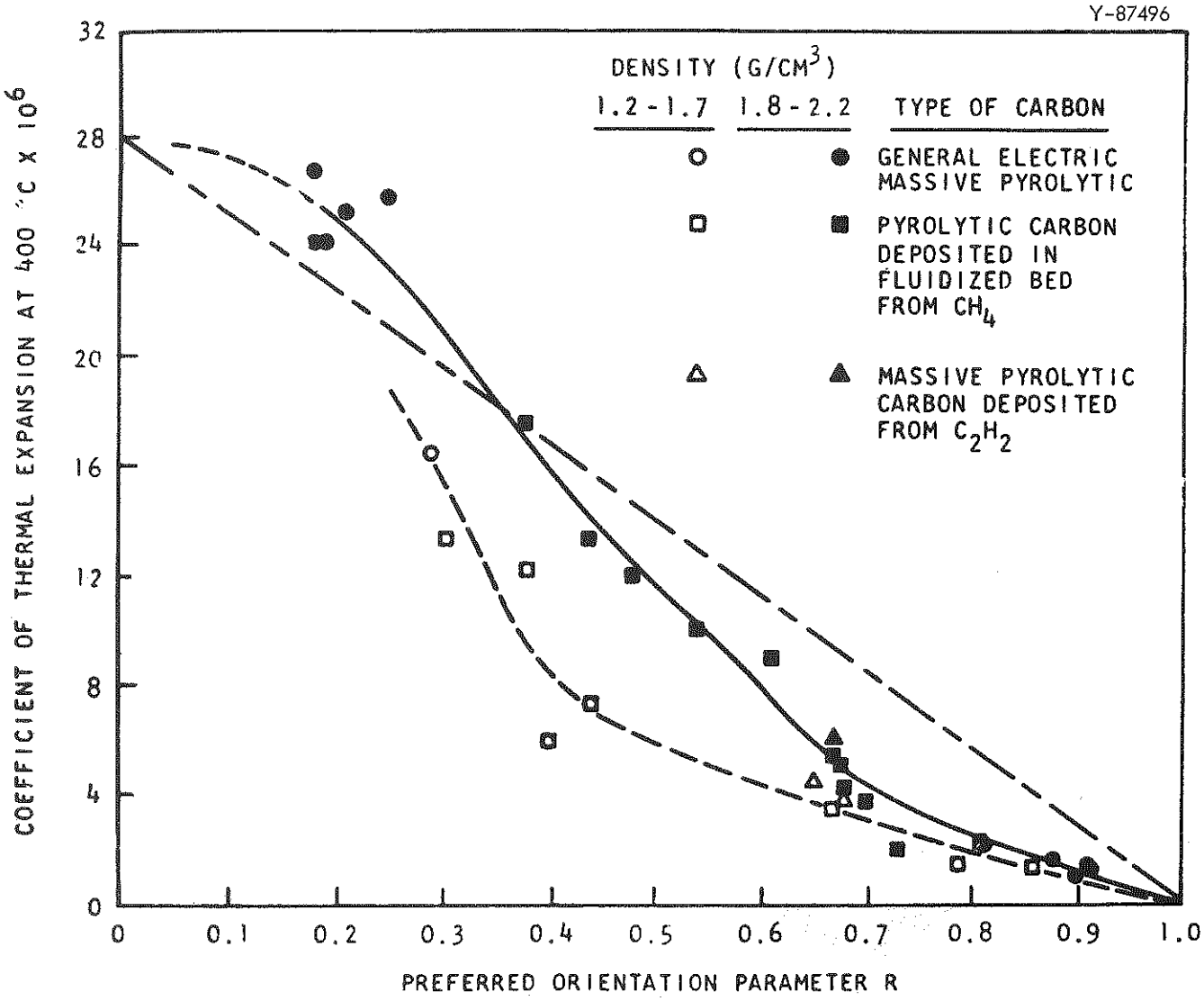

Fig. 8.34. Thermal expansion coefficient at 400°C versus preferred orientation parameter R for various pyrolytic carbons. Reprinted from reference 59.

porosity. For pyrocarbons with preferred orientation, the a-axis expansion increases and the c-axis expansion decreases with increased preferred orientation.

Thermal Conductivity

The thermal conductivity of massive, pyrolytically deposited carbon is discussed in Chapter 37 of this handbook. These massive pyrocarbons are generally very highly oriented relative to pyrocarbons deposited on microspheres and therefore show a strong anisotropy of conductivity. However, since no measurements on pyrolytic carbons deposited in a fluidized bed have been reported, data for the massive pyrocarbons must be suitably adjusted. The consequences of this are discussed in Section 6, Design of Coated Particle Fuels.

8-3.4 Reaction of Pyrolytic-Carbon-Coated Fuel Particles with Water Vapor

Oxidation of the pyrocarbon coatings on fuel particles can cause failure of coatings and a subsequent release of some portion of fission products into the coolant. Oxygen would react very rapidly with the pyrocarbon coatings at normal operating temperatures. An ingress of steam from a steam generator is the most likely source of an oxidizing gas in the coolant. The conditions under which water vapor might cause failure of the pyrocarbon coatings are therefore of interest in the operation of high-temperature gas-cooled reactors.

The reaction of pyrocarbon coatings with water vapor has been studied by a number of investigators[61–64] using various experimental conditions. These have included such parameters as coating structure,

temperature, partial pressure of water vapor, irradiation, and support and containment of the particles.

The rates of reaction of water vapor with various pyrocarbon coatings having laminar, granular, or isotropic structures have been found to be quite variable.[63,64] Attempts to correlate reaction rates with coating density, anisotropy, and crystallite size were unsuccessful. Reaction rates obtained for a number of isotropic pyrocarbon coatings at various temperatures are given in Fig. 8.35. Apparent activation energies vary considerably (30 to 65 kcal/mole), but the larger values agree with 63 kcal/mole reported for higher partial pressures of water vapor.[62]

Apparent orders of reaction of the water vapor-pyrocarbon reaction with respect to partial pressure of water vapor have been found[62–64] to vary from 0.5 to 1. Burnette et al.[62] report 0.7 for partial pressures between 19 and 165 torr in the temperature range of 1000 to 1400°C. Values ranging from 0.5 to 1 were found in this temperature range at partial pressures of 0.18 to 0.75 torr (ref. 64) and at 1000°C using partial pressures of 5 to 550 torr (ref. 63).

Certain fission products, notably barium and strontium, might be expected to catalyze the pyrocarbon-water vapor reaction. Studies of coated particles that were irradiated to build up an inventory of fission products before exposure to water vapor showed some catalytic effect on the reaction rate and also showed that failure times were reduced.[62]

The exposure time and related burnoff of pyrocarbon before failure of the coatings are of interest in assessing the results of inleakage

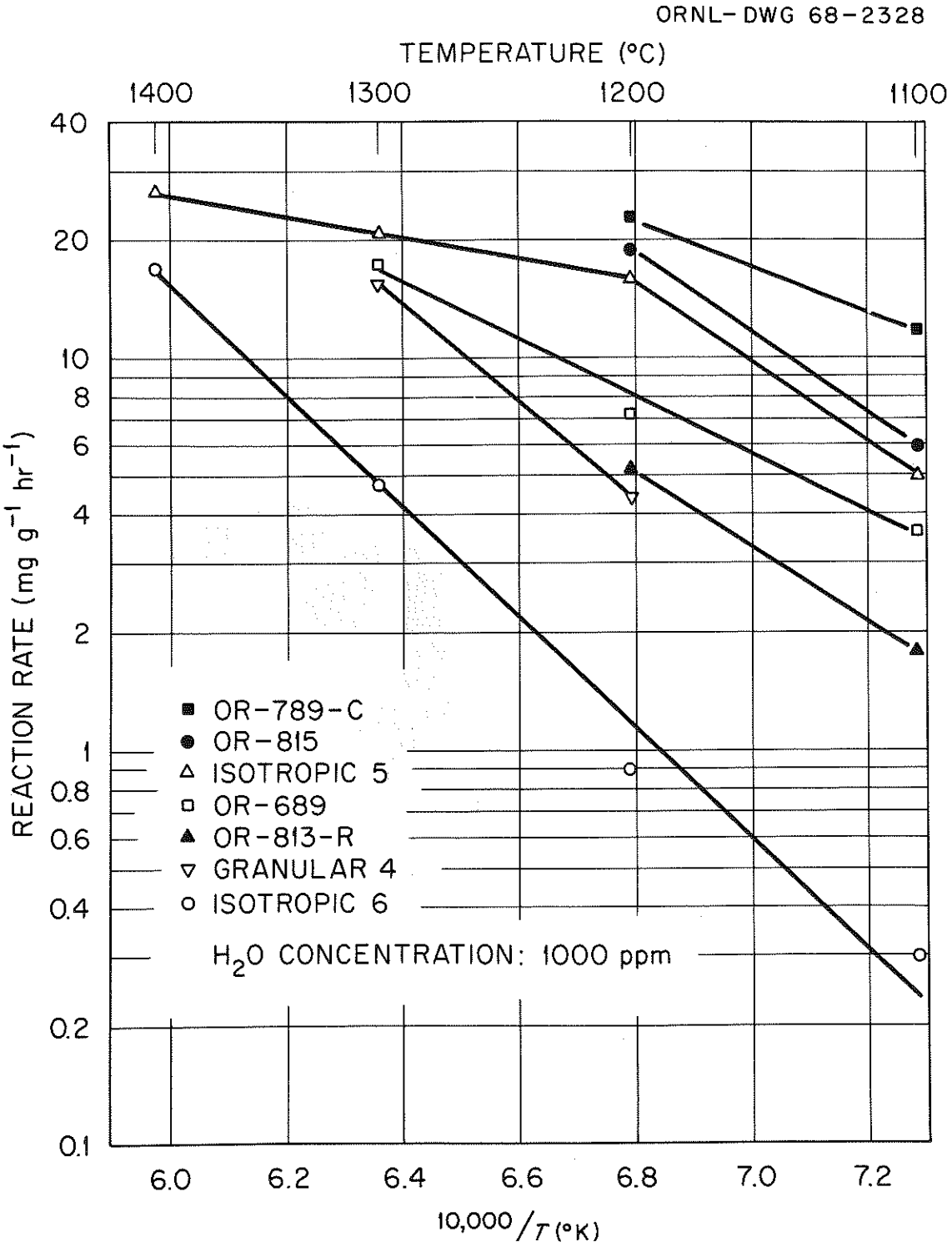

Fig. 8.35. Effects of temperature on reaction rates of various isotropic batches of coated particles. (Structure details given in references 65 and 66.) Data from reference 64.

of water vapor. Studies[62–64] made of these effects have shown that exposure times required to attain failures decreased with both increasing temperature and partial pressure of water vapor. The quantity of pyrocarbon oxidized at the time of failure, however, varied markedly for different batches of coated particles, suggesting that different types of attack were involved. In general, a pitting type of attack was observed similar to that shown in Fig. 8.36.

Most of the data available were obtained for loose particles directly exposed to the gas stream containing water vapor. Studies also have been made in which the coated particles were contained in a closed graphite container[62] or in a graphite tube in which the gas stream contacted a graphite surface before reaching the coated particle.[63] Both systems reduced the rate of attack of the coatings, the graphite container being most effective at temperatures above 1200°C. A very high degree of protection against attack by water vapor was attained by supporting coated fuel particles in a graphite matrix.[67] The geometry and composition of the fuel element can also be very important factors in the attack of pyrocarbon coatings during inleakage of water vapor.

8-4 PROPERTIES OF OXIDE COATINGS

The properties of oxide coatings have been summarized by Oxley.[5] Alumina coatings deposited at temperatures between 500 to 700°C are porous, of low density, and amorphous. They become crystalline when heated to 1000°C and above. Coatings deposited at 1000°C are impermeable and are near theoretical density, with crystallites ranging up to 0.3 μ in size dispersed in an amorphous matrix. Alumina coatings

Y-76383

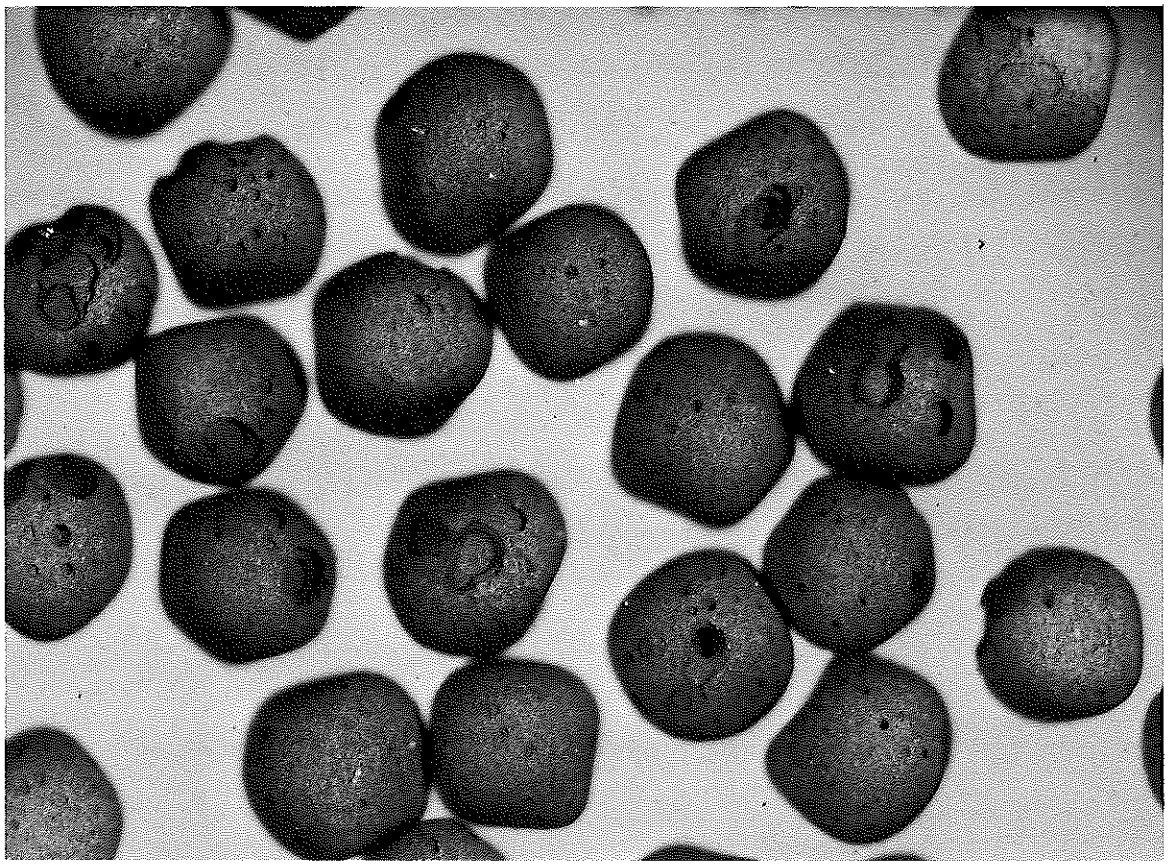

Fig. 8.36. Isotropic-6 coated particles after 24 hr exposure at 1300°C to 1000 ppm of H_2O in helium. 33×. Submitted by Oak Ridge National Laboratory, July 1968.

deposited at 1400°C are highly crystalline and have a crystallite size of about 25 μ but have inferior integrity to 1000°C coatings. Coatings prepared at 1000°C or above are equal to or harder than sapphire (2200 to 2500 KHN, 50-g load).

Beryllia coatings must be deposited at higher temperatures than alumina coatings to obtain equivalent properties.[5] Coatings deposited between 800 to 1100°C are porous and not obviously crystalline. At deposition temperatures of 1400°C or higher, BeO coatings are impermeable and are near theoretical density. These coatings have good crystallinity. The 1400°C coating is about as hard as single-crystal BeO (1200 to 1400 KHN, 50-g load).

8-5 IRRADIATION EFFECTS AND PERFORMANCE OF PYROLYTIC-CARBON COATINGS

8-5.1 Effects of Irradiation on Mechanical Properties of Pyrolytic Carbons

Price and Bokros[68] have determined the effects of fast-neutron exposures of 1.5 to 2.4 × 10^{21} neutrons/cm^2 (E > 0.18 Mev) at 540 to 1060°C on the mechanical properties of pyrolytic carbons with laminar, isotropic, and granular microstructures. The deposition conditions used to prepare the carbons are given in Table 8.11, and the structural data are given in Table 8.12. Results are shown in Figs. 8.37 through 8.39. These results show that irradiation increased the elastic moduli by 30 to 100%, with isotropic and granular carbons with low initial moduli showing the greatest increases. The flexural strength of laminar carbons was unchanged, whereas that of the isotropic and granular carbons

Table 8.11. Deposition Conditions Used to Prepare Carbon Deposits

Structure	Bed Temperature (°C)	Methane Concentration in Helium (%)	Charge Weight (g)	Particle Diameter (μ)	Bed Surface Area (cm^2)	Total Flow Rate at 23°C and 1 atm (cfm)	Coater Diameter (cm)	Contact Time[a] (sec)	Average Deposition Rate[b] (μ/hr)
Laminar 1	1400	40	15	150–250	400	2,750	2.5	0.19	24
Laminar 2	1400	28	15	150–250	400	2,780	2.5	0.19	20
Laminar 3	1400	5	15	150–250	400	2,400	2.5	0.21	9.1
Granular 4	1730	3	10	420–495	130	3,300	2.5	0.13	15
Isotropic 5	1650	15	34	420–495	400	4,600	2.5	0.10	89
Isotropic 6	2000	14.7	186	350–420	2600	13,500	6.3	0.14	25
Isotropic 7	1800	14.7	186	350–420	2600	13,500	6.3	0.15	22

[a]Calculated by dividing the total gas flow rate at the deposition temperature into the estimated volume of the hot zone and ignoring the volume change that occurs due to pyrolysis.

[b]Calculated by dividing the total thickness by the coating time.

Table 8.12. Structural Data for Carbons

Structure	Density (g/cm^3)	Bacon Anisotropy Factor	Crystallite Size, L_c (A)[c]	Misaligned Layers (%)	Layer Spacing (A)
Laminar 1	2.115 ± 0.003	3.36	43	2	3.43
Laminar 1A[a]	2.159 ± 0.003	2.59	113	1	3.42
Laminar 1G[b]	2.191 ± 0.003	2.59	226	1	3.35
Laminar 2_1[c]	1.951 ± 0.006	1.64	33	10	3.45
Laminar 2_2[c]	1.916 ± 0.001	1.66	33	10	3.45
Laminar 2A[a]	1.939 ± 0.003	1.66	73	5	3.42
Laminar 2G[b]	2.081 ± 0.006	1.64	132		3.37
Laminar 3	1.512 ± 0.006	2.09	25	23	3.43
Laminar 3A[a]	1.573 ± 0.012	1.88	43	18	3.42
Granular 4	2.008 ± 0.006	1.06	139	2	3.42
Isotropic 5	1.548 ± 0.008	1.00	49	10	3.43
Isotropic 6	2.000 ± 0.005	1.30	145	1	3.42
Isotropic 7	1.816 ± 0.001	1.05	105		3.43

[a]Annealed 4 hr at 1900°C in vacuum.

[b]Annealed 2 hr at 2800°C in argon.

[c]Laminar 2_1 and 2_2 were duplicate runs under nominally identical conditions.

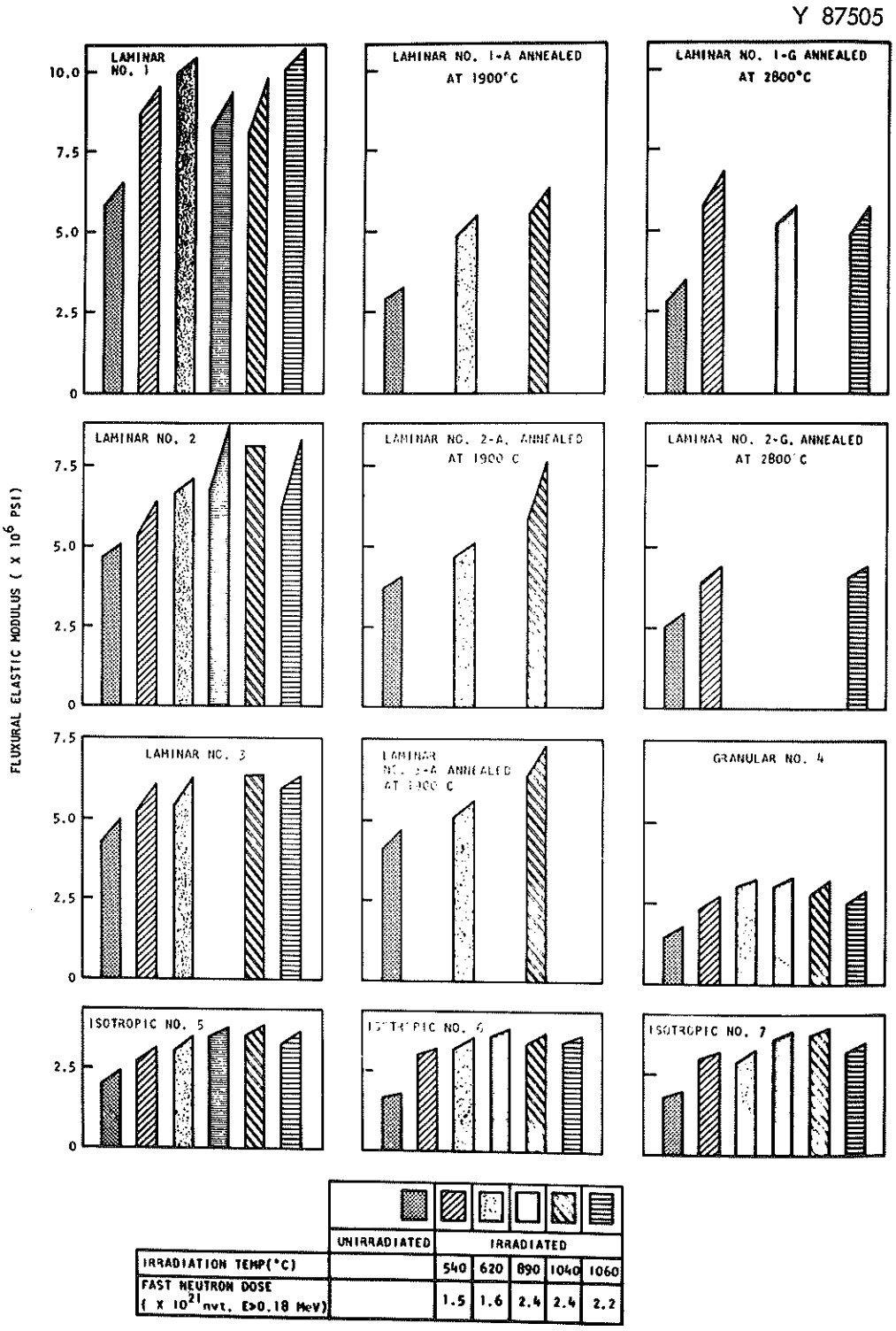

Fig. 8.37. Maximum flexural elastic modulus of pyrolytic-carbon samples before and after irradiation; tapered portions of bar graphs extend one standard deviation on either side of the mean height (for structural designations, Table 8.12). Reprinted from reference 68.

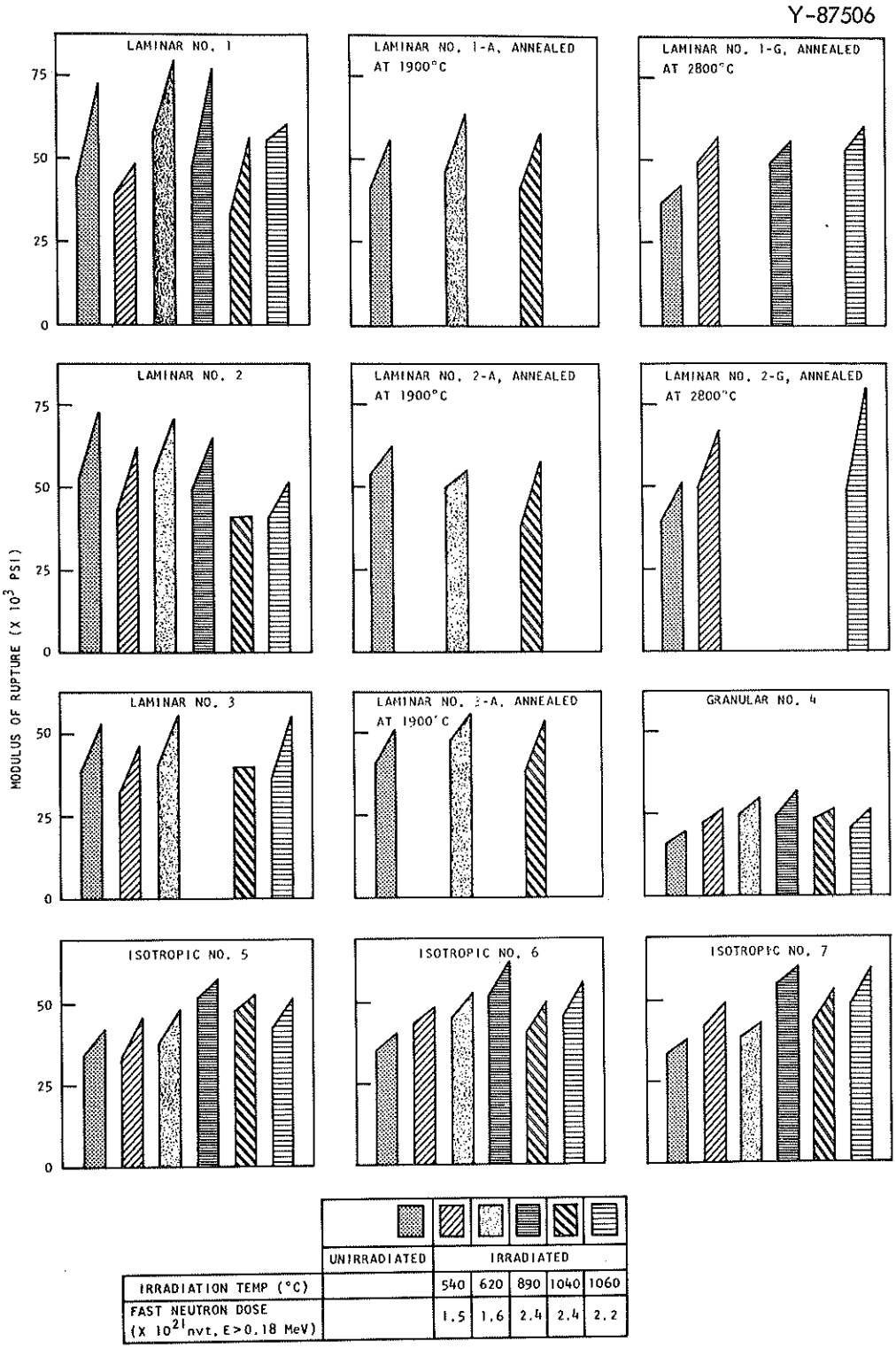

Fig. 8.38. Modulus of rupture (flexural strength) of pyrolytic-carbon samples before and after irradiation; tapered portions of bar graphs extend one standard deviation on either side of the mean height (for structural designations, Table 8.12). Reprinted from reference 68.

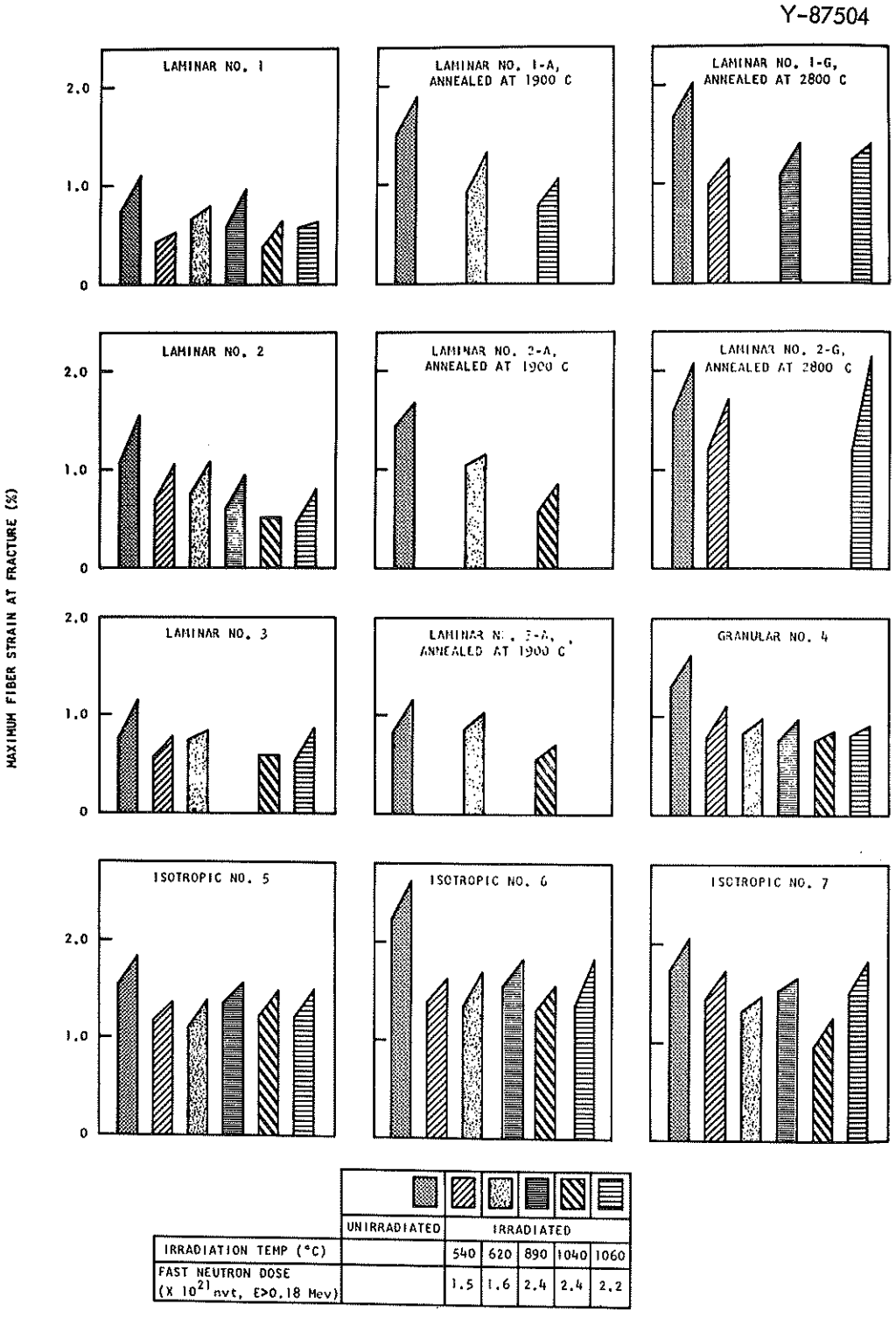

Fig. 8.39. Maximum fiber strain at fracture of pyrolytic-carbon samples before and after irradiation; tapered portions of bar graphs extend one standard deviation on either side of the mean height (for structural designations, Table 8.12). Reprinted from reference 68.

increased up to 60%. Because the increase in strength was not as great as the increase in elastic modulus, there was a decrease in elastic strain-to-fracture for all carbons.

8-5.2 Irradiation-Induced Dimensional Changes in Pyrolytic-Carbon Coatings

Fast-neutron irradiation of pyrolytic-carbon coatings results in three types of dimensional changes which contribute to the stresses on the coatings:

1. shrinkage caused by densification of low-density coatings,
2. swelling of high-density coatings, and
3. dilation at constant volume caused by expansion in the "c" direction and contraction in the "a" direction of the individual crystallites.

These processes are affected both by temperature and structural features of the coating, such as crystallite size and preferred orientation.

The processes going on in an individual crystallite are similar to those in graphite, which are described in Chapter 37, and are best visualized with reference to data obtained by irradiating massive samples of pyrolytic carbon with a high degree of crystallite perfection. Typical data obtained from duplicate samples of pyrolytic carbon deposited at 2200°C and irradiated at about 650°C are shown in Fig. 8.40. The initial density of this material was 2.20 g/cm^3, and the BAF was greater than 300. A large expansion in the "c" direction (i.e., perpendicular to the plane of deposition) is observed with a concurrent contraction in the "a" direction. For the sample used, the basal planes correspond to the surface of deposition. The data in Fig. 8.40 are for a single temperature, but the rates of "c" axis expansion and "a" axis contraction are highly temperature dependent.

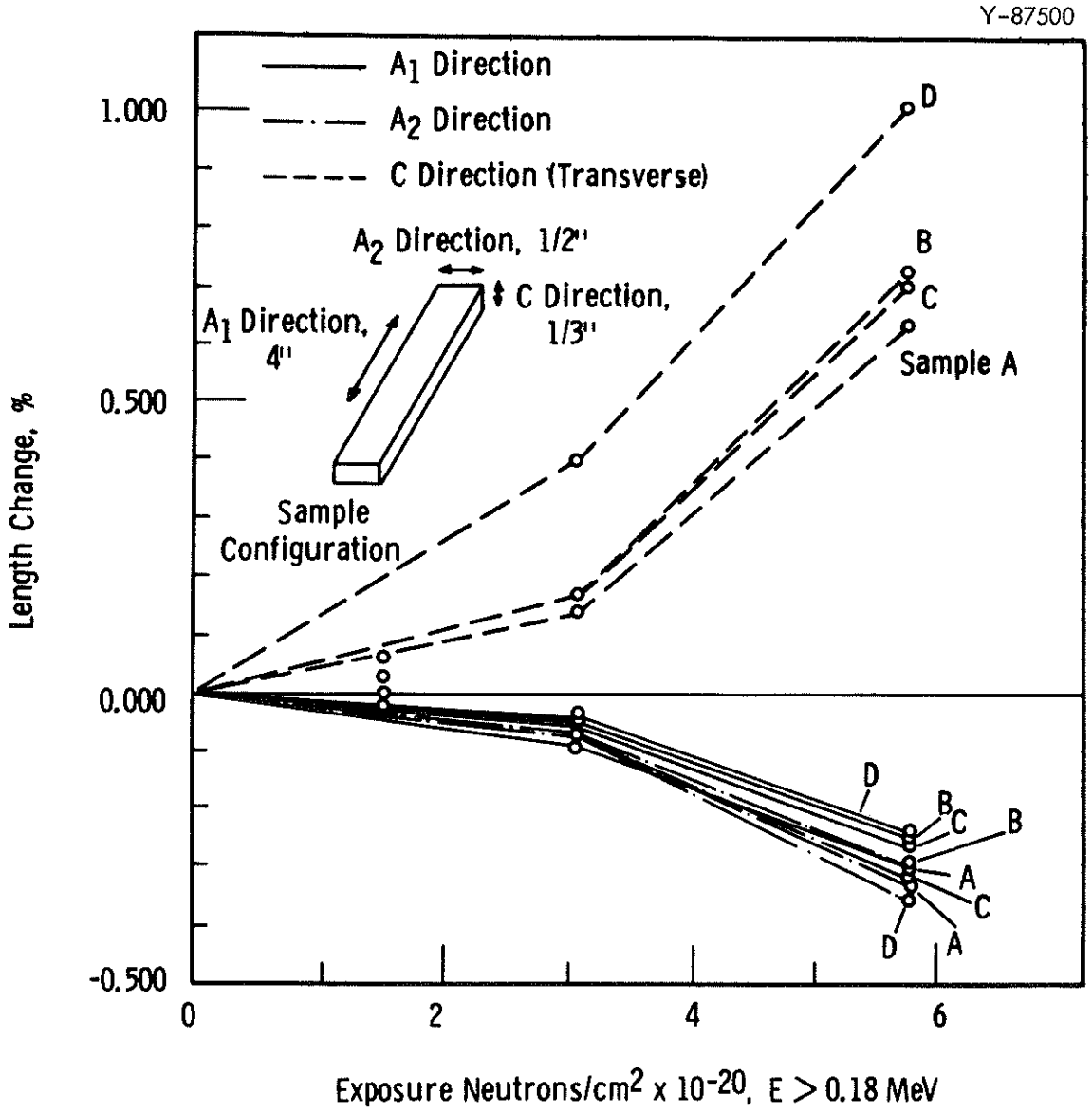

Fig. 8.40. Radiation-induced length changes in pyrolytic graphite. Irradiation temperature was approximately 650°C. Reprinted from reference 69.

For polycrystalline samples of pyrolytic carbon with either random or preferred orientation, this process occurs in the individual crystallites making up the structure. The overall strains may be obtained by using crystallite averaging methods discussed by Price and Bokros.[60] The total bulk dimensional changes, $\Delta\ell_{\parallel}/\ell_{\parallel}$ or $\Delta\ell_{\perp}/\ell_{\perp}$, are related to the total crystallite changes, $\Delta X_a/X_a$ and $\Delta X_c/X_c$, by the equation

$$\ell n\left(1+\frac{\Delta\ell_{\perp}}{\ell_{\perp}}\right)=R_{\perp}\,\ell n\left(1+\frac{\Delta X_a}{X_a}\right)+\left(1-R_{\perp}\right)\ell n\left(1+\frac{\Delta X_c}{X_c}\right). \qquad (10)$$

In this expression the symbols $\perp$ and $\parallel$ refer to the directions perpendicular and parallel to the plane of deposition, respectively. The preferred orientation parameter, R, was described previously. $R_{\perp}$ takes a value from 0 to 2/3 and $R_{\parallel}$ from 2/3 to 1. For an isotropic deposit the R value is independent of direction and equals 2/3.

A plot of $\ell n\left(1+\frac{\Delta\ell_x}{\ell_x}\right)$ is given in Fig. 8.41 as a function of R_x for a number of carbon deposits irradiated to a neutron fluence of 2.4×10^{21} neutrons/cm^2 ($E > 0.18$ Mev) at 1040°C. The highest density isotropic carbons showed virtually no density change since the dimensional change is zero at $R_x = 2/3$ for this fluence. Lower density pyrolytic carbons showed densification in proportion to the initial density defect (defined as theoretical density minus the initial density).

The effect of temperature on irradiation-induced dimensional changes for pyrolytic carbons with densities in the range 2.13 to 2.14 g/cm^3 irradiated to a fluence of 1.7 to 2.0×10^{21} neutrons/cm^2 ($E > 0.18$ Mev) is shown in Fig. 8.42. It was found that the rate of "c" axis expansion increases with temperature in the range 680 to 980°C. The net volume change was essentially zero for these high-density samples at the fluence cited.[70]

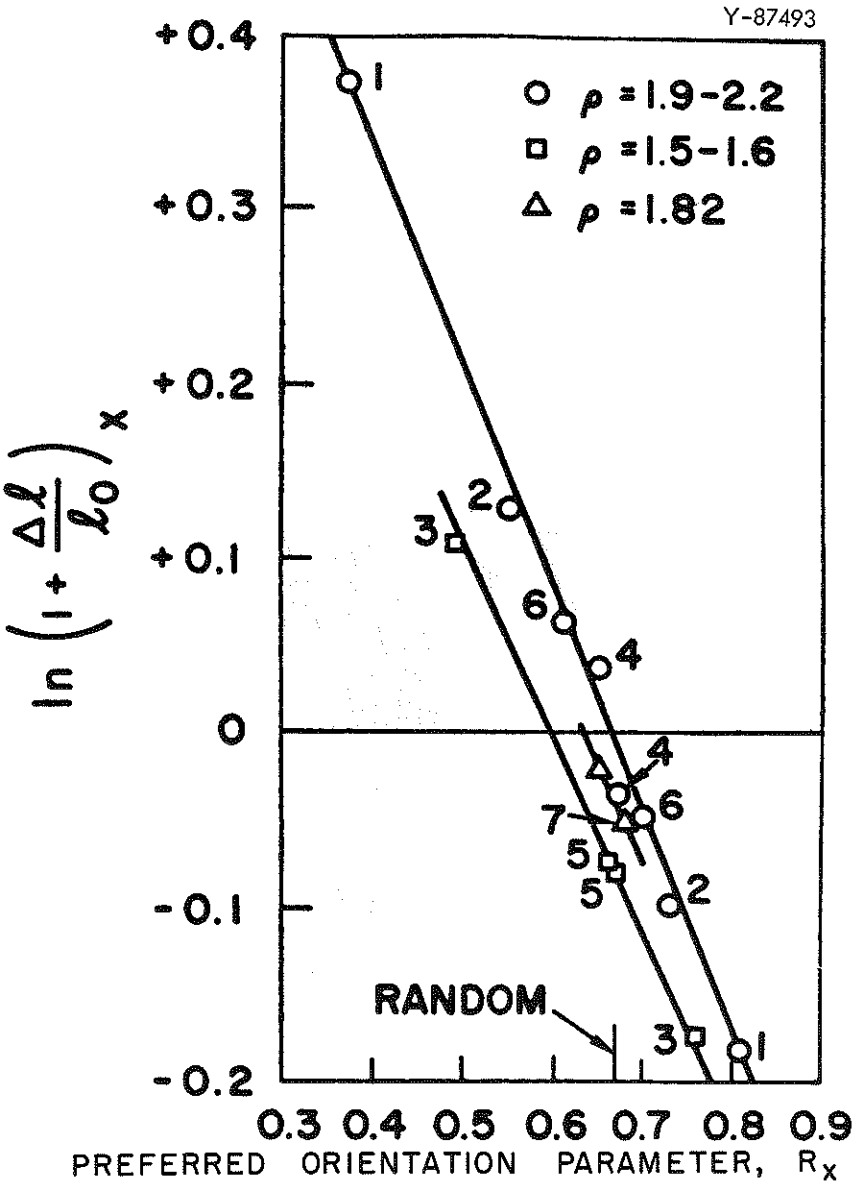

Fig. 8.41. Plot of dimensional changes, $\ln [1 + (\Delta\ell/\ell_o)]_x$, versus preferred orientation parameter, R_x, for as-deposited carbons (numbers beside points correspond to structural designations in Tables 8.11 and 8.12). Irradiated at 1040°C to a neutron exposure of 2.4×10^{21} neutrons/cm^2 (E > 0.18 MeV). Reprinted from reference 66.

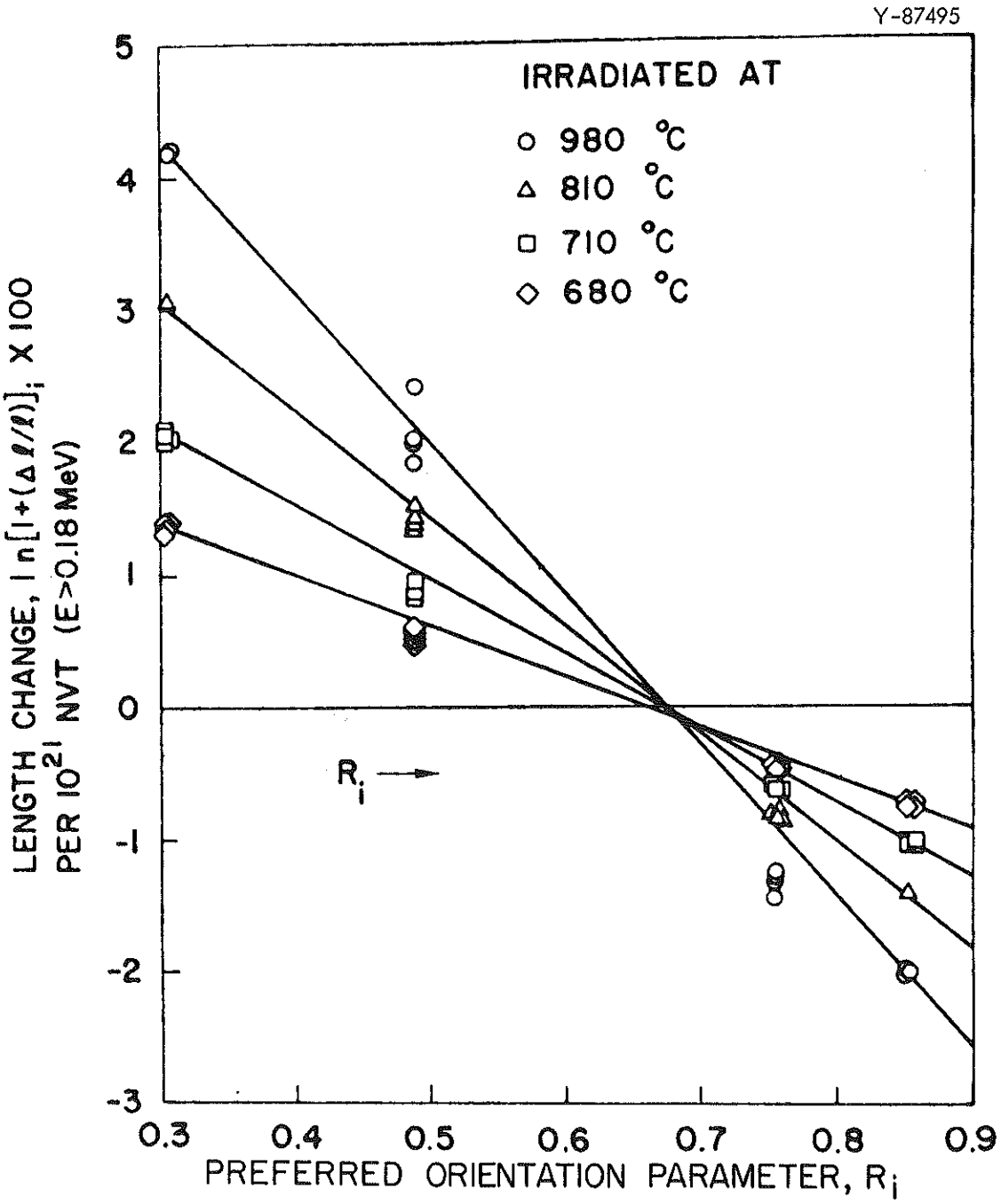

Fig. 8.42. Length changes, ln $(1 + \Delta\ell_i/\ell_i)$ per 10^{21} neutrons/cm^2 (E > 0.18 MeV) plotted as a function of the corresponding R_i parameter for various irradiation temperatures. Reprinted from reference 70.

Bokros and Schwartz[70] have examined densification in detail. They feel that densification is a first-order process, at least to a fluence of 3×10^{21} neutrons/cm^2 ($E > 0.18$ Mev), so that the following expression applies:

$$\rho = \rho_{th} - (\rho_{th} - \rho_o) \exp(-k_d \gamma) , \qquad (11)$$

where

ρ = the final density, g/cm^3,

ρ_{th} = theoretical density, g/cm^3,

ρ_o = initial density, g/cm^3,

γ = fast-neutron fluence, $E > 0.18$ Mev,

k_d = densification constant, (neutrons/cm^2)$^{-1}$

The densification constant was found to vary with temperature and crystallite size as shown in Fig. 8.43. For small crystals (L_c approx 40 A), the densification constant was only slightly temperature dependent. For intermediate-size crystallites (L_c = 100 to 200 A), the densification constant goes through a sharp minimum at about 500°C and has a value about one-tenth that of the smaller crystallites, increases rapidly above 500°C, and at about 1100°C coincides with that of the smaller size carbon. For very large crystallites from graphitized pyrolytic carbons, the minimum is displaced to a higher temperature and coincidence with the densification constants of the smaller size carbons would occur at some undefined temperature greater than 1100°C. Bokros and Schwartz[70] attribute the variation in densification constant with temperature to mobilities of carbon atoms and of vacancies relative to the crystallite sizes. This in turn determines whether nucleation of interstitial clusters occurs homogeneously or heterogeneously.

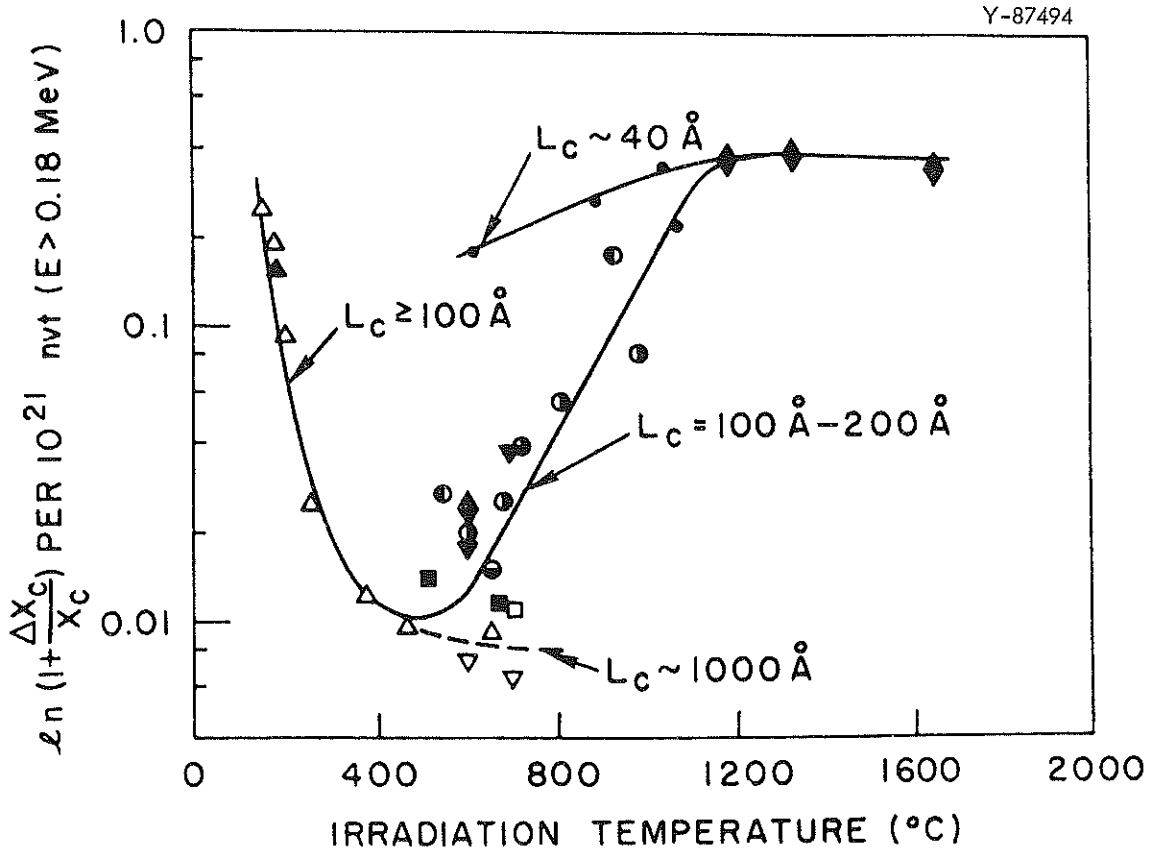

Fig. 8.43. Average crystallite growth rates, ln $(1 + \Delta X_c/\Delta X_c)$ per 10^{21} neutrons/cm^2, for turbostratic carbons (shaded symbols) and graphitized carbons (open symbols) versus irradiation temperature. Data are from materials with densities greater than 2.0 g/cm^3. Reprinted from reference 70.

Although data are limited, Bokros and Schwartz[70] indicate that a breakdown of the first-order densification process may occur at very high fluences ($E > 0.18$ Mev). Eventually one would expect breakaway swelling like that observed on graphite.

8-5.3 Fission-Product Retention by Coated-Particle Fuels

Retention of Fission Gases in Coated Particles

Early tests of coated fuel particles, both in out-of-pile heating experiments after light irradiation[71,72] and in sweep-capsule irradiation experiments,[72–74] demonstrated that as-deposited coatings of pyrolytic carbon and ceramic oxides were quite effective in retaining noble-gas fission products. The monolithic laminar or granular coatings used in early experiments, however, always began to rupture from fission recoil damage after about 5 to 15 days of irradiation. As this occurred, the fractional release (R/B) of krypton and xenon increased by two to four orders of magnitude, and the experiments were ended.

These results showing low initial release fractions were supported by supplementary measurements of the diffusion coefficients of ^{133}Xe in samples of the coatings.[75] The values for the apparent diffusion coefficient were very low ($< 10^{-14}$ cm^2/sec) for dense pyrolytic carbon and ceramic oxide coatings at temperatures up to 1500°C. On this basis, one may calculate that the loss of fission gases by diffusion through dense intact coatings would be insignificant.[75,76] Testing of fuel particles with multilayer coatings that were developed for resistance to irradiation damage confirmed this. In recent tests of two- and three-layer carbon coatings on carbide and oxide fuel particles, the fractional

release (R/B) of noble-gas fission products has remained low ($< 10^{-5}$) even after more than 20% burnup of fuel.[76,77] Results from several of these experiments, shown in Table 8.13, demonstrate the excellent behavior of these coatings on UO_2 fuel particles. It should be emphasized that very few if any ruptured coated particles were present in these experiments, since the fission-gas release from particles without coatings may be greater than 1%.

The successful development of multilayer coatings that will survive after high fuel burnup led to the confirmation of earlier indications[76,78] that the observed release rates of fission gases were caused by fuel contamination within the outer portion of the coating. In Fig. 8.44 release data from four of the experiments in Table 8.13 are plotted versus the coating contamination, which was measured as alpha-particle activity on the particles in the as-coated condition. The resulting curve indicates that release increases in direct proportion to the level of contamination.

In preparing the coated particles tested in these experiments,[77] investigators observed that the contamination levels of the coated oxides were lower by one or two orders of magnitude than those of carbide particles coated under similar conditions. This was attributed to the relative stability of UO_2 particles with dense carbon coatings at temperatures up to 2300°C. Carbide fuels, on the other hand, tend to diffuse into and contaminate coatings applied at temperatures of 1800°C and above. This is further shown by results from a series of coating experiments on $(Th,U)C_2$ particles.[42] At a constant methane concentration the surface α-count (contamination) is seen in Fig. 8.45 to increase in

Table 8.13. Fission-Gas Release from Pyrolytic-Carbon-Coated Uranium Oxide Fuel Particles During Irradiation

Capsule	Batch	Coating	Burnup (at. % U)	Temperature (°C)	Average Fractional Fission-Gas Release, R/B				
					^{85m}Kr	^{88}Kr	^{87}Kr	^{133}Xe	^{135}Xe
A9-2	OR-298	Gap + Anisotropic + Granular	27.9	1400	9.3×10^{-7}[b] 8.5×10^{-8}[c]	7.0×10^{-7}[b] 4.9×10^{-6}[c]	5.7×10^{-7}[b] 3.4×10^{-6}[c]	11.7×10^{-7}[b] d	6.5×10^{-7}[b] d
B9-26	OR-354	Porous Carbon + Isotropic	12.1	1350	4.7×10^{-6}	4.2×10^{-6}	3.9×10^{-8}	3.7×10^{-6}	1.7×10^{-8}
B9-27	OR-348	Porous Carbon + Dense Isotropic	9.4	1500	1.6×10^{-6}	1.3×10^{-6}	1.2×10^{-6}	1.0×10^{-6}	0.6×10^{-6}
C1-16	OR-343	Isotropic I + Isotropic II	11.9	1400	1.1×10^{-7}	0.8×10^{-7}	0.6×10^{-7}	0.9×10^{-7}	0.4×10^{-7}
			2.8	1500	1.9×10^{-7}	1.4×10^{-7}	1.2×10^{-7}	1.7×10^{-7}	0.7×10^{-7}
			14.7	1400[a]	1.1×10^{-7}	0.8×10^{-7}	0.7×10^{-7}	d	d
C1-17	OR-HB23	Porous Carbon + Granular	25.2	1600	6.2×10^{-8}	4.3×10^{-8}	3.9×10^{-8}	7.6×10^{-8}	5.4×10^{-8}

[a] After 2.8% burnup at 1500°C.

[b] Before bursts of fission gas.

[c] After bursts of fission gas.

[d] Data not available.

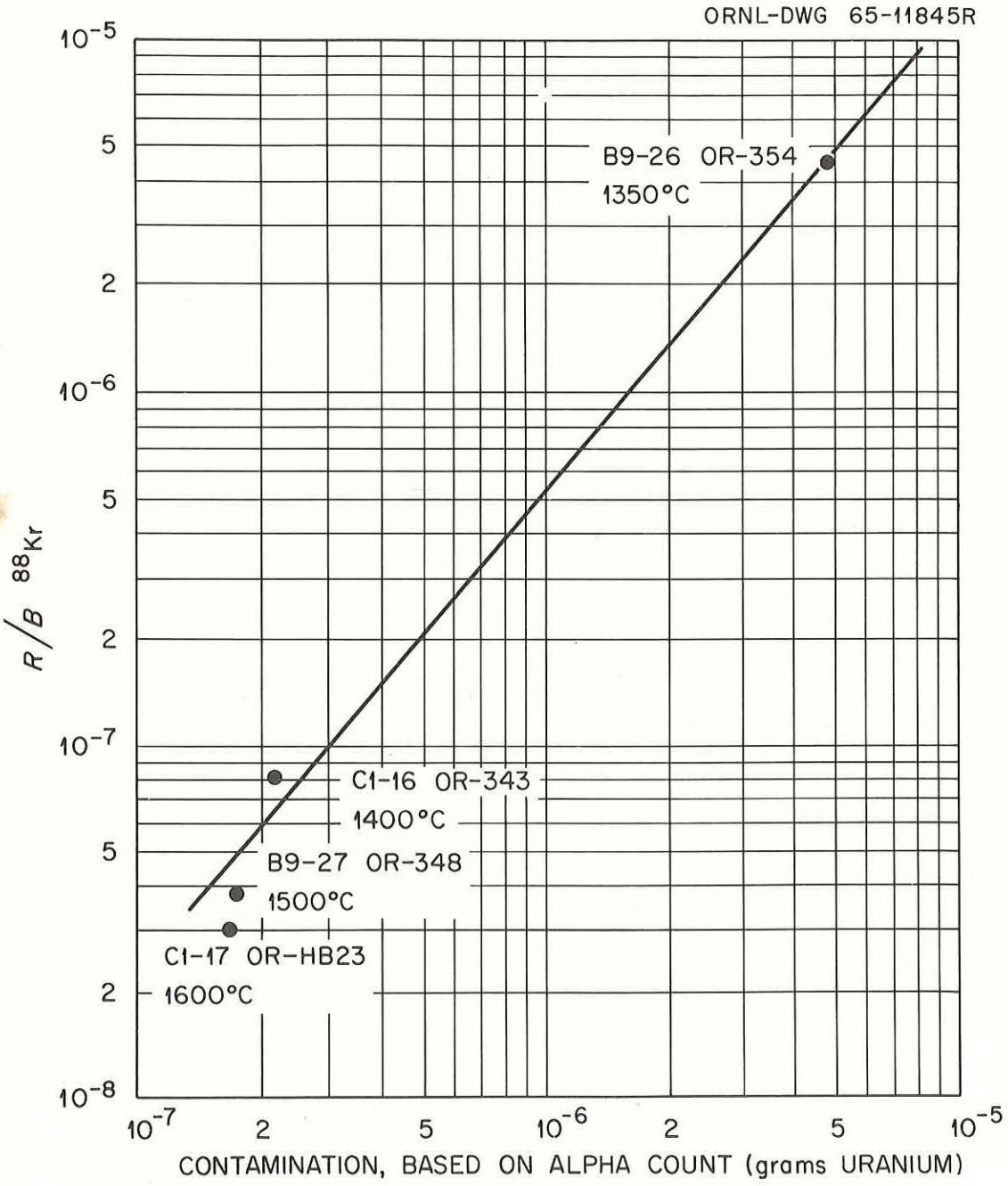

Fig. 8.44. Relationship between fission-gas release and coating contamination. Reprinted from reference 77.

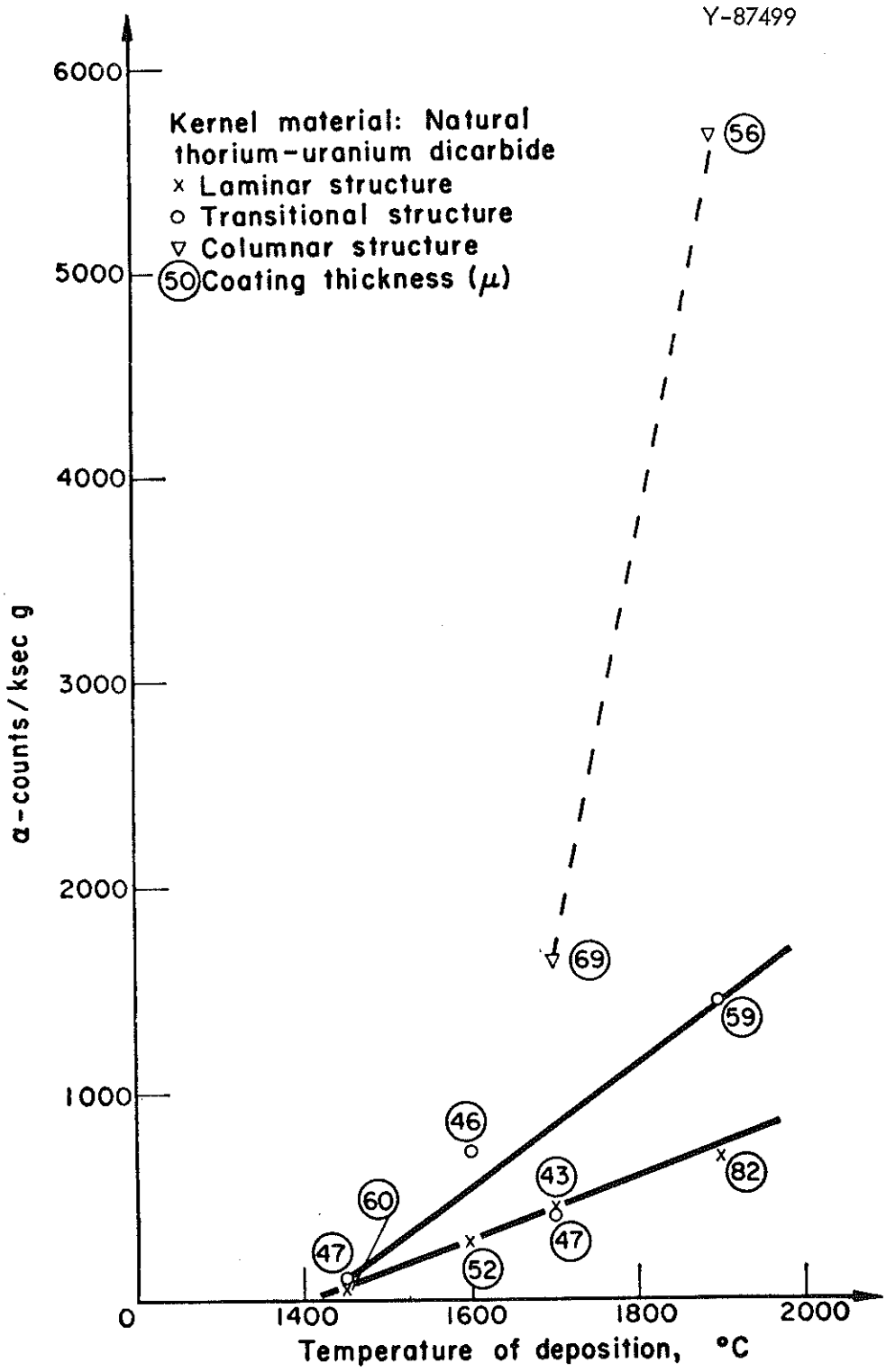

Fig. 8.45. Dependence of α-count on temperature of deposition. Reprinted from reference 42.

direct relation to the deposition temperature. The much higher contamination levels for the columnar structures were attributed to the longer coating runs required to produce this structure. Coating times for the other samples were quite comparable, which indicates that migration is somewhat sensitive to the structure of the coating.

In summary, one may conclude that virtually all of the fission-gas release observed from intact coated particles is derived from fissile materials in the outer layer of the coatings. Therefore, one finds good reason to reduce such contamination of the coatings by using oxide fuel particles, depositing coatings at lower temperatures, or using barrier layers in the coating.

Behavior of Solid Fission Products

In contrast to the low fractional release rates of the noble-gas fission products, certain solid fission products may diffuse readily through carbon coatings and thus contribute to contamination of the primary coolant system in HTGRs and other high-temperature reactors.

Behavior of Iodine. In some early experiments on release of fission products during heating of lightly irradiated coated particles, moderate-to-large releases of iodine were observed.[72,79] Later studies on improved coated particles, however, during heating after light irradiation and during high-temperature irradiation capsule experiments, indicated that virtually all the iodine released is derived from surface contamination and/or broken coated particles. In a typical, in-reactor swept experiment, Reagan et al.[74] showed that part of the xenon released during irradiation actually escapes from the coated particles as iodine

and that the iodine release fractions are of the same order of magnitude as those of the noble gases. Thus one may conclude that the release rate of iodine from intact coated particles will be a function of the surface contamination on the coatings and that iodine release will be a problem only if a significant fraction of coatings are ruptured. Moreover, recent data indicate that iodine release from broken coated particles will be moderate unless irradiation temperatures are greater than 1500°C (refs. 80, 81). In postirradiation heating experiments, coated UC_2 particles that were broken after irradiation released only about 1% of the ^{131}I during 1 hr at 1250°C (ref. 80). Analysis of coating fragments disclosed that nearly half of the iodine inventory was retained in fragments of the porous inner coating.

Metallic Fission Products. On the other hand, high fractional releases of some metallic fission products have been observed during heating of lightly irradiated coated particles that released very small or undetectable amounts of ^{133}Xe. In an early series of experiments, Scott et al.[71] observed significant release of ^{140}Ba and detectable amounts of ^{103}Ru from intact carbon-coated UC_2 particles. Further work by Scott and Toner[82] disclosed that large fractions (approx 10%) of ^{111}Ag were released at temperatures as low as 1000°C. Other early experiments confirmed the release of significant fractions of ^{137}Cs, ^{141}Ce, ^{89}Sr, and ^{147}Nd from intact pyrolytic-carbon-coated fuel particles at high temperatures.[72,79,83]

Much work has since been done on the characterization of metallic fission-product release.[80,84,85] While the mechanisms of release are not understood, data on the magnitude of release fractions of given

fission-product isotopes are available. The situation as regards pyrolytic-carbon-coated fuel particles may be summarized as follows:

1. The density and structure of carbon coatings have little if any effect on release rate of metallic products.

2. Significant fractions ($\geq$ 10%) of strontium, barium, and silver isotopes may be released from the coated particles, especially at temperatures above about 1200°C. Since these elements diffuse readily through pyrolytic carbon, their release rates are determined to some extent by the composition and structure of the fuel particle.

3. Small fractions ($<$ 1%) of cesium, cerium, and yttrium isotopes will be released from carbon-coated carbide fuels.

4. Cerium and yttrium, both of which form very stable oxides, are retained almost quantitatively by coated oxide fuels.

5. Release of all other metallic fission products is barely detectable.

The high fractional release of strontium, and to a lesser extent barium, aroused grave concern for the safety of HTGR systems and led to the development of barrier coatings containing SiC layers sandwiched between carbon coatings. Such barrier coatings are very effective containment for strontium and barium,[86–88] reducing the fractional release of these isotopes by as much as 10^{-4}. The release of cesium, however, is virtually unaffected by the presence of the SiC barrier. Other metallic species are released in lesser amounts than from carbon-coated particles, perhaps because SiC barrier coatings tend to be less contaminated than carbon coatings.

8-5.4 Performance of Coated-Particle Fuels

Numerous irradiation experiments have confirmed that coated-particle fuels are capable of performing without failures at extreme conditions of temperature, burnup, and fast-neutron fluence, as shown in Table 8.14. The few samples listed were selected from many batches of well-characterized coated particles tested in these and similar experiments. The particle coatings were designed and prepared according to principles discussed elsewhere in this chapter, and their operating conditions are shown here to illustrate present capabilities of this type of nuclear fuel.

8-6 EFFECTS OF IRRADIATION ON OXIDE OR CARBIDE COATINGS

The behavior of oxide coatings, such as BeO, MgO, and Al_2O_3, or carbide coatings, such as SiC, under irradiation is essentially the same as that observed for bulk material. Therefore, refer to Chapters 27 and 38 of this handbook for the appropriate information.

8-7 COATED-PARTICLE DESIGN

8-7.1 Introduction

The specifying of a coated-particle design requires of one the ability to predict quantitatively the influence of a coated particle's configuration and material properties on its expected life to failure in a given irradiation environment. To facilitate such predictions, mathematical models describing coated-particle irradiation behavior have been developed.[4,94–97] Although such models alone cannot be used for

Table 8.14. Performance of Selected Coated-Particle Fuel Samples in Irradiation Experiments[a]

Fuel Composition	Coating Type[b]	Irradiation Conditions			Experiment Reference[c]
		Burnup % Heavy Metal	Temperature (°C)	Fast (E > 0.18 Mev) Neutron Fluence (neutrons/cm^2)	
				$\times 10^{21}$	
$(Th,U)C_2$	BISO	16.4	1270	5.0	P-14B
$(Th,U)C_2$	BISO	23.2	1230	3.7	P-15
$(Th,U)C_2$	TRISO	20.0	1300	4.0	P-13J
$(Th,U)C_2$	Duplex	10.1	1300	0.7	B9-28[d]
$(Th,U)O_2$	BISO	3.0	1165	2.7	P-13E
UC_2	BISO	49.0	1200	1.5	F9-1
UO_2	Triplex	44.4	1150	1.5	F9-1
UO_2	BISO	25.4	1400	0.1	XB-2
ThO_2	BISO	0	1200	5.0	DFR-3

[a]Samples performing without failure.

[b]Coating types are:

BISO: inner porous buffer layer, outer isotropic carbon layer.
TRISO: SiC layer between two layers of BISO.
Duplex: inner laminar layer, granular outer layer.
Triplex: BISO with outer third layer of granular pyrolytic carbon.

[c]Experiment (1) P-capsule experiments conducted by Gulf General Atomic (refs. 89, 90).
(2) F9 high-burnup ORR experiments at ORNL (ref. 91).
(3) XB-2 (ETR X-Basket No. 2) and DFR-3 experiments conducted by ORNL (refs. 65, 92).

[d]Proof-test of coated particles for AVR (ref. 93).

reliable a priori predictions of coated-particle failure, they do provide a rational means for interpolation between limited irradiation test results and for assessing the relative influence of various coated-particle design variables on expected irradiation performance.

8-7.2 Mechanisms of Coating Failure

Coated-particle failure implies the rupture of the impervious coating layer or layers that provide primary containment for fission products released from the fuel kernel. The rupture will occur when some function of the stress-strain state in the coating exceeds a critical value. Coating stresses leading to failure can result from one or more of the following causes:[4,95]

1. swelling of the fuel kernel (from differential thermal expansion or fission) against the inner surface of the coating,
2. fission-gas pressure exerted against the inner surface of the coating,
3. coating distortion caused by direct fission fragment bombardment of the inner surface of the coating,
4. coating distortion caused by chemical reaction of fission products with the inner surface of the coating, and
5. coating distortion caused by anisotropic dimensional changes (from thermal expansion or fast-neutron damage) throughout the coating.

Early irradiation experience with pyrolytic-carbon-coated fuel particles demonstrated that the first four of these causes [especially (1) and (3)] would lead to early failure of single-layer coatings.[95] Hence, multilayer coatings were developed, incorporating a low-density "buffer"

layer immediately surrounding the fuel kernel, surrounded by one or more high-density, impervious layers to provide fission-product containment. The buffer layer contributes little, if any, mechanical strength of its own, but serves to prevent outer layer damage from fission fragments, chemical reaction, or fuel expansion; it also provides volume to accommodate released fission gases through its internal porosity and densification under irradiation, thereby greatly reducing the gas pressure exerted against the outer coating. Note also that additional fission-gas volume can be obtained through use of a fuel kernel of less than theoretical density. Subsequent discussion in this section will concern particles with two coating layers; a low-density inner buffer layer, and an impervious, outer containment layer, as shown schematically in Fig. 8.46.

8-7.3 Mathematical Models

Mathematical models of coated-particle irradiation behavior proposed to date are based on a calculation of stress and strain in the outer containment layer, considered as a thick-walled spherical pressure vessel. It is assumed in all models that the buffer coating is sufficiently thick to shield the outer layer completely from mechanical or chemical interaction with fission fragments. The models differ in the assumptions they incorporate concerning the significance of various failure mechanisms and the mechanical behavior of the outer coating.

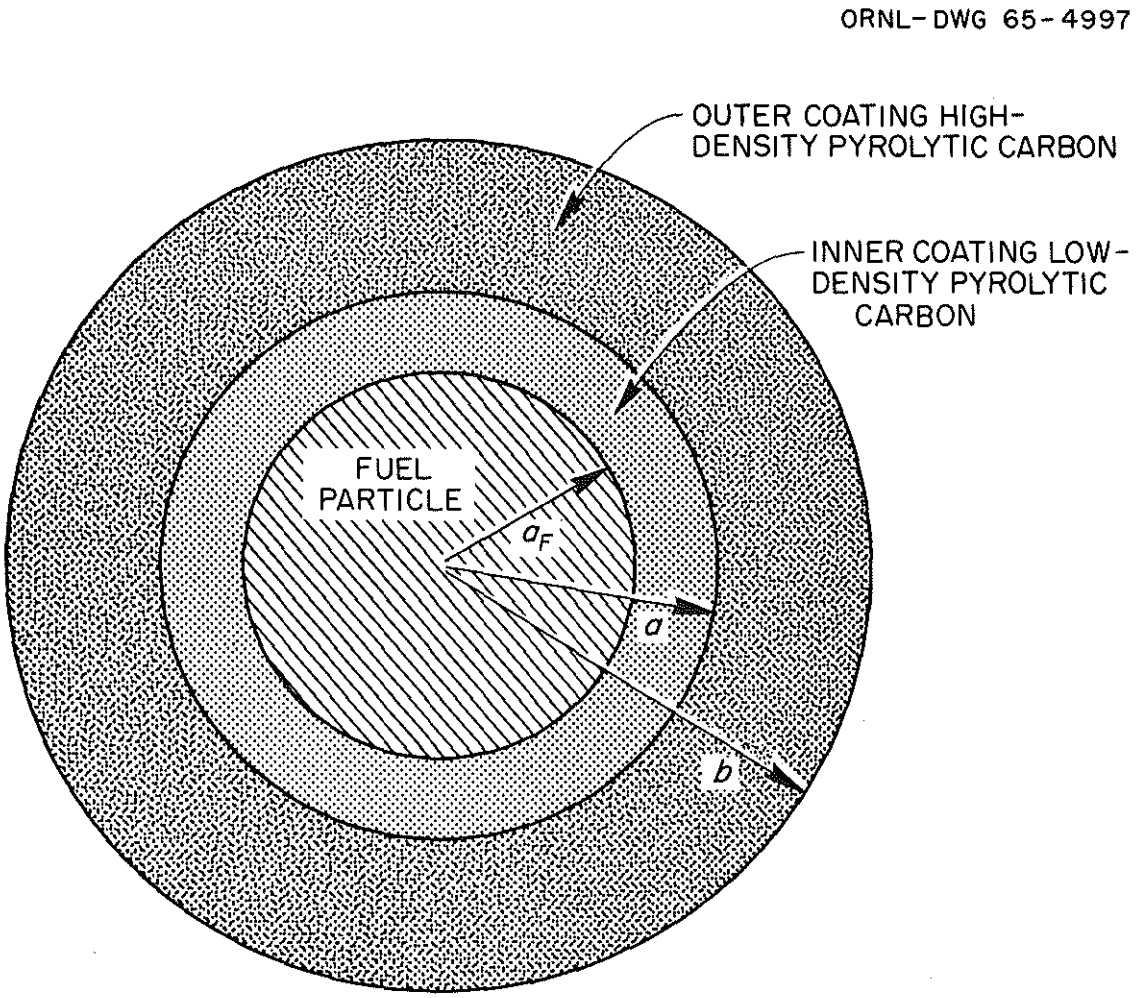

Fig. 8.46. Model of fuel particle with two-layer coating. Reprinted from reference 94.

Figure-of-Merit Model

A simple model of coated-particle performance is embodied in the "figure-of-merit" concept described by Schwartz.[96] In this model it is assumed that (1) the outer coating is isotropic and elastic with uniform properties throughout, (2) the volume available for fission gas is not significantly affected by swelling of the fuel or by shrinkage and elastic deflection of the outer coating, and (3) failure will occur when the tangential tensile stress in the outer coating exceeds some specified value.

These assumptions lead to the following equation for predicting the burnup required to cause coating failures:

$$Bu_f = G \left\{ \frac{\sigma_M \left[\left(\frac{b}{a} \right)^3 - 1 \right] \left\{ \left[\left(\frac{a}{a_F} \right)^3 - 1 \right] \epsilon_G + \epsilon_F \right\}}{T \left[\left(\frac{b}{a} \right)^3 + 2 \right]} \right\}, \qquad (12)$$

where

Bu_f = percent burnup at failure, 100× (fissions per initial heavy metal atom),

σ_M = tangential stress in outer coating necessary to cause rupture,

b, a, a_F = coated-particle dimensions (see Fig. 8.46),

ϵ_G = fraction of buffer coating volume available to accommodate fission gas,

ϵ_F = fraction of fuel kernel volume available to accommodate fission gas, and

T = absolute temperature.

The quantity G is defined as

$$G = \frac{2}{CfZR} , \tag{13}$$

where

f = fraction of fission gas produced that is released from solid fuel lattice,

Z = generalized gas compressibility factor (ref. 98),

R = universal gas constant, and

C = the gram-moles of fission gas produced in a unit volume of fuel per atom percent of heavy metal fissioned, calculated as

$$C = \frac{\gamma_G (1 - \epsilon_F) h_F \rho_F}{100 M_F} , \tag{14}$$

where

γ_G = yield of gaseous fission products, gram-moles produced per gram atom of heavy metal fissioned (value is roughly 0.24),

h_F = atoms of heavy metal per molecule of fuel material (e.g., 1 for UO_2, 3 for U_3O_8, etc.),

ρ_F = theoretical density of fuel material, and

M_F = molecular weight of fuel.

The "Figure of Merit," FM, for an irradiated coated particle is then defined as the ratio of the burnup at failure predicted from Eq. (12) to the actual burnup attained, Bu:

$$FM = \frac{Bu_f}{Bu} . \tag{15}$$

Schwartz obtained a good correlation of the percentages of failed particles in given lots as functions of their Figures of Merit, in a series of accelerated-burnup irradiation experiments.[96]

ORNL Model (Prados and Scott)

The relations employed in the Figure-of-Merit model should provide a reasonable representation of the performance of coated particles with fuel kernels having a high concentration of fissile material. This is because such particles attain a high burnup before they accumulate a significant fast-neutron exposure, and hence burnup effects (primarily fission-gas pressure) contribute far more to the coating stress than do fast-neutron effects (anisotropic dimensional changes and creep relaxation of stress). Equations (12) and (13) would not be valid, however, for particles subjected to fast-neutron exposures above about 5×10^{20} neutrons/cm^2 ($E > 0.18$ Mev); above this level, fast-neutron-induced shrinkage, anisotropic distortion, and creep can significantly alter the coating stress state from that caused by internal pressure alone. To treat such cases, Prados and Scott have formulated a model[4,94] which permits calculation of stress and strain in a spherical pyrolytic-carbon coating under the influence of internal fission-gas pressure acting in combination with fast-neutron-induced shrinkage and distortion. The most recent version also accounts for the creep exhibited by pyrolytic-carbon coatings under fast-neutron irradiation.

The interaction between fission-gas pressure, coating stress, and coating displacement necessitates a trial-and-error solution for the stress distribution, even when elastic behavior of the coating is assumed.[94] The computational difficulties are significantly increased by the inclusion of creep, since this introduces nonlinearity and time dependence into the equations governing stress and strain in the spherical coatings and makes it impossible to obtain explicit solutions

for the stress distribution. The approach employed by Prados and Scott for calculation of the outer coating stress distribution in the presence of creep is based on the iterative numerical procedure of Mendelson et al.[99] This technique requires equations giving the distribution of principal stresses in the system in terms of initially unknown (and hence arbitrary) creep displacements. Stresses calculated from these relations are used to obtain successively improved values of creep strains until all system-governing equations are satisfied over a given small-time increment. The process is repeated over successive time intervals to build up a stress-strain history for the system.

Working equations have been developed for the Prados-Scott model[4,94,95,97] and they may be summarized as follows.

Coating Stress Components as Functions of Coating Dimensions and Properties, Fission-Gas Pressure, and Nonelastic Strain Components:

$$\sigma_\theta(r) = \frac{p}{2}\left[\frac{(n_1+2)\left(\frac{b}{a}\right)^{n_2}\left(\frac{r}{a}\right)^{n_1} - (n_2+2)\left(\frac{b}{a}\right)^{n_1}\left(\frac{r}{a}\right)^{n_2}}{\left(\frac{b}{a}\right)^{n_1} - \left(\frac{b}{a}\right)^{n_2}}\right] + \frac{E_\theta}{(1-\nu_1)(n_1-n_2)}$$

$$\times\left\{\left[I_1\left(\frac{b}{a}\right) - I_2\left(\frac{b}{a}\right)\right]\left[\frac{(n_2+2)\left(\frac{r}{a}\right)^{n_2} - (n_1+2)\left(\frac{r}{a}\right)^{n_1}}{\left(\frac{b}{a}\right)^{n_1} - \left(\frac{b}{a}\right)^{n_2}}\right]\right.$$

$$\left. + (n_1+2)I_1\left(\frac{r}{a}\right) - (n_2+2)I_2\left(\frac{r}{a}\right)\right\}. \qquad (16)$$

and

$$\sigma_r(r) = -p\left[\frac{\left(\frac{b}{a}\right)^{n_1}\left(\frac{r}{a}\right)^{n_2} - \left(\frac{b}{a}\right)^{n_2}\left(\frac{r}{a}\right)^{n_1}}{\left(\frac{b}{a}\right)^{n_1} - \left(\frac{b}{a}\right)^{n_2}}\right] + \frac{2E_\theta}{(1-\nu_1)(n_1-n_2)}$$

$$\times\left\{\left[I_1\left(\frac{b}{a}\right) - I_2\left(\frac{b}{a}\right)\right]\left[\frac{\left(\frac{r}{a}\right)^{n_2} - \left(\frac{r}{a}\right)^{n_1}}{\left(\frac{b}{a}\right)^{n_1} - \left(\frac{b}{a}\right)^{n_2}}\right] + I_1\left(\frac{r}{a}\right) - I_2\left(\frac{r}{a}\right)\right\}, \qquad (17)$$

where

σ_θ, σ_r = tangential and radial components, respectively, of normal stress in the outer coating,

p = pressure on inner coating surface,

a, b = inner and outer radii of spherical outer coating,

n_1, n_2 = roots of quadratic equation, $n^2+3n+2\left[1 - \frac{E_\theta(1-\nu_2)}{E_r(1-\nu_1)}\right] = 0$, and

$E_\theta, E_r, \nu_1, \nu_2$ = elastic moduli and Poisson's ratios for outer coating.

The quantities I_1 and I_2 appearing in Eqs. (16) and (17) are integral functions defined as

$$I_i\left(\frac{r}{a}\right) = \left(\frac{r}{a}\right)^{n_i} g_\theta(1) - g_\theta\left(\frac{r}{a}\right) + \left(\frac{r}{a}\right)^{n_i}\int_1^{\frac{r}{a}} \frac{g_r - (1+n_i)g_\theta}{y^{(n_i+1)}}\,dy \;; \quad i = 1,2. \qquad (18)$$

Nonelastic Strain Components as Functions of Coating Temperature, Fast-Neutron Damage, and Stress: The quantities g_θ and g_r appearing in Eq. (18) are the tangential and radial components of coating strain contributed by causes other than elastic response to stress and are calculated as

$$g_\theta(r) = \alpha_\theta \left[T(r) - T_c\right] + \eta_\theta(r) + \int_o^t \dot{\epsilon}_{\theta c}\, dt \ , \tag{19}$$

and

$$g_r(r) = \alpha_r \left[T(r) - T_c\right] + \eta_r(r) + \int_o^t \dot{\epsilon}_{rc}\, dt \ , \tag{20}$$

where

α_θ, α_r = tangential and radial thermal expansion coefficients for coating,

η_θ, η_r = tangential and radial components of unrestrained fractional fast-neutron-induced dimensional change in coating,

T = temperature at a point in coating,

T_c = temperature at which coating was deposited, and

t = time.

Components of Creep-Strain Rates in Coating as Functions of Coating Properties, Fast-Neutron Flux, and Stress: Relations for the creep-strain rates in terms of the stress components are based on a modification of Hill's theory of anisotropic plastic yielding[97,100] and are as follows:

$$\dot{\epsilon}_{\theta c} = A_r \left(\frac{\dot{\bar{\epsilon}}}{\bar{\sigma}}\right)\left(\frac{\sigma_\theta - \sigma_r}{2}\right) , \tag{21}$$

$$\dot{\epsilon}_{rc} = A_r \left(\frac{\dot{\bar{\epsilon}}}{\bar{\sigma}}\right)\left(\sigma_r - \sigma_\theta\right) , \tag{22}$$

where $\dot{\bar{\epsilon}}$ is an effective creep-strain rate, given by

$$\dot{\bar{\epsilon}} = \sqrt{\frac{\dot{\epsilon}_{rc}^2}{A_r}} \ . \tag{23}$$

Here, A_r is an anisotropic yield coefficient, given approximately by the ratio of tangential to radial elastic moduli, E_θ/E_r, and $\bar{\sigma}$ is the "plastic potential" or effective creep stress, related experimentally to the creep strain and strain rate. The form of this relation is that suggested by Price and Bokros.[68] It is assumed that when pyrolytic carbon is placed under load in a fast-neutron flux, three types of deformation occur: (1) instantaneous elastic strain; (2) a rapid, recoverable, "primary" creep strain, approximately equal to the elastic strain; and (3) a steady, irreversible, "secondary" creep at a strain rate proportional to the effective creep stress and the fast-neutron flux, as given by the equation

$$\dot{\bar{\epsilon}} = K\Phi_f\bar{\sigma} \ , \tag{24}$$

where

K = steady-state creep coefficient [of the order of 10^{-27} $(\text{psi})^{-1}$ $(\text{neutrons/cm}^2)^{-1}$], and

Φ_f = fast-neutron flux [neutrons cm^{-2} sec^{-1} $(E > 0.18$ Mev)].

The primary creep strain may be automatically incorporated into the stress calculations, Eqs. (15) and (16), by use of modified elastic property values computed as follows:

$$E'_\theta = 0.5\ E_\theta \ , \tag{25}$$

$$E'_r = 0.5\ E_r \ , \tag{26}$$

$$\nu'_1 = \frac{\nu_1 + 0.5\ (E_\theta/E_r)}{1 + (E_\theta/E_r)} \tag{27}$$

and

$$\nu'_2 = \frac{\nu_2 + 0.5}{2} \tag{28}$$

where

E'_θ, E'_r = effective tangential and radial Young's moduli, modified for effect of primary creep, and

ν'_1, ν'_2 = effective tangential and radial Poisson's ratios, modified for effect of primary creep.

Fission-Gas Pressure as a Function of the Volume, Temperature, and Amount of Gas Present: Fission-gas pressures are calculated using the Redlich-Kwong equation of state,[101] recommended for noble gases at elevated temperatures and pressures:

$$p = \frac{RT}{(V_G/n) - \hat{b}} + \frac{\hat{a}}{(V_G/n)\,(V_G/n + \hat{b})\,T^{0.5}} \tag{29}$$

where

T = average absolute temperature of fission gas,

V_G = total volume of fission gas,

n = moles of fission gas present,

R = universal gas constant, 82.057 cm^3-atm-$(g\ mole)^{-1}$-$(°K)^{-1}$, and

$\hat{a}, \hat{b}$ = constants for specific gases, taken as 6.48×10^{11} atm-$(°K)^{0.5}$-cm^6-$(g\ mole)^{-2}$, and 28.2 cm^3 $(g\ mole)^{-1}$, respectively, for fission-gas mixture.

Amount of Fission Gas as a Function of Fuel Properties and Burnup: The gram-moles of fission gas present within a coated particle, n, is given by

$$n = 4/3\ \pi a_F^3\ CfBu\ , \tag{30}$$

where

a_F = fuel kernel radius,

Bu = burnup of fuel, 100 fissions per initial heavy metal atom, and

C is given by Eq. (14).

The fraction of the fission gas generated that is released from the kernel, f, can be estimated directly or calculated from diffusional relations.[95]

Fission-Gas Volume as a Function of Fuel Properties, Burnup, Coating Dimensions and Properties, and Coating Displacement: The fission-gas volume is computed as

$$V_G = 4/3\ \pi\ (a^3 - a_F'^3) - V_U\ , \tag{31}$$

with a_F' the equivalent radius of a zero-porosity kernel,

$$a_F'^3 = a_F^3\ (1 - \epsilon_F)\ , \tag{32}$$

where ϵ_F equals the actual porosity of fuel kernel and V_U is the inner coating volume unavailable for fission gas, given by

$$V_U = 4/3\ \pi\ (a_o^3 - a_{Fo}^3)\ (1 - \epsilon_G)\ , \tag{33}$$

where a_o and a_{Fo} equal the initial radii of inner coating and fuel kernel, respectively, and ϵ_G equals the fraction of inner coating volume available to accommodate fission gas and fuel swelling. The swelling and/or compression of the fuel kernel during irradiation is computed from the following relations:

$$a_F' = a_{Fo}' \left(1 + \frac{\Delta V_F}{V_{OF}}\right)^{1/3} \left[1 + \alpha_F\ (T_F - T_C) - \frac{p\ (1-2\nu_K)}{E_K}\right]\ , \tag{34}$$

where

T_F = average fuel temperature,

α_F = fuel thermal expansion coefficient,

E_K, ν_K = Young's modulus and Poisson's ratio for fuel kernel,

and the fractional volume increase of the fuel kernel due to solid fission products, $\Delta V_F/V_{OF}$, is given by

$$\frac{\Delta V_F}{V_{OF}} = \frac{\rho_F h_F}{M_F} \left[\xi_1 \Delta V_1 + \xi_2 \Delta V_2 + \xi_3 \Delta V_3 + \xi_4 \Delta V_4 \right] , \qquad (35)$$

where

ΔV_1 = volume change per gram-atom of metal for fission of ^{235}U, $[50.4\ (1 - 0.12\ f) - 12.32]$ cm^3/gram-atom

ΔV_2 = volume change per gram-atom of metal for transformation of ^{232}Th to ^{233}Pa, -4.77 cm^3/gram-atom,

ΔV_3 = volume change per gram-atom of metal for decay of ^{233}Pa to ^{233}U, -2.915 cm^3/gram-atom, and

ΔV_4 = volume change per gram-atom of metal for fission of ^{233}U, $[50.4\ (1 - 0.12\ f) - 12.21]$ cm^3/gram-atom.

The volume changes associated with each nuclear transformation above are computed from the values given by Brinkman.[102] The extents of reaction for each nuclear transformation, ξ_i, (atom events per initial heavy metal atom present), are obtained from the standard exponential solutions to the nuclear kinetic equations.

The distortion of the outer coating is accounted for through equations of the form

$$a = a_o \left[1 + g_\theta(a) + \left(\frac{1-\nu_1}{E_\theta}\right) \sigma_\theta\ (a) - \left(\frac{\nu_2}{E_r}\right) \sigma_r\ (a) \right] \tag{36}$$

and

$$b = b_o \left[1 + g_\theta(b) + \left(\frac{1-\nu_1}{E_\theta}\right) \sigma_\theta\ (b) - \left(\frac{\nu_2}{E_r}\right) \sigma_r\ (b) \right] \tag{37}$$

In practice, the dimensions are revised incrementally after each time increment in the calculations. Equations (15) through (37) do not permit explicit determination of the coating stress components. The coating stresses depend on the functions I_1 and I_2 which depend on the time integrals of the creep strain rates, $\dot{\epsilon}_{\theta c}$ and $\dot{\epsilon}_{rc}$, through Equations (18), (19), and (20); and the creep strain rates are, themselves, functions of the stresses. Furthermore, the internal pressure, p, depends on the volume available for fission gas, V_G, which depends in turn on the coating deflections and hence on the stresses. Thus a double trial-and-error calculation is required to determine the stress distribution in the outer coating at a given time during a coated particle's irradiation history.

The calculations have been implemented through a computer program, STRETCH,[97] with logic flow shown in Fig. 8.47. The computational sequence is as follows: (1) choose a time (or fluence) interval small enough that the use of average stress values over the interval does not introduce serious error; (2) next, assume average values for pressure and creep-strain increments over the interval and use these to calculate a first approximation to the stress distributions, as indicated in the upper left-hand and center blocks in Fig. 8.47; (3) use these stresses to correct the creep-strain increments through the lower left-hand loop

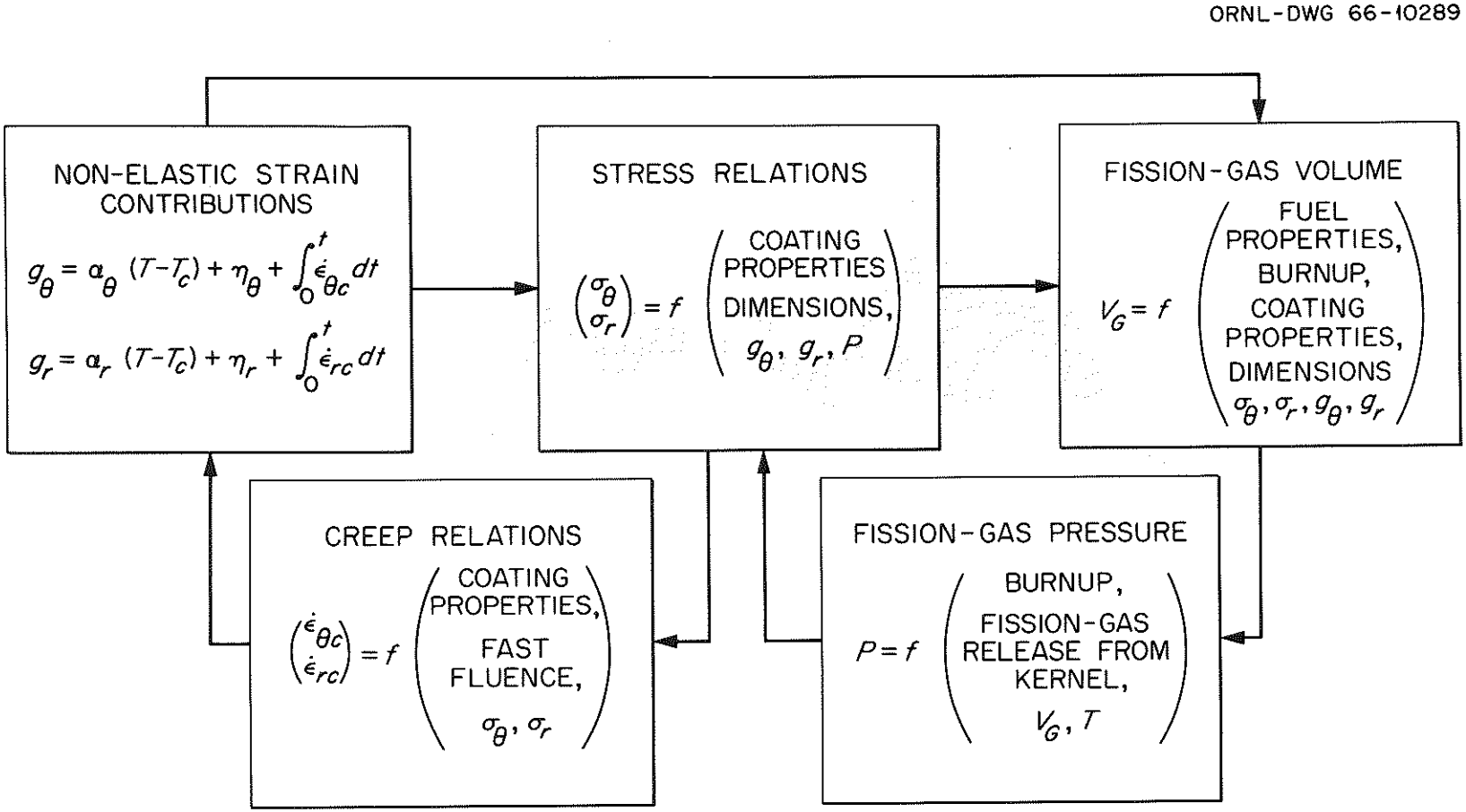

Fig. 8.47. Information flow in coated particle simulation. Reprinted from reference 4.

shown in Fig. 8.47 and repeat the procedure until a converged set of stresses, strains, and creep-strain increments is obtained for the pressure assumed; (4) correct the pressure estimate through the lower right-hand calculation loop (for each new trial pressure, the trial-and-error calculations of the left-hand loop must be performed to obtain stresses and creep-strain increments satisfying the equations for the given pressure); and (5) when convergence is obtained in both loops, a new time interval is selected and the entire procedure repeated. These calculations are continued over successive time intervals until some criterion for termination is met. This is normally the attainment of a given total fluence or time or the exceeding of a specified tangential or effective creep stress at some point in the coating. Complete descriptions of the computer programs required to implement these calculations are now available.[97]

The most serious uncertainty in these calculations is incomplete knowledge of the mechanical and physical properties of pyrolytic-carbon-coating materials under fast-neutron irradiation. Many valuable contributions in this area have been provided by Price and Bokros,[59,68,103] and their results are summarized in Section 8.5 of this chapter. Data are still lacking, however, on mechanical behavior at the high fast fluences (approx 10^{22} neutrons/cm^2, E > 0.18 Mev) anticipated for HTGR fuels. Preliminary data suggest that increases in preferred orientation and swelling of dense pyrolytic carbon may occur at these fast-fluence levels;[59] these could adversely affect coating performance. Clearly, experiments are needed to define more precisely this high fast-fluence behavior.

At low fast-neutron exposures, good agreement has been obtained between model predictions and observed coated-particle performance over a wide range of burnups. Comparison of predicted and observed results is shown in Fig. 8.48 for a set of irradiation tests on pyrolytic-carbon-coated sol-gel and sintered UO_2 microspheres at burnups up to 25 at. % heavy metal fissioned.[104–106] Performance equalled or exceeded predictions in all cases except for a few lots with poorly selected buffer layers in which the buffer layer disintegrated, allowing direct fission-recoil damage to the outer coating and hence premature failure. Fast fluence in these experiments was less than 1×10^{20} neutrons/cm^2 ($E > 0.18$ Mev).

8-7.4 Coated-Particle Performance Limits

As noted earlier, the model calculations provide estimates of the stress-time history for a given coated particle irradiated in a given reactor environment. Specification of a failure-stress condition allows prediction of life to failure for the particle. However, since the coating stress level is influenced almost independently by the fuel burnup, which controls fission-gas production and fuel swelling, and by fast fluence, which controls irradiation distortion and creep, it is convenient to plot, for given coating dimensions and properties, a curve relating the combinations of fuel burnup and fast fluence above which a specified stress-strain state in the coating will be exceeded. Such a curve is known as a failure locus, and defines a boundary in the fast fluence-burnup plane; combinations of burnup and fast fluence lying below and to the left of the locus would not be expected to produce

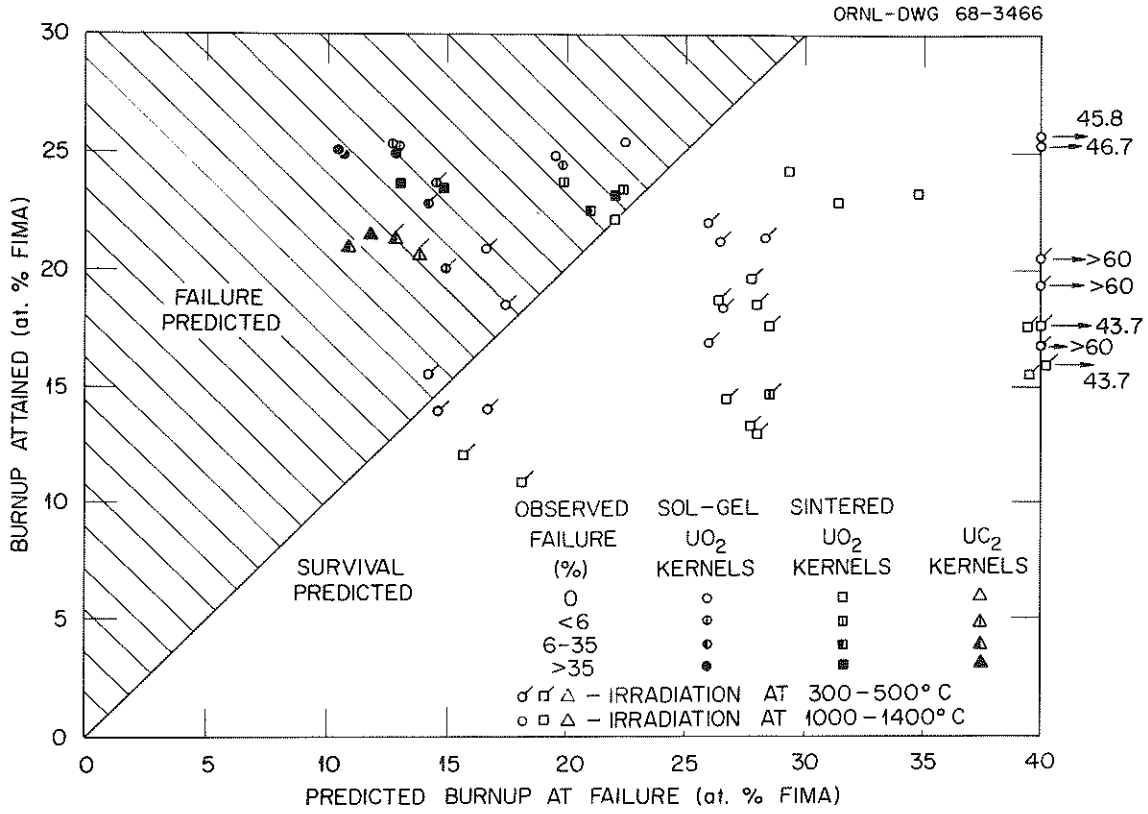

Fig. 8.48. Predicted burnup based on 60,000 psi effective stress at failure, 100% release of fission gas from kernels at high temperatures, 10% release at low temperatures, 25% of inner coating porosity available as free volume (except 50% for porous inner coating), irradiation creep rate of 1×10^{-27} in./in.-psi-neutrons/cm^2 ($E > 0.18$ MeV). Submitted by Oak Ridge National Laboratory, July 1968.

failure, while failure would be expected for combinations above and to the right of the locus. Shown in Fig. 8.49 is a set of typical failure loci (the curves converging toward the abscissa at about 19% burnup) for a two-layer coated particle consisting of a 240-μ-diam, fully dense $(Th,U)C_2$ kernel surrounded by a porous buffer layer, 40 μ thick and a 40-μ, high-density outer layer of moderate anisotropy. The failure loci in this plot are based on a limiting tangential tensile stress of 30,000 psi. The parameters on the failure loci are the steady-state creep coefficients [K in Eq. (24)]. The leftmost failure locus is based on the assumption of no creep; the next one was calculated using a coefficient suggested by the pyrolytic-carbon-creep measurements of Price and Bokros[68] and the other two (incomplete) failure loci were calculated using somewhat higher creep coefficients. Note that these last two curves terminate, indicating that at sufficiently high creep rates, stress relief will be too rapid for the specified failure stress to develop.

The four remaining curves on Fig. 8.49 represent the relation between fast fluence and burnup for a fuel kernel of given thorium-to-uranium ratio, operating in a given neutron energy spectrum. These curves incorporate the assumption that the uranium is 93% enriched in ^{235}U. The point of intersection of one of these fuel-burnup curves with a given failure locus represents the predicted fast fluence and burnup at failure for the given fuel under the given coating creep assumption. The lowest of these fuel-burnup curves represents conditions typical of many coated-particle irradiation tests [i.e., a highly enriched UC_2 (or UO_2) kernel irradiated in a facility where the fast-to-thermal flux ratio is low]. Here the presence or absence of creep has essentially

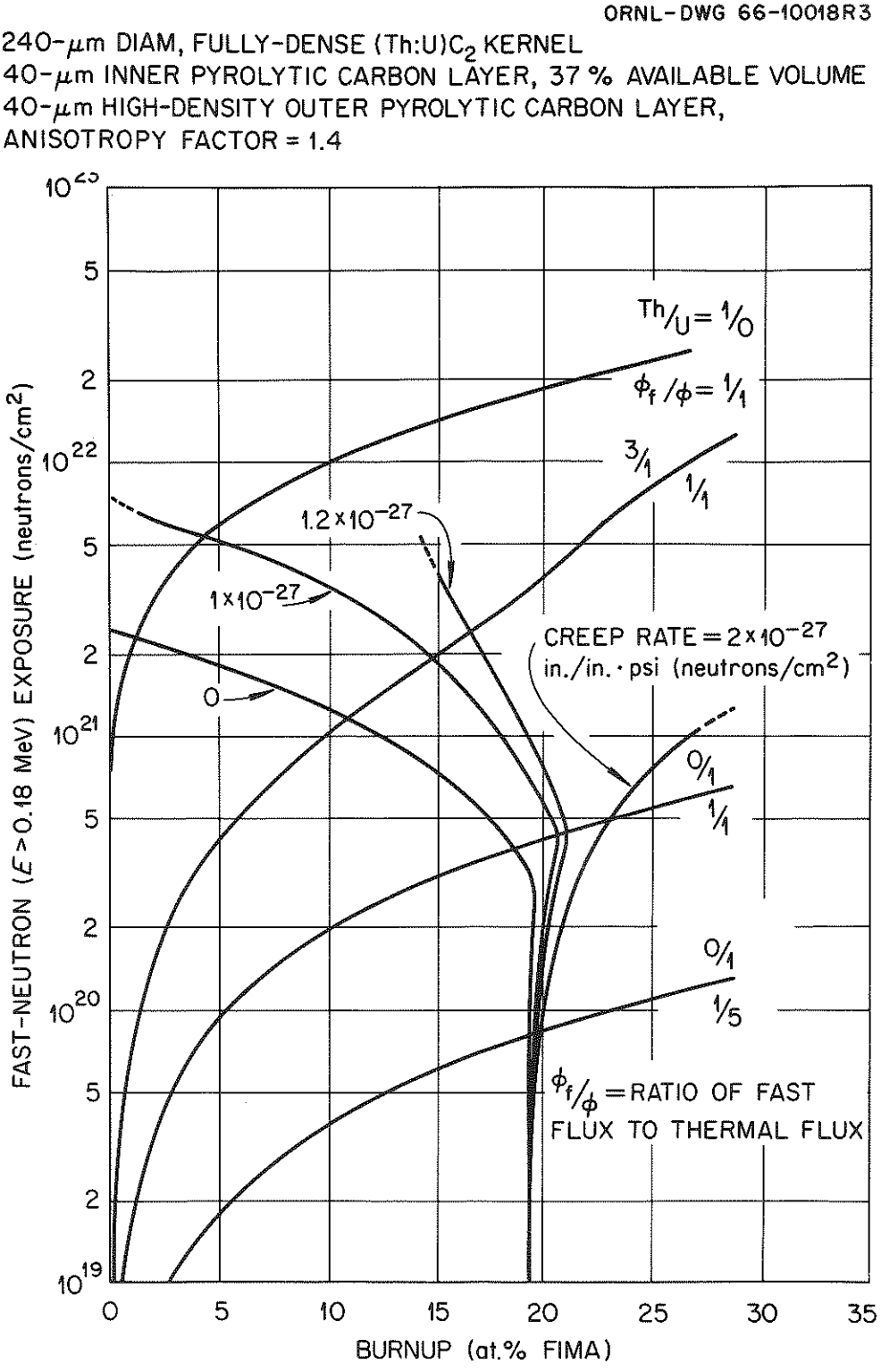

Fig. 8.49. Effect of creep on typical coated-particle failure loci. Reprinted from reference 4.

no effect on failure predictions, since the burnup effects (fuel swelling, fission-gas pressure, etc.) will become severe before sufficient fast fluence has accumulated to allow appreciable creep. It is significant that this curve represents conditions in irradiation tests which gave results in good agreement with model predictions, ignoring creep.[104–106] Figure 8.49 indicates that this would have been expected. The second fuel curve illustrates conditions for the same fuel kernels (enriched UC_2 or UO_2) irradiated in a more energetic neutron-flux spectrum, as might be obtained in a core position in a test reactor. Here the influence of creep on predicted failure conditions is measurable in theory, but experimentally the effect would probably be masked by variations in dimensions and properties of coated particles within a given batch. The two upper curves represent possible conditions for the driver particles and fertile particles, respectively, in the fuel elements of an advanced HTGR converter, designed to utilize a Th-^{233}U cycle. For such particles, coating creep exerts a profound influence on operating lifetime; with sufficiently high creep rates, there is no combination of fast fluence and burnup that would be predicted to cause failure, at least from the standpoint of a limiting stress criterion.

8-7.5 Heat Conduction in Coatings

In evaluating a given coated-particle design, it is necessary to estimate the temperature drops across the coating layers to determine whether excessive fuel-kernel temperature could exist at the expected operating conditions. The equation used to calculate this temperature drop is[107]

$$T_i - T_o = \frac{W}{4\pi k}\left(\frac{r_o - r_i}{r_o r_i}\right), \qquad (38)$$

where

T_i = temperature at inner surface of layer in °C,

T_o = temperature at outer surface of layer in °C,

W = heat generation rate in fuel kernel in watts,

k = thermal conductivity of layer in w cm^{-1} $°C^{-1}$,

r_o = outer radius of layer in cm, and

r_i = inner radius of layer in cm.

The total temperature drop across a coating will be the sum of the drops across individual layers (plus drops across interfacial resistances if contact between coating layers is poor).

Lack of thermal conductivity data on pyrolytic-carbon-coating materials makes such estimates very crude at present. Although thermal conductivity data are available for massive, highly oriented pyrolytic carbon[108] none have been published for fluidized-bed deposited materials employed for nuclear fuel-particle coatings. These are characterized by a relatively low degree of preferred orientation and would not be expected to exhibit the strong anisotropy of thermal conductivity (conductivity in the plane of deposition roughly 100 times that perpendicular to the deposition plane)[108] observed in the massive pyrolytic carbons. The high-density outer coating materials would be expected to possess thermal conductivities intermediate between those in the parallel and perpendicular directions for the massive deposits; however, the conductivities of porous buffer-layer materials should be very low — perhaps even lower than those exhibited by the massive deposits in the perpendicular direction.

For the purposes of estimation, the buffer-layer conductivity has been taken as that of carbon felt insulation in the range 1000 to 1500°C. The values reported by the manufacturer,[109] measured in helium at 1 atm, were halved to account for the lower conductivity of the hydrogen-xenon-krypton mixture expected in the pores of a buffer coating. Resulting conductivity estimates for the buffer layers are in the range 0.001 to 0.002 w cm^{-1} $°C^{-1}$. These values lead to calculated temperature drops across buffer layers in the range 100 to 200°C for typical coated particles and operating conditions, although considerably higher values may exist in accelerated burnup tests, and calculations should be made for each specific set of conditions.

Temperature drops across the outer coatings are expected to be significantly smaller than those across the buffer layer. Even if conservative values for outer coating conductivity are assumed (e.g., 0.05 w cm^{-1} $°C^{-1}$, which is roughly one-tenth the conductivity of reactor-grade graphite and one twentieth the parallel-direction value for massive pyrolytic carbon at 1500°C) temperature drops are computed to be less than 10°C across the outer coating.

8-7.6 Summary of Coating Design Considerations

Results of model calculations and irradiation tests have indicated that the following coated-particle parameters exert a major influence on life under irradiation.

1. Ratio of free volume provided by buffer layer and porous kernel to fuel volume: 2 to 3% free volume per atom percent burnup is required.

2. Thickness of buffer layer: This must be at least sufficient to prevent fission fragments from striking the outer coating. Minimum buffer thickness, t_{min}, in microns may be estimated from the relation,

$$t_{min} = \frac{33}{\rho_B} \mu \ , \tag{39}$$

where

ρ_B is the actual buffer density in grams per cubic centimeter.

More precise relations are given by Evans et al.[110] The thickness should not be so great as to lead to excessive fuel temperatures.

3. Buffer density: Low buffer density increases the free volume available to accommodate fission gas and fuel swelling. However, a minimum buffer density-thickness product must be maintained as given in Eq. (39) to prevent fission-recoil damage to the outer layer.

4. Kernel density: Reducing kernel density below theoretical provides free volume in addition to that of the buffer. Fabrication and cost considerations should determine whether a portion of the required free volume is to be included in the kernel.

5. Thickness of the outer coating layer: Here two opposing factors must be considered. Increased thickness will reduce the stress level at a given internal pressure; however, it will increase the stress from anisotropic fast-neutron-induced distortion. The optimum outer coating thickness for a given particle will depend on the fuel composition and kernel and buffer dimensions for the particle together with the temperature and flux spectrum to which it will be exposed. Detailed calculations are required for any given case.

6. Density and anisotropy of outer coating: The optimum outer coating density is uncertain, and additional high-fast-fluence irradiation data will be required before it can be accurately defined. Values in the range 1.7 to 2.0 g/cm^3 are currently employed. Anisotropy (preferred orientation) should be as low as possible to minimize stress-inducing distortion under fast-neutron irradiation.

7. Outer coating mechanical properties: Desired mechanical behavior for the outer coating includes low values for the Young's moduli, E_θ and E_r, and high values for the creep coefficient, K, and for the stress at which failure would be expected.

8. Ratio of buffer thickness to total coating thickness: In many cases total coating thickness is restricted by fuel-loading requirements. In such cases, increasing the buffer thickness at the expense of the outer coating thickness reduces the fission-gas pressure at a given burnup and temperature, but leads to an increased outer coating stress at a given gas pressure. A complication is provided by the effect of outer coating thickness on stresses arising from fast-neutron damage, as discussed in (5) above. Detailed calculations are required for each case. An example of the results of such calculations for typical $(Th,U)C_2$ particles[106] is shown in Fig. 8.50 for a total coating thickness restricted to 1/3 of the fuel diameter.

In designing a coated particle for a specific irradiation environment, one uses the above considerations in arriving at a preliminary set of specifications. These specifications are then employed in simulation calculations to arrive at a predicted coating life. Repeating the calculations with altered parameters will permit ultimate selection of optimum particle specifications consistent with fabrication and cost considerations.

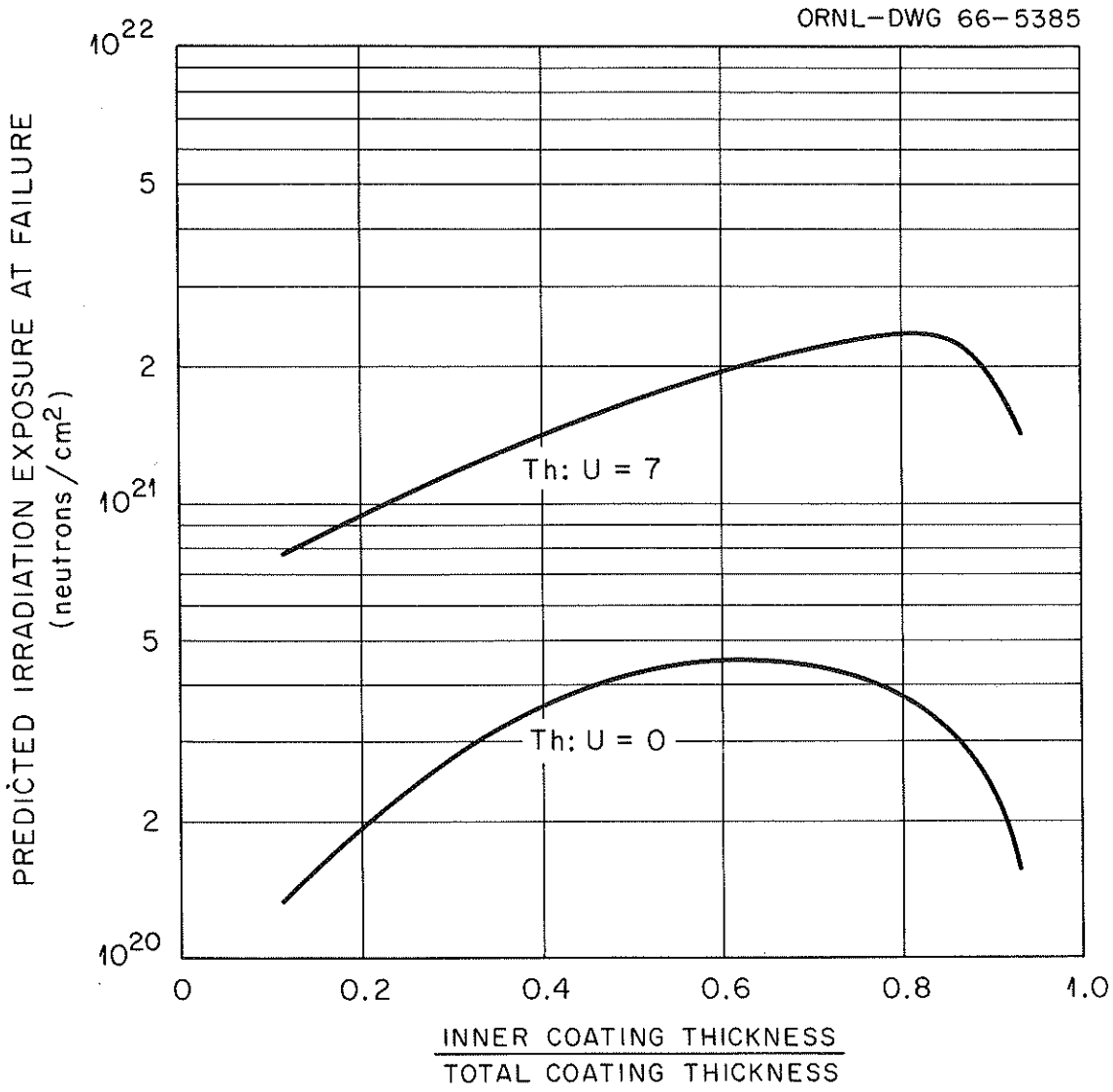

Fig. 8.50. Determination of optimum ratio of inner coating thickness to total coating thickness for coated particles with total coating thickness equal to 1/3 fuel kernel diameter. Reprinted from reference 106.

8-8 REPROCESSING OF COATED-PARTICLE FUELS

Periodic reprocessing of irradiated nuclear power reactor fuels generally is essential to the achievement of an economical fuel cycle, that is, to a low power cost. In the reprocessing step of the fuel cycle, unfissioned uranium and unconverted thorium are separated from fission products and other contaminants and then are converted into a form suitable for refabrication of new fuel elements and subsequent recycle to the reactor. Development of reprocessing methods for graphite-base, coated-particle reactor fuels has proceeded concurrently with the evolution of the various types of fuel. Most of the process development dealt with fuels that contained carbon-coated uranium and thorium carbide particles because this type of fuel will be used in the first graphite-base reactors (Peach Bottom, AVR, and UHTREX). A lesser effort was devoted to processing of other types of fuel, those containing carbon-coated uranium and/or thorium oxide particles and those containing fuel particles coated with ceramics such as SiC, BeO, and Al_2O_3.

According to the current literature the burn-leach process[111–113] (or a modification of it) appears to be the most practicable processing method for coated-particle fuels. This process is especially suited to graphite-matrix fuels that contain carbon-coated carbide particles that are inseparable from the matrix. Another method, the grind-leach process,[111,114–116] has also received considerable evaluation; although the method is applicable in principle to all types of coated-particle fuels, it has several disadvantages, as discussed later. Both the burn-leach and grind-leach processes use nitric acid to dissolve the uranium and thorium compounds, and both terminate in decontamination and recovery

of these elements by solvent extraction. The uranium and thorium are extracted from a nitric acid solution into a tributyl phosphate–kerosene solution, leaving the fission products in the aqueous phase. The uranium and thorium are then stripped from the organic phase with dilute nitric acid; the resulting nitrate solution can be used as a feed solution for the sol-gel recycle process.

8-8.1 The Burn-Leach Process

This process,[111–113] depicted in Fig. 8.51, consists of burning the fuel in air or oxygen to oxidize the carbon to CO_2 and CO and to convert the uranium and thorium to their respective oxides. Combustion in a fluidized bed of inert alumina appears to be the best mode of operation. Graphite-matrix fuels would be crushed to about −6 mesh before being charged to the burner; however, only the coated fuel particles need be burned if they can be mechanically separated from the matrix. Studies have been made with prototype Peach Bottom fuel, both unirradiated and irradiated to burnups of up to 40,000 Mwd/t(U+Th), with 1- to 4-in.-diam fluidized-bed burners. Since the fluidized alumina is a good heat-transfer medium, the reaction temperature was easily controlled. At 700 to 750°C, combustion rates of 1.1 to 1.4 kg of carbon per hour were attained with an oxygen utilization of at least 90%. Irradiated fuel samples oxidized at about the same rate as unirradiated specimens. Early in the development of the burn-leach process it was feared that a highly radioactive combustion off-gas would be produced by volatilization and entrainment of fission products; but experiments with irradiated fuel[113] showed that the combustion

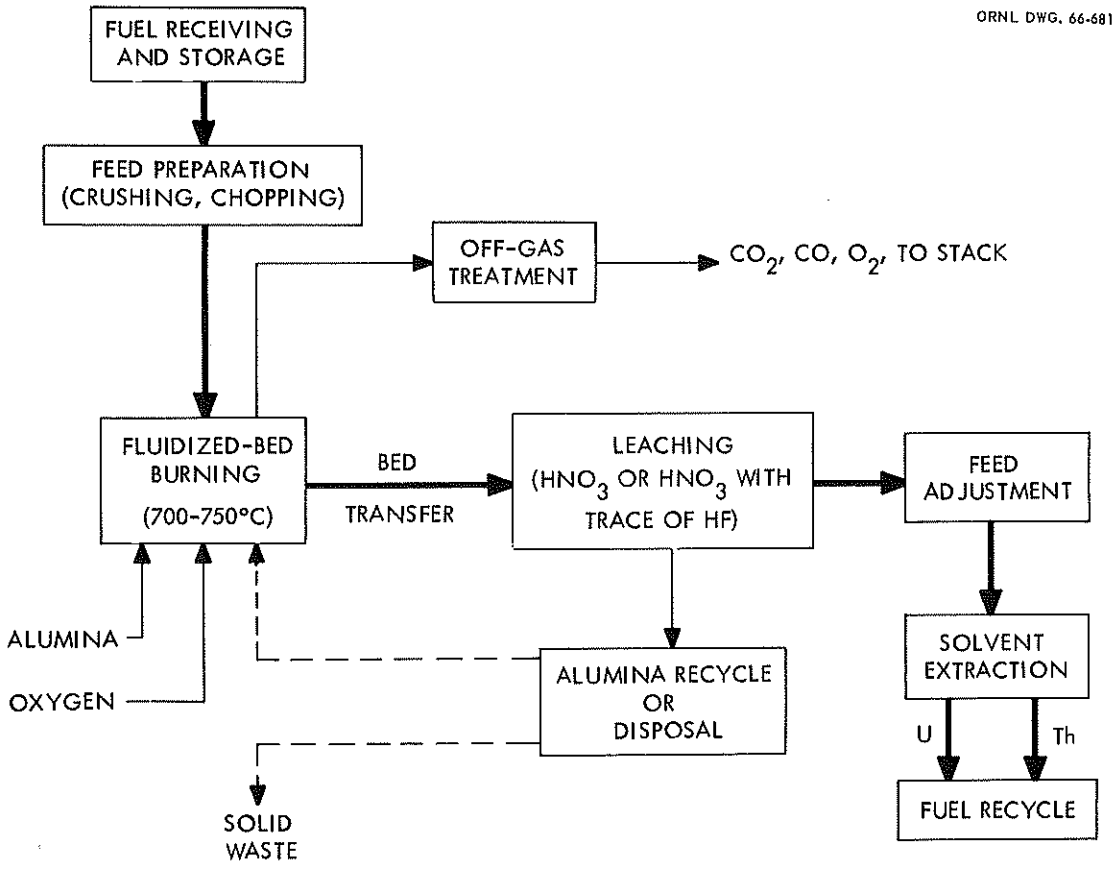

Fig. 8.51. Burn-leach process for graphite-base reactor fuels. Reprinted from reference 111.

off-gas could be readily decontaminated by passage through cooled filters. Actually, a high degree of decontamination (decontamination factors of 10^4 to 10^6) was obtained with only sintered metal filters above the fluidized bed. After passage through the sintered metal filters, usually at temperatures of 150 to 200°C, the off-gas passed through an absolute filter at room temperature where all remaining radioactive species except ^{85}Kr were removed. In an actual plant, the activity of the filtered off-gas could easily be reduced to an acceptable level (below the maximum permissible concentration for ^{85}Kr) by dilution in a stack before release to the atmosphere.

The material in the fluidized-bed burner after combustion (U_3O_8 and/or ThO_2, and fission products dispersed in alumina) is a free-flowing powder and can be readily transferred pneumatically to another vessel for leaching. If ThO_2 is not present, uranium can be recovered by leaching with nitric acid. Products containing ThO_2 must be leached with boiling nitric acid that contains hydrofluoric acid in low concentration if almost complete removal of the uranium and thorium is to be achieved. In the experiments with irradiated fuel,[113] at least 99.8% of the uranium and thorium were recovered by leaching with boiling 13 M HNO_3, 0.05 M HF, 0.05 M $Al(NO_3)_3$; less than 5% of the fission products remained with the alumina. During leaching, less than 1% of the alumina was dissolved; thus, the alumina could probably be recycled to the burner.

The burn-leach process, as described above, is probably not suitable for fuels containing particles coated with SiC, Al_2O_3, or BeO because these ceramics are not chemically attacked during the combustion

step. It has been suggested[111] that fuels of this type could be processed by a grind-burn-leach method. This technique involves grinding the fuel fine enough to rupture the coated particles, burning the powder produced, and then leaching the combustion ash. In small-scale experiments with fuel containing SiC-coated $(Th,U)C_2$ particles, the method led to recovery of at least 99.8% of the uranium and thorium; the SiC was chemically unaffected by the burning and leaching steps.

8-8.2 The Grind-Leach Process

This technique[111,114–116] consists of fine grinding the fuel and then leaching the powder with nitric acid (or nitric acid containing hydrofluoric acid) to recover uranium and thorium. The method, in principle, is applicable to the processing of all types of coated particle fuels if the fuel is ground fine enough to rupture the coated particles. Engineering-scale studies with unirradiated graphite-matrix fuels indicated that the best grinding sequence was to rough-crush the fuel to −6 mesh in a hammer mill and then pulverize the product in a double-roll mill. High crushing rates (10 to 50 kg/hr) were achieved by this method with only minor abrasion of the hammers and rolls. Most of the work was done with fuel containing pyrocarbon- or SiC-coated carbide particles; however, no major problems are anticipated in the crushing of fuels that contain coated oxide particles or particles coated with Al_2O_3 or BeO.

After being crushed, the powder would be leached to recover the uranium and thorium. Nitric acid is a suitable leachant for fuels having UO_2, UC, UC_2, $(Th,U)C_2$, or ThC_2 particles. Nitric acid containing

hydrofluoric acid in low concentration is required for the dissolution of ThO_2 and $(Th,U)O_2$ particles. Much of the experimental work on leaching was done with prototype Peach Bottom fuel. With unirradiated fuel samples, ground to −140 mesh to rupture the $(Th,U)C_2$ particles, up to 99.9% of the uranium and thorium could be recovered by leaching the powder twice for 5 hr with boiling 5 to 16 M HNO_3 (ref. 113). Irradiated sol-gel ThO_2 and $(Th,U)O_2$ particles coated with pyrolytic carbon were treated by the grind-leach process, and recoveries of at least 99.6% of the uranium and 99.9% of the thorium were realized, and more than 86% of the gamma emitters were dissolved.[116] These results contrast markedly with the uranium and thorium recoveries — as low as 95.4 and 93.1%, respectively — that were obtained in grind-leach studies with irradiated laminar-coated $(Th,U)C_2$ particles in a graphite matrix.[115] The low recoveries from the dicarbide fuels were attributed to the migration of the fuel into the pyrolytic-carbon coating where it was relatively inaccessible to the nitric acid.

Although the grind-leach process can be applied successfully to the treatment of HTGR fuels containing carbon-coated sol-gel oxide particles, the economics of the process may not be attractive due to the large retention of fission products by the leached carbon residue. These residues would have to be treated as intermediate- to high-level solid wastes, and their storage would add significantly to the processing costs.

REFERENCES

1. C. R. Tipton, Jr. (Ed.), Reactor Handbook, Vol. 1 – Materials, 2nd ed., pp 299–301, Interscience, New York, 1960.

2. J. M. Blocher, Jr., M. F. Browning, W. J. Wilson, V. M. Secrest, R. B. Landrigan, and J. H. Oxley, Properties of Ceramic-Coated Nuclear-Fuel Particles, Nucl. Sci. Eng. 20(2): 153–170 (1964).

3. W. V. Goeddel, Development and Utilization of Pyrolytic-Carbon-Coated Carbide Fuel for the High-Temperature Gas-Cooled Reactor, Nucl. Sci. Eng. 20: 201–218 (1964).

4. J. W. Prados and J. L. Scott, The Influence of Pyrolytic-Carbon Creep on Coated-Particle Fuel Performance, Nucl. Appl. 3: 488–494 (1967).

5. J. H. Oxley, Recent Developments with Coated-Particle Fuel Materials, Reactor Mater. 6(2): 1–14 (1963).

6. R.A.U. Huddle, M.S.T. Price, M. Howdaille, and W. G. Popp, The Cost of Coated Particle Fuel for High Temperature Reactor Programme, pp 1–26 in Proceedings of the Conference "Fuel Cycles of High-Temperature Gas-Cooled Reactors," D. Tytgat (Ed.), EURATOM Eur. 2780.e (May 1966).

7. J. V. Shennan, Dispersed Ceramic Fuels for the Advanced Gas-Cooled Reactor, Chem. Eng. Progr. Symposium Ser. No. 80 63: 96–110 (1967).

8. J. V. Shennan and M. J. Nichols, The Fabrication of Small Uranium Carbide Spheres, pp 518–539 in Carbides in Nuclear Energy, Vol. 2, Preparation and Fabrication; Irradiation Behaviour (Ed. by L. E. Russell et al.), Macmillan and Company, London, 1964.

9. F. Gorlé and J. J. Huet, The Powder Metallurgy Agglomeration Process for Fabrication of Carbide Spherical Particles, pp 763–776 in Carbides in Nuclear Energy, Vol. 2, Preparation and Fabrication; Irradiation Behavior (Ed. by L. E. Russell et al.), Macmillan and Company, London, 1964.

10. H. Bildstein and P. Koss, Karbidische Brennstoff Hoher Spalt Produktrückhaltefahigkeit für Hoch Temperaturreaktoren, Atompraxis 9: 259–264 (1963).

11. J. J. Huet and F. Gorlé, The Powder-Agglomeration Method for the Fabrication of Spherical Fuel Particles, Kerntechnik 7: 365–367 (1965).

12. H. G. Sowman, R. L. Surver, and J. R. Johnson, The Development of Spherical Pyrolytic-Carbon-Coated UC_2 and $(U,Th)C_2$ Fuel Particles, Nucl. Sci. Eng. 20: 228–234 (1964).

13. H. E. Shoemaker, Method of Preparing Spherical Nuclear Fuel Particles (to U.S. Atomic Energy Commission), U.S. Patent 3,179,722. April 2, 1962.

14. W. V. Goeddel, Method of Forming Metal Carbide Spheroids with Carbon Coat (to U.S. Atomic Energy Commission), U.S. Patent 3,179,723. June 12, 1962.

15. H. G. Sowman and J. R. Johnson, Crystalline Spherules (to Minnesota Mining and Manufacturing Company), U.S. Patent 3,129,188. April 4, 1964.

16. W. V. Goeddel and H. E. Shoemaker, Preparation of $(Th,U)C_2$ Fuel Particles for the HTGR, USAEC Report GA-2881, General Atomic, Nov. 12, 1962.

17. W. V. Goeddel, Pyrolytic-Carbon-Coated Carbide Fuel Particles and Their Use in Graphite-Matrix Fuel Compacts, pp 142–222 in Proceedings of Symposium on "Ceramic Matrix Fuels Containing Coated Particles," Battelle Memorial Institute, November 5–6, 1962, USAEC Report TID-7654, June 1963.

18. R.A.U. Huddle, J. R. Gough, and H. Beutler, Coated-Particle Fuel for the Dragon Reactor Experiment, pp 349–374 in Proceedings of Symposium on "Ceramic Matrix Fuels Containing Coated Particles," Battelle Memorial Institute, November 5–6, 1962, USAEC Report TID-7654, June 1963.

19. M. N. Burkett, W. P. Eatherly, and W. O. Harms, Fueled-Graphite Elements for the German Pebble-Bed Reactor (AVR), paper presented at the AIME Symposium on High Temperature Nuclear Fuels, Delavan, Wis., October 3–5, 1966 (to be published).

20. J. O. Gibson, The Synthesis of (UZr)-C at 5000° Kelvin, pp 816–825 in Carbides in Nuclear Energy, Vol. 2, Preparation and Fabrication; Irradiation Behaviour (ed. by L. E. Russel et al.), Macmillan and Company, London, 1964.

21. D. E. Ferguson, O. C. Dean, and P. A. Haas, Preparation of Oxide Fuels for Vibratory Compaction by the Sol-Gel Process, pp 23–38 in Symposium on Powder Packed Uranium Dioxide Fuel Elements, Vol. 1, USAEC Report CEND-153, Combustion Engineering Nuclear Division, November 1962.

22. A. L. Lotts, J. D. Sease, R. E. Brooksbank, A. R. Irvine, and F. W. Davis, The Oak Ridge National Laboratory Kilorod Facility, pp. 351–383 in Proceedings of the Thorium Fuel Cycle Symposium, Gatlinburg, Tennessee, December 5–7, 1962, USAEC Report TID-7650 July 1963.

23. P. A. Haas and S. D. Clinton, Preparation of Thoria and Mixed-Oxide Microspheres, Ind. Eng. Chem. Prod. Res. Develop. 5(3): 236–244 (1966).

24. J. P. McBride (Comp.), Preparation of UO_2 Microspheres by a Sol-Gel Technique, USAEC Report ORNL-3874, Oak Ridge National Laboratory, February 1966.

25. J. L. Kelly, A. T. Kleinsteuber, S. D. Clinton, and O. C. Dean, Sol-Gel Process for Preparing Spheroidal Particles of the Dicarbides of Thorium and Thorium-Uranium Mixtures, Ind. Eng. Chem. Prod. Res. Develop. 4(2): 212–216 (1965).

26. P. A. Haas, W. D. Bond, M. H. Lloyd, and J. P. McBride, Sol-Gel Process Development and Microsphere Preparation, pp 391–415 in Proceedings of the 2nd International Thorium Fuel Cycle Symposium, Gatlinburg, Tennessee, May 1966, R. G. Wymer (Coordinator) CONF-660524 (Feb. 1968).

27. P. A. Haas, S. D. Clinton, and A. T. Kleinsteuber, Preparation of Urania and Urania-Zirconia Microspheres by a Sol-Gel Process, Can. J. Chem. Eng. 44(6): 348–353 (1966).

28. D. M. Helton, Dispersion of a Liquid Stream by an Electrical Potential: Applications to the Preparation of Thoria Microspheres, USAEC Report ORNL-TM-1395, Oak Ridge National Laboratory, January 1966.

29. P. A. Haas, F. G. Kitts, and H. Beutler, Preparation of Reactor Fuels by Sol-Gel Process, Chem. Eng. Progr. Symposium Ser. No. 80 63: 16–27 (1967).

30. R. G. Wymer and J. H. Coobs, Preparation, Coating, Evaluation, and Irradiation Testing of Sol-Gel Oxide Microspheres, Proc. Brit. Ceram. Soc. 7, 61–79 (1967).

31. G. W. Horsley, L. A. Podo, and F. C. Wood, Studies on the Reprocessing and Refabrication of HTGR Fuels in the OECD Dragon Project, pp 121–144 in Proceedings of the Conference "Fuel Cycles of High-Temperature Gas-Cooled Reactors," D. Tytgat (ed.), EURATOM Eur 2780.e (May 1966).

32. R. W. Dayton. J. H. Oxley, and C. W. Townley (eds.), Proceedings of Symposium on "Ceramic Matrix Fuels Containing Coated Particles," Battelle Memorial Institute, November 5–6, 1962, USAEC Report TID-7654, June 1963.

33. M. F. Browning, J. M. Blocher, Jr., V. M. Secrest, and A. C. Secrest, Coating Fuel Particles with Pyrolytic Carbon, USAEC Report BMI-1643 Battelle Memorial Institute, 1963.

34. M. F. Browning and J. M. Blocher, Jr., Preparation of Experimental Coated Particles by Chemical Vapor Deposition, pp 42–106 in Development of Ceramic-Coated-Particle Nuclear Fuels Summary Report, C. W. Townley (ed.), USAEC Report BMI-1768, Battelle Memorial Institute, April 1966.

35. F. L. Carlsen, Jr., E. S. Bomar, and W. O. Harms, Development of Fueled Graphite Containing Pyrolytic-Carbon-Coated Carbide Particles for Nonpurged, Gas-Cooled Reactor Systems, Nucl. Sci. Eng. 20: 180–200 (1964).

36. R.A.U. Huddle, The Development of Coated-Particle Fuel for High-Temperature Reactors, Atompraxis 12: 54–57 (1966).

37. R. A. Reuter, Duplex Carbon-Coated Fuel Particles, Nucl. Sci. Eng. 20: 219–226 (1964).

38. M.S.T. Price, J.R.G. Gough and J. W. Horsley, Fuel Element Fabrication for the Dragon Reactor Experiment, J. Brit. Nucl. Energy Soc. 5: 361–382 (1966).

39. R. L. Beatty, F. L. Carlsen, and J. L. Cook, Pyrolytic-Carbon Coatings on Ceramic Fuel Particles, Nucl. Appl. 1: 560–566 (1965).

40. J. C. Bokros, The Structure of Pyrolytic Carbon Deposited in a Fluidized Bed, Carbon 3: 17–29 (1965).

41. H. Beutler, R. L. Beatty, and J. H. Coobs, Low Density Pyrolytic-Carbon Coatings for Nuclear Fuel Particles, Electrochem. Technol. 5: 189–194 (1967).

42. J.R.C. Gough and D. Kern, Studies on the Coating of Fuel Particles for the Dragon Reactor Experiment, J. Nucl. Energy 21: 623–642 (1967).

43. A. L. Lotts, Fueled-Graphite Development, pp 210–215 in Metals and Ceramics Division Annual Progress Report June 30, 1966, USAEC Report ORNL-3970, Oak Ridge National Laboratory, October 1966.

44. J. C. Bokros, Variation in the Crystallinity of Carbons Deposited in a Fluidized Bed, Carbon 3: 201–211 (1965).

45. R. L. Pilloton, Gas Flow Calculations for Fluidized-Bed Coating of Nuclear Fuel Particles, USAEC Report ORNL-3639, Oak Ridge National Laboratory, June 1964.

46. P. Popper and F. L. Riley, Texture of Pyrolytic Silicon Carbide, Proc. Brit. Ceram. Soc. 7, 99–109 (1967).

47. R. B. Landrigan, M. F. Browning, and J. M. Blocher, Jr., Carbide Coatings, p 101 in Development of Ceramic-Coated-Particle Nuclear Fuels Summary Report, C. W. Townley (ed.), USAEC Report BMI-1768 Battelle Memorial Institute, April 25, 1966.

48. H. Beutler, Deposition and Characterization of Silicon Carbide Coatings, pp 10–16 in Gas-Cooled Reactor Program Semiannual Progress Report March 31, 1967, USAEC Report ORNL-4133, Oak Ridge National Laboratory, August 1967.

49. L. H. Ford, N. S. Hibbert, B. E. Ingleby, and D.E.Y. Walker, The Fluidised Bed Coating of Uranium Monocarbide with Silicon Carbide, British Report TRG-1544 (Springfields), 1967.

50. T. D. Gulden, Deposition and Microstructure of Vapor-Deposited Silicon Carbide, USAEC Report GA-8275, General Atomic, Dec. 1, 1967.

51. R. L. Beatty, Oak Ridge National Laboratory, unpublished, February 1968.

52. W. V. Goeddel, Coated-Particle Fuels in High Temperature Reactors: A Summary of Current Application, Nucl. Appl. 3(10): 599–614 (1967).

53. W. O. Harms, Carbon-Coated Carbide Particles as Nuclear Fuels, pp 290–313 in Modern Ceramics – Some Principles and Concepts, J. E. Hove and W. C. Riley (Eds.), Wiley, New York, 1965.

54. G. E. Bacon, The Method for Determining the Degree of Orientation of Graphite, J. Appl. Chem. (London) 6: 477–481 (1956).

55. D. M. Hewette II, and R. L. Beatty, Coatings Deposited from Methane in a 2-in.-diam Fluidized Bed, pp 3–6 in Gas-Cooled Reactor Program Semiannual Progress Report March 31, 1966, USAEC Report ORNL-3951 Oak Ridge National Laboratory, July 1966.

56. R. L. Beatty, Pyrolytic Carbon Deposited from Propane in a Fluidized Bed, USAEC Report ORNL-TM-1649, Oak Ridge National Laboratory, January 1967.

57. J. L. Scott and R. L. Beatty, Pyrolytic-Carbon Coatings Formed at High Deposition Rates, Trans. Am. Nucl. Soc. 10: 96 (1967).

58. J. C. Bokros and R. J. Price, Deformation and Fracture of Pyrolytic Carbons Deposited in a Fluidized Bed, Carbon 3: 503–519 (1966).

59. R. J. Price, J. C. Bokros, and K. Koyama, Thermal Expansivities and Preferred Orientation of Pyrolytic Carbons, Carbon 5: 423–430 (1967).

60. R. J. Price and J. C. Bokros, Relationship Between Preferred Orientation, Thermal Expansion and Irradiation-Induced Length Changes in Graphite, J. Appl. Phys. 36: 1897–1906 (1965).

61. J. P. Blakely, N. V. Smith, and L. G. Overholser, Compatibility of Unsupported Pyrolytic-Carbon Coated Uranium Dicarbide Particles with Water Vapor, USAEC Report ORNL-3598, Oak Ridge National Laboratory, 1964.

62. R. D. Burnette, J. M. Dixon, D. R. Lofing, and L. R. Zumwalt, Experiments on the Reaction of High-Temperature Steam with Pyrolytic-Carbon-Coated $(Th,U)C_2$ Particles, USAEC Report GA-7005, General Atomic Division, General Dynamics Corporation, 1966.

63. C. M. Blood and L. G. Overholser, Compatibility of Pyrolytic-Carbon Coated Fuel Particles with Water Vapor, USAEC Report ORNL-4014, Oak Ridge National Laboratory, 1966.

64. J. E. Baker and L. G. Overholser, Compatibility of Pyrolytic-Carbon Coated Fuel Particles with Water Vapor, pp 124–133 in Gas-Cooled Reactor Semiannual Progress Report September 30, 1967, USAEC Report ORNL-4200, Oak Ridge National Laboratory, February 1968.

65. D. M. Hewette and J. H. Coobs, Preparation and Characterization of Specimens for the ORNL-DFR-2, -3, and -4 Irradiation Experiments, pp 77–79 in Gas-Cooled Reactor Semiannual Progress Report March 31, 1967, USAEC Report ORNL-4133, Oak Ridge National Laboratory,

66. J. C. Bokros and R. J. Price, Radiation-Induced Dimensional Changes in Pyrolytic Carbons Deposited in a Fluidized Bed, Carbon 4: 441–454 (1966).

67. J. L. Rutherford, J. P. Blakely, and L. G. Overholser, Oxidation of Unfueled and Fueled Graphite Spheres by Steam, USAEC Report ORNL-3947, Oak Ridge National Laboratory, 1966.

68. R. J. Price and J. C. Bokros, Mechanical Properties of Neutron-Irradiated Pyrolytic Carbons, J. Nucl. Mater. 21: 158–174 (1967).

69. H. H. Yoshikawa, Radiation Effects on Pyrolytic Graphite, Nucl. Sci. Eng. 19: 461–462 (1964).

70. J. C. Bokros and A. S. Schwartz, A Model to Describe Neutron-Induced Dimensional Changes in Pyrolytic Carbon, Carbon 5: 481–492 (1967).

71. J. L. Scott, D. F. Toner, and R. E. Adams, Release of Fission Products from Coated Fuel Particles, pp 86–88 in Gas-Cooled Reactor Semiannual Progress Report June 30, 1961, USAEC Report ORNL-3166, Oak Ridge National Laboratory, 1961.

72. L. R. Zumwalt, E. E. Anderson, and P. E. Gethard, Fission-Product Release from $(Th,U)C_2$-Graphite Fuels, pp 223–272 in Proceedings of Symposium on "Ceramic Matrix Fuels Containing Coated Particles," Battelle Memorial Institute, November 5–6, 1962, USAEC Report TID-7654, June 1963.

73. C. W. Townley, N. E. Miller, R. L. Ritzman, and R. J. Burian, In-Pile Performance of Ceramic Coated-Particle Fuels, Nucleonics 22: 43–48 (1964).

74. P. E. Reagan, F. R. Carlsen, and R. M. Carroll, Fission-Gas Release from Pyrolytic-Carbon-Coated Fuel Particles During Irradiation, Nucl. Sci. Eng. 18: 301–318 (1964).

75. R. W. Dayton, J. H. Oxley, and C. W. Townley, Ceramic Coated Particle Nuclear Fuels, J. Nucl. Mater. 11: 1–31 (1964).

76. P. E. Reagan, J. G. Morgan, and O. Sisman, Fission-Gas Release from Pyrolytic-Carbon-Coated Fuel Particles During Irradiation at 2000 to 2500°F, Nucl. Sci. Eng. 23: 215–223 (1965).

77. P. E. Reagan, R. L. Beatty, and E. L. Long, Jr., Performance of Pyrolytic-Carbon-Coated Uranium Oxide Particles During Irradiation at High Temperature, Nucl. Sci. Eng. 28: 34–41 (April 1967).

78. E. S. Bomar and R. J. Gray, Thorium-Uranium Carbides for Coated-Particle Graphite Fuels, pp 703–728 in International Symposium on Compounds of Interest in Nuclear Reactor Technology, J. T. Waber, P. Chiotti, and W. N. Miner, (Eds.), AIME Metallurgical Society, New York, 1964.

79. R. W. Dayton and R. F. Dickerson, Progress Relating to Civilian Applications During September 1963, USAEC Report BMI-1650, Battelle Memorial Institute, 1963.

80. M. T. Morgan and R. L. Towns, Fission-Product Release from High Burnup Coated Fuel Particles by Postirradiation Heating, pp 107–113 in Gas-Cooled Reactor Program Semiannual Progress Report September 30, 1967, USAEC Report ORNL-4200, Oak Ridge National Laboratory, February 1968.

81. Public Service Company of Colorado 330-Mw(E) HTGR, Quarterly Progress Report December 31, 1967, USAEC Report GA-8420, pp 131–134, Gulf General Atomic, January 29, 1968.

82. J. L. Scott and D. F. Toner, Release of Fission Products from Fueled Graphite, pp 180–184 in Gas-Cooled Reactor Program Quarterly Progress Report March 31, 1962, USAEC Report ORNL-3302, Oak Ridge National Laboratory, July 1962.

83. R. H. Flowers, J. Pattison, F.C.W. Pummery, and R. Watts, Some Measurements of the Diffusion of ^{235}U Fission Products and ^{233}Pa from Coated Fuels, British Report AERE-R-4215, 1962.

84. P. E. Gethard and L. R. Zumwalt, Diffusion of Metallic Fission Products in Pyrolytic Carbon, Nucl. Appl. 3: 679–685 (1967).

85. H. S. Rosenburg, D. L. Morrison, C. W. Townley, and D. N. Sunderman, Postirradiation Fission-Product Release from Coated Fuel Particles, USAEC Report BMI-1734, Battelle Memorial Institute, 1965.

86. H. J. de Nordwall and J. B. Sayers, The Value of A Silicon Carbide Barrier in HTR Fuels, paper presented at the AIME Symposium on High Temperature Nuclear Fuels, Delavan, Wis., October 3–5, 1966 (to be published).

87. M. T. Morgan and R. L. Towns, Fission-Product Release from High-Burnup Coated Fuel Particles by Postirradiation Annealing, pp 89–91 in Gas-Cooled Reactor Program Semiannual Progress Report March 31, 1967, USAEC Report ORNL-4133, Oak Ridge National Laboratory, August 1967.

88. HTGR-Base Program Quarterly Progress Report Nov. 30, 1967, USAEC Report GA-8356, pp 91–106, Gulf General Atomic, December 29, 1967.

89. Public Service Company of Colorado 330-Mw(E) High-Temperature Gas-Cooled Reactor Research and Development Program Quarterly Progress Report June 30, 1967, USAEC Report GA-8038, pp 146–154, Gulf General Atomic, July 1967.

90. Summary Report on the Use of TRISCO-Coated Particles in the PSC Reactor Plant, pp 28–44, USAEC Report GA-8467, Gulf General Atomic, January 1968.

91. Gas-Cooled Reactor Program Semiannual Progress Report March 31, 1967, pp 60–67, USAEC Report ORNL-4133, Oak Ridge National Laboratory, August 1967.

92. Gas-Cooled Reactor Program Semiannual Progress Report September 30, 1967, pp 37–46; 94–97, USAEC Report ORNL-4200, Oak Ridge National Laboratory, February 1968.

93. P. E. Reagan, Fission-Gas Release and Irradiation Damage to AVR Pyrolytic-Carbon Coated Thorium-Uranium Carbide Particles, USAEC Report ORNL-4053, Oak Ridge National Laboratory, January 1967.

94. J. W. Prados and J. L. Scott, Mathematical Model for Predicting Coated-Particle Behavior, Nucl. Appl. 2: 402–414 (1966).

95. J. W. Prados, Computer Program for Predicting Coated-Particle Behavior, USAEC Report, ORNL-TM-1385, Oak Ridge National Laboratory, March 1966.

96. A. S. Schwartz, The Design of Buffer-Isotropic-Coated Fuel Particles to Survive High Burnup Operation, Chem. Eng. Progr. Symposium Ser. No. 80 63: 121–129 (1967).

97. J. W. Prados and T. G. Godfrey, STRETCH, A Computer Program for Predicting Coated-Particle Irradiation Behavior; Modification IV, December 1967, USAEC Report ORNL-TM-2127, Oak Ridge National Laboratory, April 1968.

98. D. M. Himmerblau, Basic Principles and Calculations in Chemical Engineering, 2nd ed., Prentice Hall, Englewood Cliffs, N.J., 1967.

99. A. Mendelson, M. H. Hirschberg, and S. S. Manson, A General Approach to the Solution of Practical Creep Problems, J. Basic Engr. 81: 585–598 (1959).

100. R. Hill, The Mathematical Theory of Plasticity, Oxford University Press, London, 1950.

101. K. K. Shah and G. Thodos, A Comparison of Equations of State, Ind. Eng. Chem. 57: 30–37 (1965).

102. J. A. Brinkman, Fundamentals of Fission Damage, pp 1–11 in Nuclear Metallurgy, Vol. 4, Met. Soc. Am. Inst. Mining Met. Petrol. Engrs. Inst. Metals Div. Spec. Rep. 9 (1959).

103. J. C. Bokros and R. J. Price, Dimensional Changes Induced in Pyrolytic Carbons by High-Temperature Fast-Neutron Irradiation, Carbon 5: 301–312 (1967).

104. J. H. Coobs, R. L. Beatty, A. R. Olsen, H. L. Krautwedel, J. W. Prados, and J. L. Scott, Testing of a Design Analysis for Coated-Particle Fuels, Trans. Am. Nucl. Soc. 9: 421–422 (1966).

105. A. R. Olsen, J. H. Coobs, D. M. Hewette II, H. L. Krautwedel, A. W. Longest, J. W. Prados, and J. L. Scott, Performance of Pyrolytic-Carbon-Coated Sol-Gel UO_2 Microspheres in High-Burnup Irradiation Tests, Trans. Am. Nucl. Soc. 10: 96–97 (1967).

106. J. W. Prados, R. L. Beatty, H. Beutler, J. H. Coobs, A. R. Olsen, and J. L. Scott, Development of Coated-Particle Fuels for Advanced Gas-Cooled Reactors, pp 273–292 in Proceedings of the 2nd International Thorium Fuel Cycle Symposium, Gatlinburg, Tennessee, May 1966, R. G. Wymer (coordinator), CONF-660524 (1968).

107. H. Etherington (ed.), Nuclear Engineering Handbook, 1st. ed., Vol. 1, p 57, McGraw-Hill, New York, 1957.

108. General Electric Company Pyrolytic Graphite Engineering Handbook, p. 10, Metallurgical Products Department, General Electric Company, Detroit, Michigan, 1963.

109. Bulletin No. 110, New Product Data Sheet, Carbon Products Division, Union Carbide Corporation, 270 Park Avenue, New York.

110. R. B. Evans III, J. L. Rutherford, and R. B. Perez, Recoil of Fission Products in Homogeneous Carbon Structures, J. Appl. Phys. 38: 3127–3134 (1967).

111. L. M. Ferris, Head-End Processes for Graphite-Base and Carbide Reactor Fuels, to appear in Progress in Nuclear Energy, Process Chemistry, Vol. 4, Pergamon Press.

112. E. L. Nicholson, L. M. Ferris, and J. T. Roberts, Burn-Leach Processes for Graphite-Base Reactor Fuels Containing Carbon-Coated Carbide or Oxide Particles, USAEC Report ORNL-TM-1096, Oak Ridge National Laboratory, April 2, 1965.

113. J. R. Flanary, J. H. Goode, H. O. Witte, and V.C.A. Vaughen, Hot-Cell Evaluation of the Burn-Leach Process Using Irradiated Graphite-Base HTGR Fuels, USAEC Report ORNL-4120, Oak Ridge National Laboratory (in press).

114. L. M. Ferris, Grind-Leach Process for Graphite-Base Reactor Fuels That Contain Coated Particles: Laboratory Development, USAEC Report ORNL-4110, Oak Ridge National Laboratory, June 1967.

115. J. R. Flanary and J. H. Goode, Hot-Cell Evaluation of the Grind-Leach Process. I. Irradiated HTGR Candidate Fuels: Pyrocarbon-Coated $(Th,U)C_2$ Particles Dispersed in Graphite, USAEC Report ORNL-4117, Oak Ridge National Laboratory, August 1967.

116. J. H. Goode and J. R. Flanary, Hot-Cell Evaluation of the Grind-Leach Process. II. Recovery of Uranium and Thorium from Irradiated Pyrolytic-Carbon-Coated Sol-Gel Thoria-Urania Particles, USAEC Report ORNL-4213, Oak Ridge National Laboratory, March 1968.

ORNL-4324
UC-25 — Metals, Ceramics, and Materials

INTERNAL DISTRIBUTION

1–3. Central Research Library
4–5. ORNL — Y-12 Technical Library Document Reference Section
6–25. Laboratory Records
26. Laboratory Records, ORNL, RC
27. ORNL Patent Office
28. S. E. Beall, Jr.
29. R. J. Beaver
30. R. L. Beatty
31. D. S. Billington
32. C. M. Blood
33. G. E. Boyd
34. C. D. Cagle
35. W. H. Carr
36. A. K. Chakraborty
37. Ji Young Chang
38. J. H. Coobs
39. G. L. Copeland
40. C. M. Cox
41. D. R. Cuneo
42. J. E. Cunningham
43. R. G. Donnelly
44. W. S. Ernst
45. J. I. Federer
46. L. M. Ferris
47. B. C. Finney
48. J. R. Flanary
49. J. H Frye, Jr.
50. T. G. Godfrey
51. A. Goldman
52. J. H. Goode
53. R. J. Gray
54. R. W. Gunkel
55. W. O. Harms
56–58. M. R. Hill
59. P. R. Kasten
60. T. M. Kegley, Jr.
61. G. W. Keilholtz
62. E. E. Ketchen
63. C. E. Lamb
64. C. E. Larson
65. T. B. Lindemer
66. C. S. Lisser
67. B. T. Loh
68. E. L. Long, Jr.
69. R. A. Lorentz
70. A. L. Lotts
71. H. G. MacPherson
72. A. P. Malinauskas
73. G. B. Marrow
74. D. L. McElroy
75. C. J. McHargue
76. T. L. McLean
77. F. R. McQuilkin
78. J. R. McWherter
79. J. G. Merkle
80. F. W. Miles
81. R. P. Milford
82. W. R. Mixon
83. S. E. Moore
84. W. L. Moore
85. F. H. Neill
86. K. J. Notz
87. M. F. Osborne
88. L. G. Overholser
89. P. Patriarca
90. A. M. Perry
91. J. W. Prados
92. R. B. Pratt
93. J. T. Roberts
94. A. C. Schaffhauser
95. J. L. Scott
96. C. E. Sessions
97. M. D. Silverman
98. W. G. Stockdale
99. R. S. Stone
100. D. A. Sundberg
101. V. J. Tennery
102–148. D. B. Trauger
149. W. E. Unger
150. R. S. Valachovic
151. G. M. Watson
152. A. M. Weinberg
153. Paul Wood
154. R. G. Wymer
155. G. T. Yahr
156. C. M. Adams (consultant)
157. Leo Brewer (consultant)
158. L. S. Darken (consultant)
159. J. A. Krumshansl (consultant)

EXTERNAL DISTRIBUTION

160. R. H. Ball, RDT, SSR, Gulf General Atomic
161. R. J. Bard, Los Alamos Scientific Laboratory
162. W. Bell, Gulf General Atomic
163. A. M. Boltax, Westinghouse Astronuclear Laboratory
164. D. F. Cope, RDT, SSR, AEC, Oak Ridge National Laboratory
165. R. W. Dayton, Battelle Memorial Institute
166. J. E. Fox, AEC, Washington
167. A. Gaimbusso, AEC, Washington
168. W. V. Goeddel, Gulf General Atomic
169. A. J. Goodjohn, Gulf General Atomic
170. H. Hessing, SNPO, Los Alamos
171. J. D. Holmgren, Westinghouse Astronuclear Laboratory
172. R. F. Kirkpatrick, AEC, Washington
173. A. W. Larson, AEC, San Francisco
174. L. L. Lyon, Los Alamos Scientific Laboratory
175. C. L. Matthews, RDT, OSR, AEC, Oak Ridge National Laboratory
176. D. Moss, AEC, Washington
177. R. E. Pahler, AEC, Washington
178. W. S. Scheib, Jr., SNPO, Washington
179. J. M. Simmons, AEC, Washington
180. D. K. Stevens, AEC, Washington
181. J. A. Swartout, Union Carbide Corporation, New York
182. S. A. Szawlewicz, AEC, Washington
183. J. F. Watson, Gulf General Atomic
184. Laboratory and University Division, AEC, Oak Ridge Operations
185-381. Given distribution as shown in TID-4500 under Metals, Ceramics, and Materials category